



HAL
open science

Multi-scale coupling of CFD/porous solvers through domain decomposition method applied to multidirectional flows

Chufa Qiu

► **To cite this version:**

Chufa Qiu. Multi-scale coupling of CFD/porous solvers through domain decomposition method applied to multidirectional flows. Fluid mechanics [physics.class-ph]. Université Paris-Saclay, 2022. English. NNT: 2022UPAST189 . tel-03957576

HAL Id: tel-03957576

<https://theses.hal.science/tel-03957576v1>

Submitted on 26 Jan 2023

HAL is a multi-disciplinary open access archive for the deposit and dissemination of scientific research documents, whether they are published or not. The documents may come from teaching and research institutions in France or abroad, or from public or private research centers.

L'archive ouverte pluridisciplinaire **HAL**, est destinée au dépôt et à la diffusion de documents scientifiques de niveau recherche, publiés ou non, émanant des établissements d'enseignement et de recherche français ou étrangers, des laboratoires publics ou privés.

Multi-scale coupling of CFD/porous solvers
through domain decomposition method applied
to multidirectional flows
*Couplage multi-échelle des solveurs CFD/poreux par la
méthode de décomposition de domaine appliquée aux
écoulements multidirectionnels*

Thèse de doctorat de l'université Paris-Saclay

École doctorale n° 579, Sciences Mécaniques et Energétiques,
Matériaux et Géosciences (SMEMaG) Spécialité de doctorat :
Mécanique des fluides

Graduate School: Sciences de l'ingénierie et des systèmes
Réfèrent : ENS Paris-Saclay

Thèse préparée dans l'unité de recherche Service de Thermo-hydraulique et de Mécanique des Fluides (Université Paris-Saclay, CEA), sous la direction de **Vincent FAUCHER**, Directeur de recherche, le co-encadrement de **Bruno RAVERDY**, Ingénieur-chercheur.

Thèse soutenue à Saclay, le 15 décembre 2022, par

Chufa QIU

Composition du Jury

Membres du jury avec voix délibérative

Michel BELLIARD Directeur de recherche, CEA Cadarache	Président
Stéphane VINCENT Professeur, Université Gustave Eiffel	Rapporteur
Philippe HELLUY Professeur, Université de Strasbourg	Rapporteur & Examineur
Olivier HURISSE Ingénieur-chercheur, HDR, EDF R&D	Rapporteur & Examineur
Anne CHARMEAU Ingénieure-chercheuse, IRSN	Examinatrice

Titre : Couplage multi-échelle des solveurs CFD/poreux par la méthode de décomposition de domaine appliquée aux écoulements multidirectionnels

Mots clés : thermo-hydraulique, multi-échelle, couplage de codes, décomposition de domaine

Résumé : Ce travail de thèse est consacré au développement d'une méthode de couplage entre un code CFD et un code dit " poreux" qui est dédié à la modélisation thermohydraulique à l'échelle moyenne dans un coeur de réacteur nucléaire. La méthode de décomposition de domaine partitionné a été retenue comme méthode de couplage. Deux approches sont utilisées, une avec recouvrement et l'autre sans qui se basent respectivement sur une méthode de Schwarz Multiplicative et une méthode itérative de Dirichlet-Neumann. Une stratégie de résolution itérative de type point fixe est adjointe aux précédentes approches avec deux algorithmes explicite et implicite. Pour améliorer les échanges de données entre deux maillages non-conformes, des procédures de prolongation et de restriction ont été développées.

La vérification de la méthode de couplage

a été réalisée sur un ensemble de cas test à complexité croissante afin de vérifier l'influence des approches avec et sans recouvrement, l'impact des algorithmes explicite et implicite et l'interopérabilité de la méthode. De plus, les nouvelles procédures de prolongation et de restriction ont montré leur bénéfice dans le couplage. Enfin, la méthode de couplage a été appliquée à un cas représentatif d'un écoulement dans un coeur de réacteur nucléaire, à savoir l'écoulement dans l'expérience MANIVEL. Ainsi, des premiers calculs CFD ont été réalisés sur cette expérience afin de disposer de données de références. Ensuite, des simulations couplées ont été réalisées et comparées avec ces références. Pour finir, des calculs prospectifs d'un déséquilibre de débit en entrée d'assemblage ont été réalisés.

Title : Multi-scale coupling of CFD/porous solvers through domain decomposition method applied to multidirectional flows

Keywords : thermal-hydraulic, multi-scale, codes coupling, domain decomposition

Abstract : This thesis work is devoted to the development of a coupling method between a CFD code and a so-called "porous" code which is dedicated to the thermal-hydraulic modelling at the sub-channel scale of a nuclear reactor core. The partitioned domain decomposition method has been chosen for the coupling work. Two methods are applied, one with overlap and the other without, based on Multiplicative Schwarz and iterative Dirichlet-Neumann methods, respectively. An iterative fixed-point solving strategy is implemented with explicit and implicit algorithms using previous approaches as pre-conditioners. For the purpose of improving the data exchange between two non-conforming meshes, prolongation and restriction procedures have been developed.

The verification of the coupling method has

been performed on a set of test cases with increasing complexity to verify the influence of overlapping and non-overlapping approaches, the impact of explicit and implicit algorithms and the interoperability of the method. Moreover, the new prolongation and restriction procedures have shown their benefit in the coupling. Finally, the coupling method has been applied to a representative case simulating the flow in a nuclear reactor core, namely the MANIVEL experiment. Thus, first CFD calculations have been realized on this experiment to obtain reference data. Then, coupled simulation were carried out and compared with these references. Finally, prospective computations of a flow imbalance at the inlet of the assembly has been performed.

Acknowledgement

This thesis work was performed in the LATF laboratory of the Commissariat à l’Energie Atomique et aux Energies Alternatives (CEA Saclay). I want to express my sincere gratitude to all the people who have ever helped me during my Ph.D project.

Firstly, I would like to thank Bruno RAVERDY for his friendly reception when I came to the laboratory, for his teachings and inspiration, for giving me an excellent example of a researcher with a great passion and for his support and encouragement during this challenging period of COVID19. Thanks to him, I learned to be more autonomous when doing research.

The sincere and hearty appreciations go to my thesis director, Vincent FAUCHER, for his point of view on research, for his advice in the editing and revising of articles and this thesis, for his great patience. We had many meaningful discussions which gave me good inspiration and are helpful in my future work.

I gratefully acknowledge Clotire GEFFRAY and Chai KOREN for their advice and support in the coupling work related to NEPTUNE_CFD; I would like to thank Evangelos STAVROPOULOS VASILAKIS for providing technical advice about linear interpolation; I want to express my gratitude to TRUST support team for dealing with many technical issues about Trio_CFD.

Then, I would like to thank Bertrand MERCIER and Eric PROUST for their recommendation of this thesis. They have given me advice and generous guidance in my study and life since I became a student of IFCEN.

Finally, I must express my very profound gratitude to my family and university classmates for providing me with unfailing support and continuous encouragement throughout the process of research. The author gratefully acknowledges other colleagues of the STMF service for their kindness and availability during my work at CEA.

邱初发

Contents

Résumé substantiel en français	V
Acronyms	VII
Nomenclature	VIII
List of publications	IX
1 Introduction	1
2 Domain partitioned approaches	5
2.1 Domain overlapping method	5
2.2 Domain decomposition method	6
2.2.1 Schwarz methods	7
2.2.2 Optimized Schwarz method	13
2.2.3 Schur complement method	15
2.2.4 Accelerants: Krylov methods	18
2.3 Different mesh refinements: LDC methods	23
2.3.1 Model case of decomposition into two domains	24
2.3.2 Multi-grid method for domain decomposition	25
2.3.3 Multigrid data exchange methods	27
2.4 Numerical algorithms used in coupling work	36
2.4.1 Data exchange and time coupling	36
2.4.2 Problem formulation	37
2.4.3 Explicit coupling scheme	38
2.4.4 Implicit coupling scheme	40
2.4.5 General implicit coupling scheme	41
2.5 Conclusions	42
3 Complex problem of coupling different two-phase flow models	43
3.1 Phasic variables	43
3.2 Mixture variables	44

3.3	Porous 4 equations model : FLICA4	45
3.4	Six equations model : NEPTUNE_CFD	48
3.4.1	Mass balance equations	48
3.4.2	Momentum equations	49
3.4.3	Energy equations	50
3.5	Coupling of two-phase flow models	51
3.5.1	Left STFM model	51
3.5.2	Right HRM model	52
3.5.3	Father model	52
3.5.4	Main ideas of the coupling algorithm	52
3.6	Conclusions	53
4	Verification and validation through test cases	55
4.1	Coupling of CFD/CFD	55
4.1.1	One-dimensional flow	56
4.1.2	Two-dimensional flow	63
4.1.3	Reverse flow	67
4.2	Coupling of SC/CFD	71
4.2.1	FT mode	72
4.2.2	TF mode	74
4.3	Conclusions	76
5	Semi-industrial implementation and experimental validation	79
5.1	MANIVEL experiment	79
5.1.1	Context of benchmark experiment	79
5.1.2	Description of the facility	80
5.1.3	Analysis of experiment	85
5.2	Simulation with SC code: average modeling	87
5.2.1	Description of mesh and parametric parameters	89
5.2.2	Results	90
5.3	CFD Simulation : influence of inlet turbulent flow	90
5.3.1	Introduction	91
5.3.2	Mesh generation	93
5.3.3	RANS turbulence models	94
5.3.4	Boundary conditions	95
5.3.5	RANS model sensitivity study	97
5.3.6	Mesh sensitivity study with the $R_{ij} - \varepsilon$ SSG model	103
5.3.7	Conclusions	107
5.4	SC/CFD coupling	107
5.4.1	Axial velocity results	108

5.4.2	Pressure drop results	111
5.5	Prospective CFD/SC coupling with modified inlet flow	113
5.6	Conclusions	114
6	Conclusions and perspectives	117
6.1	Conclusions	117
6.1.1	Coupling methods development	117
6.1.2	Verification with test cases	118
6.1.3	Influence of inlet turbulent flow	119
6.1.4	Experimental validation	119
6.2	Perspectives	119
	List of Figures	121
	List of Tables	124
	Bibliography	125

Résumé substantiel en français

La sûreté de la centrale nucléaire est basée sur trois barrières et notre sujet s'intéresse à la première (la gaine du crayon combustible). L'idée principale de la conception du réacteur peut être résumée à plusieurs objectives : on cherche une température et une pression de la sortie plus grandes possible pour améliorer l'efficacité du transfert de chaleur ; en outre, on cherche une homogénéité de l'état thermo-hydraulique du fluide caloporteur pour la sûreté nucléaire.

Mais en réalité, la distribution des écoulements n'est pas uniforme, comme la redistribution des débits entre différents assemblages et différents sous-canaux causée par l'écoulement transverse. Cela a plusieurs conséquences : la risque de vibration, la crise d'ébullition et la destruction de la structure. A l'industrie nucléaire, des études de la sûreté nucléaire sont menées afin d'assurer que le critère pour l'intégrité physique soit respecté pour toutes les situations rencontrées.

Des codes composants, comme FLICA4, VIPRE ou COBRA sont utilisés pour simuler un ou plusieurs assemblages. A cause de la conception interne complexe des assemblages de combustible, la taille de l'écoulement varie de sub-millimètre jusqu'à mètre. Alors, le solveur poreux n'est pas approprié dans certaines situations (des écoulements 3D), et le code CFD est un outil essentiel pour obtenir l'information dans la région la plus intéressante. Mais la simulation du cœur complet de REP avec un seul domaine de CFD est inaccessible. D'où la méthodologie de la thèse est de coupler un solveur poreux avec un code CFD bien résolu pour améliorer l'efficacité de calcul.

D'abord, on peut faire des hypothèses suivantes : seulement l'écoulement monophasique et incompressible est considéré ; on va coupler avec les conditions aux limites disponibles pour chaque code sans la modification ; le système des équations n'est pas libre à choisir. D'après la littérature, la méthode de domaine décomposition est choisie pour notre couplage parce que c'est plus simple à être implémentée. Dans ce cas-là, le système à modéliser est simulé par différents solveurs locaux avec leur propres domaines locaux. Les champs de variables sont échangés aux frontières entre deux codes.

Il y a deux types de partitionnements qu'on peut distinguer : sans recouvrement, l'intersection entre sub-domaines est limitée à l'interface ; avec recouvrement, chaque sub-domaine recouvre une partie de ses voisins. Enfin, l'algorithme Dirichlet-Neumann est choisi pour notre couplage sans recouvrement basé sur les conditions aux limites disponibles (Dirichlet pour l'entrée et Neumann pour la sortie), et la méthode de Schwarz multiplicative est utilisée pour le cas avec recouvrement parce qu'elle converge plus vite.

Sur la résolution d'un problème linéaire, l'itération du point-fixe est utilisée pour développer des schémas numériques explicite et implicite dont le type implicite est plus favorable en termes de

stabilité numérique. En considérant les densités du maillage différents, la moyenne surfacique ou volumique est appliquée dans la procédure de restriction ; par contre, la méthode d'interpolation linéaire développée nous permet d'imposer un profil de vitesse plus précise dans la procédure de prolongation.

La vérification de la méthode de couplage a été réalisée sur un ensemble de cas test à complexité croissante. Il y a trois cas test dans la partie de couplage entre CFD/CFD. D'abord, pour un écoulement monodirectionnel dont la direction est perpendiculaire à l'interface, le recouvrement du domaine n'est pas nécessaire et la méthode d'interpolation nous permet de conserver le profil de vitesse. Ensuite, pour un écoulement bidirectionnel, le couplage avec recouvrement est plus approprié parce qu'il y a une perturbation près de la sortie dans le domaine en amont. Enfin, en considérant l'écoulement avec l'effet de rétroaction, c'est mieux de lancer un couplage de Dirichlet-Dirichlet avec recouvrement.

Puis, dans la partie de couplage entre SC/CFD. On a considéré deux modes différents avec le code SC en amont ou en aval du domaine. Dans le régime stationnaire, la distribution de la pression a un profil continu dans le domaine de calcul même si on utilise les pas de temps différents entre deux solveurs. Dans le régime transitoire, on a les résultats similaires avec les pas de temps identiques, mais on va obtenir les résultats incohérents avec les pas de temps différents si le code SC est en amont du domaine parce qu'il est considéré comme un filtre, la variation de la vitesse va être filtrée.

Finalement, la méthode de couplage a été appliquée à un cas représentatif avec une expérience de benchmark MANIVEL. Les premiers calculs de CFD ont été réalisés pour analyser l'influence du flux turbulent à l'entrée. On peut générer le flux turbulent bien développé en utilisant les faisceaux de tube avec une longueur réduite sans la grille. Le modèle Rij avec un maillage fin nous permet de capturer le creux au centre de chaque sous-canal. Les couplages avec ou sans recouvrement nous donnent la même chose parce que l'écoulement est presque monodirectionnel. Les résultats de couplage sont proches des données expérimentales, et l'écart est à cause du flux turbulent d'entrée qui n'est pas bien développé.

Pour les travaux au futur, il faut optimiser le couplage SC/CFD de l'expérience de benchmark, ça veut dire d'améliorer la méthode d'interpolation entre les maillages 3D structuré et non-structuré. C'est intéressant de construire un type de condition aux limites pour le couplage afin d'être plus cohérent avec la méthode de domaine décomposition. On peut réfléchir sur la possibilité de lancer un couplage pour l'écoulement diphasique, dans ce cas-là, les variables à transférer seront différentes et on doit vérifier l'équation de l'état.

Acronyms

BC	Boundary Conditions
CFD	Computational Fluid Dynamics
LOCA	Loss Of Coolant Accident
PWR	Pressurized Water Reactor
RANS	Reynolds-Averaged Navier-Stokes
STH	System Thermal Hydraulics
SC	Sub-Channel
PDE	Partial Differential Equation
FETI	Finite Element Tearing and Interconnect
LDC	Local Defect Correction
AS	Additive Schwarz
RAS	Restricted Additive Schwarz
SSG	Simple Support Grid
CHF	Critical Heat Flux
LDV	Laser Doppler Velocimetry
LES	Large Eddy Simulation
ONB	Onset of the Nucleate Boiling
CIPS	Crud-Induced Power Shift
ICoCo	Interface for Code Coupling
RHS	Right Hand Side
LHS	Left Hand Side

Nomenclature

α	Volume fraction
δ	Relative error
μ	Dynamic viscosity
ρ	Density
σ	Standard deviation
τ	Friction forces
τ_{ij}	Viscous stress tensor
ε	Kinetic energy
$D_{h,SC}$	Hydraulic diameter of typical sub-channel
D_h	Hydraulic diameter of a test section bare rod bundle
f_{MCA}	Darcy friction factor from McAdams correlation
g	Gravity
H	One-span length
K_{BR}	One-span friction-related pressure loss coefficient
K_{cv}	Concentration dispersion coefficient
K_{SSG}	One-span grid-related pressure loss coefficient
P_{dyn}	Dynamic pressure
Re_{D_h}	Reynolds number based on hydraulic diameter
Re_{SC}	Reynolds number based on the typical sub-channel hydraulic diameter
V_0	Bulk velocity

List of publications

Papers published in peer-reviewed Journals

- C.Qiu, B.Raverdy, and V.Faucher. Development of a partitioned coupling method based on multi-scale data exchanges between porous and CFD solvers for a nuclear core. *Annals of Nuclear Energy*, 2022.

Papers published in International Conference Proceedings

- C.Qiu, B.Raverdy, V.Faucher and A.Bergeron. Influence of inlet turbulent flow generated by periodic computations on the pressure drop and axial velocity distribution predictions. In *International Conference on Nuclear Engineering (ICONE28)*. American Society of Mechanical Engineers, 2021.
- C.Qiu, B.Raverdy, and V.Faucher. Development of a sub-channel/CFD coupling method for multi-scaled simulations. In *International Topic Meeting on Nuclear Reactor Thermal Hydraulics (NURETH19)*. American Nuclear Society, 2022.

Chapter 1

Introduction

Recently, economies are developing rapidly all over the world, consequently, energy demands have simultaneously increased rapidly. Counting challenges associated with global climate and environmental impact, nuclear energy has gained more and more attention due to its high power generation and zero carbon gas emissions. Nuclear reactor uses the energy released by fission of nuclear fuels which are principally composed by U235 and Pu239 to produce electrical power [1]. Cold water is used to cool down the nuclear reactor and convert the thermal energy to electricity. In the following, the nuclear reactors of the PWR (Pressurized Water Reactors) family are considered where the nuclear fuel is cooled by liquid water under forced flow.

In order to ensure the safety of nuclear power plant, three barriers of containment presented in the nuclear reactor work at preventing from the dispersion of radioactive products into natural environment as the following [2]:

- the first barrier : the metal cladding which contains the nuclear fuel, consisting of uranium pellets where the fission occurs; it prevents the radioactive constituents produced by fission reaction from dispersing into the fluid;
- the second barrier : the reactor primary circuit composed of the vessel which contains the nuclear core and the different pipes for fluid circulation; it isolates much of the radioactive material of the core from external environment where human being can step in;
- the third barrier : the concrete containment building, which surrounds the reactor coolant system, it can not only isolate radiation from natural environment but also sustain external forces attack.

The basic idea of reactor design can be summarized in several objectives: firstly, the average outlet temperature and pressure should be increased as much as possible to improve the efficiency of heat transfer [3]; secondly, in order to ensure the safety of the reactor core, it is necessary to seek homogeneity of the thermal-hydraulic state of the cooling water.

Indeed, heterogeneity in the core leads to a non-uniform temperature distribution, which in certain situations can give rise to the appearance of bubbles that coalesce to form a steam film with a considerable reduction in heat transfer [4]. This situation can result in an excursion of the cladding temperature beyond the cladding melting one, thus the first containment barrier is destroyed. Heterogeneities can be caused by transverse flows that develop in the core with the origin of the non-uniformity of the assembly supply due to the flow redistribution in the lower plenum below the assemblies or the expansion of the jets coming from the lower holes of the core support plate which contributes to a phenomenon of flow redistribution between the different sub-channels of an assembly. The consequences can be characterized by assembly expulsion due to hydrodynamic thrust, by vibrations [5] that accelerate fuel wear or by boiling crisis that leads to cladding destruction.

In the nuclear industry, thermal-hydraulic safety studies are performed to ensure [6, 7] that the criteria for the physical integrity of the three barriers are met for all situations encountered. Thermal-hydraulic codes are used for these purposes, in particular to simulate flows on a "system" scale, such as RELAP5 [8], TRACE [9] or CATHARE [10], which are part of the system thermal-hydraulic codes (STH). Concerning core flows, codes such as COBRA [11], VIPRE [12] or FLICA4 [13] allow us to simulate at subchannel (SC) scale [14]. To account for unresolved physics, such as singular friction, Reynolds tensor, mass transfer, etc., correlations from experiments are used, which can provide reliable solutions [15].

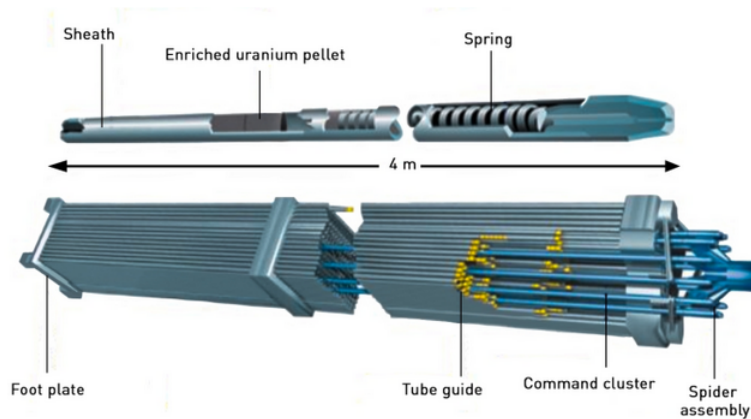


Figure 1-1: Schematic view of a fuel assembly [16]

Due to the intricate internal design (fuel rods, control rods and grids [17]) of the fuel assemblies in the nuclear core (see Figure 1-1), the scales of the flow vary from sub-millimeters (e.g. secondary flow downstream spacer grids [18]) to meters (e.g. transverse flow between assemblies) [19]. Unfortunately, the SC codes are not perfect in situations that present transverse flows between assemblies and sub-channels, in particular for flow redistribution or when the flow is 3D with sub-millimeter spatial scales and high temporal frequencies. For these flow conditions, the Computational Fluid

Dynamics (CFD) is an essential tool to obtain detailed information in the most interesting regions near complex structures, such as spacer grids, as opposed to SC codes which are more suitable to simulate mean flow. Capturing all the physical scales with one single CFD computational domain covering all the PWR core is currently unaffordable, even considering upcoming exascale supercomputers. A more suitable approach classically proposed and explored in the current research in agreement with the specifics of the PWR nuclear core flow conditions is to implement a multi-scale strategy [20].

The proposed methodology is based on coupling a porous SC model with a well-resolved CFD model to improve computational efficiency. Code coupling is already a popular approach in the open literature [21], which could be characterized by two domain partitioned approaches: the domain overlapping method and the domain decomposition method. For the domain overlapping methods [22, 23, 24] applied to our SC/CFD coupling, the SC code simulates the whole domain including the CFD part, and provides boundary conditions to the CFD code, which in turn provides a better description of local phenomena; in this case, CFD solution is used to correct the solution of the SC code in the overlapping domain. For the domain decomposition methods [25], the system to be modelled is simulated by different local solvers with their own local domains and field variables and boundaries where information are exchanged between two codes. Domain overlapping approach has favorable numerical stability characteristics while the domain decomposition approach is chosen in our work since it is easier and less intrusive to be implemented and only localized information needs to be exchanged.

Considering the domain decomposition method, computational domains for the two solvers can be partially overlapping or not [26, 27, 28]. The used methods are Schwarz alternating and Schur complement, respectively. The case with overlapping subdomains can converge with all-Dirichlet transmission conditions. In contrast, for non-intersecting subdomains, Robin-Robin, Neumann-Neumann transmission conditions, etc., are required to obtain convergent solutions. Based on the types of boundary conditions defined on two sides of interface, Gander et al. [29] proposed the Neumann-Dirichlet method to satisfy the equilibrium equation while only Dirichlet or Neumann method is used for respectively velocity or pressure in our work. Concerning the practical data exchange between domains with different levels of modeling and refinement, a multi-grid method is applied, which consists of restriction and prolongation steps. When passing data from a fine domain to a coarse one (restriction step), homogenization of data obtained by CFD code is transferred to the SC code, whereas in reverse (prolongation step), CFD code should retrieve the information obtained by SC code as accurately as possible. Zhang et al. [21] have used the way of 'uniform by pieces' when imposing the velocity profile on the side of CFD solver; here, a new method is developed through linear interpolation to reconstruct a continuous profile from piecewise constant solution obtained by SC code.

Once the multi-scale boundary conditions setting the data exchange between the coupled domains are defined, the time-coupling strategy must be proposed. Explicit or implicit solution schemes [30, 31] can be adopted; in the explicit coupling scheme, the coupled solvers compute once every time step and data transfer only occurs at the end of each time step; while in the implicit one, data exchange is repeated within a time step via sub-iterations until a defined convergence criterion is met.

This thesis is finally dedicated to presenting the domain decomposition coupling between CFD and SC solvers (with or without overlap) at different scales with a newly developed data exchange method and fixed-point numerical scheme. From a software point of view, the coupling is implemented in the formalism of the ICoCo library [32] and is restricted for demonstrative purposes to single-phase hydraulics including the study of transverse flow in PWR fuel assemblies. The thesis is structured as follows. First, domain decomposition and data exchange methods are presented in the following section. A verification procedure is then carried out with increasing complexity from one-dimensional flow to multi-dimensional ones. Finally, the full coupling between CFD and SC solvers is provided to simulate a benchmark experiment with an assembly flow, namely MANIVEL. The results are compared to the experimental data and reference CFD simulations to validate the coupling methods. Some purely numerical prospective results are also proposed in the reference experimental configuration to illustrate the capability of the proposed approach to compute localized cross flows in an assembly with non-homogeneous inlet flow.

Chapter 2

Domain partitioned approaches

This chapter reviews the state of the art of domain partitioned approaches used in multi-scale simulations. Particular attention is given to domain decomposition methods with a description of the methods applied in overlapping and non-overlapping configurations. Then, the coupling convergence acceleration techniques used are described. Finally, in the case of coupling between domains with different refinements, the methods developed are exposed.

2.1 Domain overlapping method

For the domain overlapping methods [22], the STH/SC code simulates the whole domain including the CFD part, and provides boundary conditions to the CFD code, which in turn provides a better description of local phenomena, as depicted in Figure 2-1; in this case, CFD solution is used to correct the solution of the STH/SC code in the overlapping domain [33].

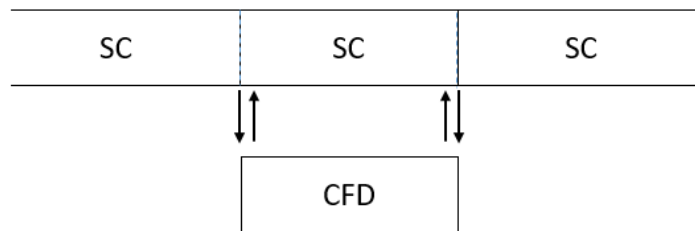


Figure 2-1: Illustration of domain overlapping methods

This approach has been widely employed in the framework of CFD/STH coupling. But, this approach needs to modify the system equations used in the STH solver. We can cite the work of Fanning and Thomas [23] which modified the energy equation and the gravitational pressure term of the system code SAS4A using the CFD solution for the simulation of sodium-cooled reactors or the work of Jeltsov et al. [24] which used a CFD solution to correct the system code energy

equation through the implementation of a "virtual heater". Bavière et al. [34] introduced a source term in the momentum equation of the system code to adjust the overall pressure drop across the overlapped component with the CFD solution. Huxford et al. [35] used the CFD solution to correct the friction factor in the momentum equation of the system code SAM. Grunloh et al. [22] used the pressure gradient computed by the STAR-CCM+ to modify the friction factor of system code TRACE. Besides, Liu et al. [36] has developed a different method whose principle is close to the concept of overset mesh method for the coupling of CFD-based sub-channel code and CFD code, such as the 3D-to-3D data exchange algorithm at the coupling interfaces, and the forms of information feedback. A correction source term is used to force the velocity of coarse-grid model to approach that of the refined sub-models. Pressure is also reconstructed using the solution of embedded resolved model in the overlapping region.

Comparison between domain overlapping and domain decomposition has been performed by Grunloh and Manera [37] to examine the effect of each coupling method on convergence, consistency and numerical stability. As a results, domain overlapping method shows more favourable convergence and stability behaviour, while domain decomposition method is more intuitive and easier to be implemented since only field variables need to be exchanged in contrast to the modification of system equations in the STH/SC code. In the following, a detailed description of related decomposition methods employed in our works is presented.

2.2 Domain decomposition method

The domain decomposition methods [38, 39, 40, 41, 28] have received a lot of attention in the last few years, because of their obvious implication in parallel computation. The principle is quite simple: one transforms a large problem into a sequence of decoupled sub-problems of smaller size, which can be solved in parallel. Two types of partitioning can be distinguished:

- without overlap: the intersection between the subdomains is limited to the interfaces (see left Figure 2-2);
- with overlap: each subdomain overlaps a part of its neighbors (see right Figure 2-2).

We briefly present the main part of domain decomposition methods starting with the first method proposed by Schwarz with overlap.

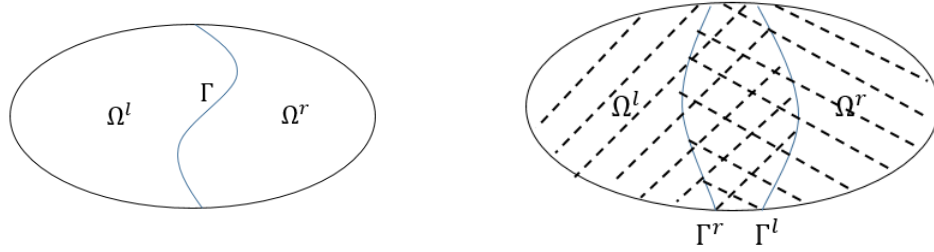


Figure 2-2: Decomposition into two domains : without (left) and with (right) overlap.

2.2.1 Schwarz methods

Schwarz [42] proposes the first domain decomposition method for a global computation on a complex geometry into an iterative one on simple geometries. To illustrate our point, we consider the Poisson equation defined on a domain Ω (see Figure 2-3), where the global problem is split into overlapping sub-problems which are solved alternatively by exchanging interface conditions. This method is called multiplicative or alternating Schwarz algorithm [43].

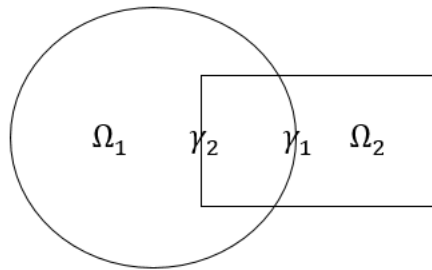


Figure 2-3: A complex domain made from two overlapping subdomains

The Poisson problem is defined on a domain Ω :

Find $u: \Omega \mapsto \mathbb{R}$ such that

$$\begin{cases} -\Delta u = f, & \text{in } \Omega \\ u = 0, & \text{on } \partial\Omega \end{cases} \quad (2.1)$$

For simplification, the boundary condition on $\partial\Omega$ is neglected.

Alternating Schwarz algorithm

The main idea is to use an iterative fixed point algorithm based on solving alternately sub-problems

in domains Ω_1 and Ω_2 with boundary conditions updated from the opposed domain solution at the previous iteration. We take the last interface values calculated by the neighboring subdomain as Dirichlet conditions. The algorithm is carried out in two steps:

$$\begin{cases} -\Delta(u_1^{n+1}) = f, & \text{in } \Omega_1, \\ u_1^{n+1} = u_2^n & \text{on } \gamma_1 \end{cases} \quad (2.2)$$

then

$$\begin{cases} -\Delta(u_2^{n+1}) = f, & \text{in } \Omega_2, \\ u_2^{n+1} = u_1^{n+1} & \text{on } \gamma_2 \end{cases} \quad (2.3)$$

The convergence and well-posedness has been proved by H. Schwarz. One can notice that this algorithm is sequential, which means step (2.3) needs solution of step (2.2) to start the computation.

Multiplicative Schwarz (MS) method

Gander [44] made the demonstration that this method is also equivalent to the discretized Schwarz method. Thus, from numerical point of view, the discretized equation of Eq.(2.1) leads to the linear system [28] :

$$Au = f, \quad A \text{ a large sparse matrix}$$

With the restriction matrices

$$R_1 = \begin{bmatrix} 1 & & \\ & \ddots & \\ & & 1 \end{bmatrix} \quad R_2 = \begin{bmatrix} & & \\ & 1 & \\ & & \ddots \\ & & & 1 \end{bmatrix}$$

and $A_j = R_j A R_j^T$ the MS method reads

$$u^{n+1/2} = u^n + R_1^T A_1^{-1} R_1 (f - Au^n) \quad (2.4)$$

$$u^{n+1} = u^{n+1/2} + R_2^T A_2^{-1} R_2 (f - Au^{n+1/2}) \quad (2.5)$$

The next, we will prove the relation with alternating Schwarz method. If the R_j are non-overlapping, and we partition accordingly

$$A = \begin{bmatrix} A_1 & A_{12} \\ A_{21} & A_2 \end{bmatrix}, \quad f = \begin{pmatrix} f_1 \\ f_2 \end{pmatrix}$$

we obtain from the first relation of MS, i.e.

$$u^{n+1/2} = u^n + R_1^T A_1^{-1} R_1 (f - Au^n)$$

an interesting cancellation:

$$\begin{aligned}
 R_1(f - Au^n) &= f_1 - A_1 u_1^n - A_{12} u_2^n \\
 A_1^{-1} R_1(f - Au^n) &= A_1^{-1}(f_1 - A_{12} u_2^n) - u_1^n \\
 \begin{pmatrix} u_1^{n+1/2} \\ u_2^{n+1/2} \end{pmatrix} &= \begin{pmatrix} u_1^n \\ u_2^n \end{pmatrix} + \begin{pmatrix} A_1^{-1}(f_1 - A_{12} u_2^n) - u_1^n \\ 0 \end{pmatrix} \\
 &= \begin{pmatrix} A_1^{-1}(f_1 - A_{12} u_2^n) \\ u_2^n \end{pmatrix}
 \end{aligned}$$

Similarly, from the second relation of MS, i.e.

$$u^{n+1} = u^{n+1/2} + R_2^T A_2 R_2 (f - Au^{n+1/2})$$

we obtain

$$\begin{pmatrix} u_1^{n+1} \\ u_2^{n+1} \end{pmatrix} = \begin{pmatrix} A_1^{-1}(f_1 - A_{12} u_2^n) \\ A_2^{-1}(f_2 - A_{21} u_1^{n+1}) \end{pmatrix}$$

which can be rewritten in the equivalent form

$$A_1 u_1^{n+1} = f_1 - A_{12} u_2^n, \quad A_2 u_2^{n+1} = f_2 - A_{21} u_1^{n+1} \quad (2.6)$$

and is therefore a discretization of the alternating Schwarz method. The non-overlapping MS is also equivalent to a block Gauss Seidel method, since Eq.(2.6) leads in matrix form to the iteration :

$$\begin{bmatrix} A_1 & 0 \\ A_{21} & A_2 \end{bmatrix} \begin{pmatrix} u_1^{n+1} \\ u_2^{n+1} \end{pmatrix} = \begin{bmatrix} 0 & -A_{12} \\ 0 & 0 \end{bmatrix} \begin{pmatrix} u_1^n \\ u_2^n \end{pmatrix} + \begin{pmatrix} f_1 \\ f_2 \end{pmatrix}$$

To simplify the presentation, the global solution at each iteration of one-dimensional Poisson problem (considering only the x axis) whose variables are dimensionless is shown in Figure 2-4. It is solved by two overlapping sub-domains using MS method and is the discrete level of alternating Schwarz method.

Parallel Schwarz algorithm

P.L. Lions [45, 46, 47] gives a parallel formulation which is the basis of many domain decomposition methods. We take the values given by the neighboring domain at the previous iteration as Dirichlet conditions for a subdomain Ω_i . The computation of each sub-domain can be launched in parallel with an iterative method which solves concurrently in all subdomains, $i=1,2$ [48]:

$$\begin{cases} -\Delta(u_i^{n+1}) = f, & \text{in } \Omega_i, \\ u_i^{n+1} = u_{3-i}^n & \text{on } \gamma_i \end{cases} \quad (2.7)$$

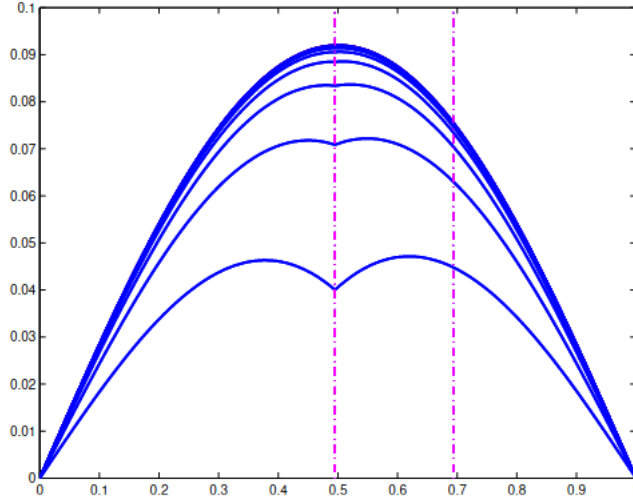


Figure 2-4: Convergence of MS method

Like the previous case, it is important to note that the convergence rate is lower than that of alternating Schwarz algorithm as shown in Figure 2-5 for one-dimensional Poisson problem.

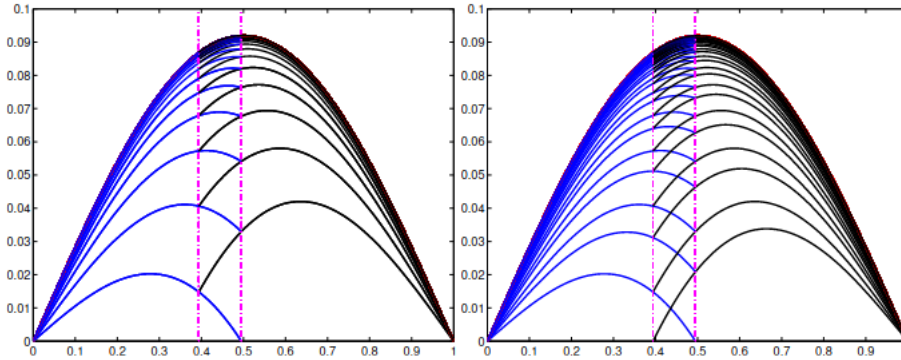


Figure 2-5: Comparison of convergence rates between alternate (left) and parallel (right) Schwarz algorithms

Additive Schwarz method

In order to understand the major invention of the Additive Schwarz (AS) method [49, 50, 51], let us consider the discretized parallel Schwarz method written in Jacobi block form which is exposed in the following. Dinh et al. [52] propose an approach that uses overlaps and remains symmetrical. This writing allows us in this case to interpret the algorithm as an iterative method for the preconditioned system [53].

Using the same notation as before, the preconditioned system is

$$(R_1^T A_1^{-1} R_1 + R_2^T A_2^{-1} R_2) A u = (R_1^T A_1^{-1} R_1 + R_2^T A_2^{-1} R_2) f$$

Writing this as a stationary iterative method yields

$$u^n = u^{n-1} + (R_1^T A_1^{-1} R_1 + R_2^T A_2^{-1} R_2)(f - Au^{n-1}) \quad (2.8)$$

If the R_j are non-overlapping, we obtain now

$$\begin{pmatrix} u_1^{n+1} \\ u_2^{n+1} \end{pmatrix} = \begin{pmatrix} A_1^{-1}(f_1 - A_{12}u_2^n) \\ A_2^{-1}(f_2 - A_{21}u_1^n) \end{pmatrix}$$

which can be rewritten in the equivalent form

$$A_1 u_1^{n+1} = f_1 - A_{12} u_2^n, \quad A_2 u_2^{n+1} = f_2 - A_{21} u_1^n \quad (2.9)$$

This is a discretization of Lions' parallel Schwarz method. AS is also equivalent to a block Jacobi method, since Eq.(2.9) leads in matrix form to the iteration

$$\begin{bmatrix} A_1 & 0 \\ 0 & A_2 \end{bmatrix} \begin{pmatrix} u_1^{n+1} \\ u_2^{n+1} \end{pmatrix} = \begin{bmatrix} 0 & -A_{12} \\ -A_{21} & 0 \end{bmatrix} \begin{pmatrix} u_1^n \\ u_2^n \end{pmatrix} + \begin{pmatrix} f_1 \\ f_2 \end{pmatrix}$$

In order to write algorithms that act on global function in $H^1(\Omega)$, we need extension operators and partitions of unity. We note E_i the extension operator such that $E_i(w_i) : \Omega \rightarrow R$ is the extension of $w_i : \Omega_i \rightarrow R$ by zero outside Ω_i . We also define the partition of unity function $\chi_i : \Omega_i \rightarrow R, \chi_i \geq 0$ and $\chi_i(x) = 0$ for $x \in \partial\Omega_i \setminus \partial\Omega$ such that

$$w = \sum_{i=1}^2 E_i(\chi_i w|_{\Omega_i}) \quad (2.10)$$

for any function $w : \Omega \rightarrow R$. We introduce a formulation in terms of the continuous residual $r^n := f + \Delta u^n$ which is closer to the algebraic definition of domain decomposition methods.

1 Compute the residual $r^n : \Omega \rightarrow R$:

$$r^n := f + \Delta(u^n)$$

2 For $i = 1, 2$ solve for a local correction v_i^n :

$$-\Delta(v_i^n) = r^n \text{ in } \Omega_i, \quad v_i^n = 0 \text{ on } \partial\Omega_i$$

3 Update u^n :

$$u^{n+1} = u^n + E_1(v_1^n) + E_2(v_2^n).$$

where $(E_i)_{i=1,2}$ define a extension operator.

Restricted Additive Schwarz method

Cai and Sarkis [54] introduced a new discrete method, the Restricted Additive Schwarz algorithm. This modification has the benefit of removing the error committed in the recovery by the additive Schwarz iteration, and the method is convergent and equivalent to the discretized parallel Schwarz method [55, 44] as is shown in Figure 2-7 the comparison between the RAS and the AS methods.

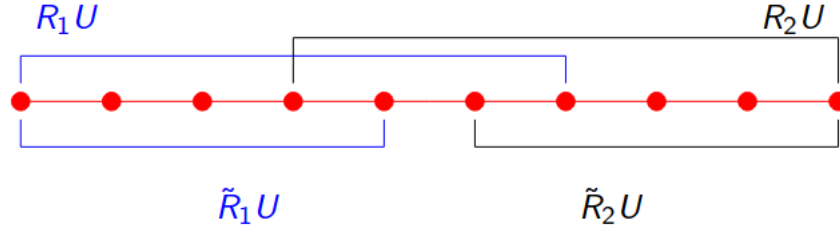


Figure 2-6: Schematic configuration of new restriction matrices

Replace R_j^T in AS by \tilde{R}_j^T , as shown in Figure 2-6:

$$u^{n+1} = u^n + (\tilde{R}_1^T A_1^{-1} R_1 + \tilde{R}_2^T A_2^{-1} R_2)(f - Au^{n-1}) \quad (2.11)$$

- 1 Compute the residual $r^n : \Omega \rightarrow R$:

$$r^n := f + \Delta(u^n) \quad (2.12)$$

- 2 For $i = 1, 2$ solve for a local correction v_i^n :

$$-\Delta(v_i^n) = r^n \text{ in } \Omega_i, \quad v_i^n = 0 \text{ on } \partial\Omega_i \quad (2.13)$$

- 3 Compute an average of the local correction and update u^n :

$$u^{n+1} = u^n + E_1(\chi_1 v_1^n) + E_2(\chi_2 v_2^n). \quad (2.14)$$

where $(\chi_i)_{i=1,2}$ define a partition of unity.

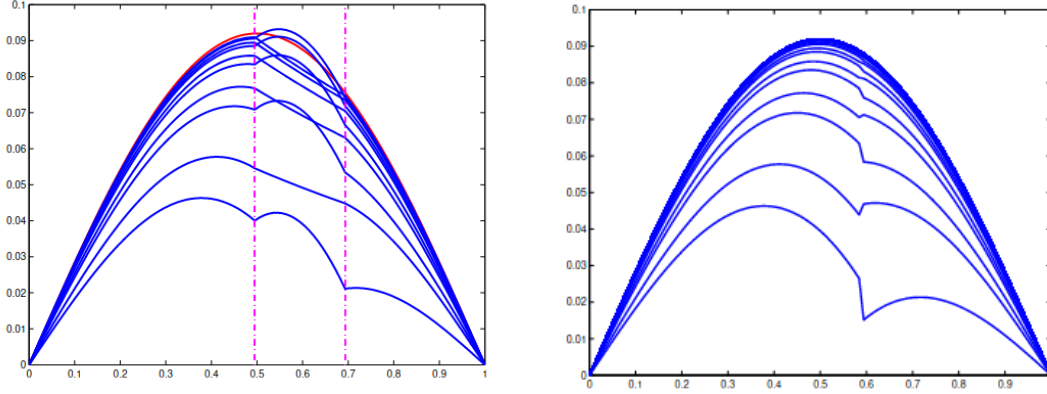


Figure 2-7: Comparison between AS (left) and RAS (right) algorithms

2.2.2 Optimized Schwarz method

The Optimized Schwarz (OS) methods are a link between the classical Schwarz methods, which work with overlap, and the Schur methods, which do not use overlays. The OS methods allow to improve significantly the convergence factors of both stationary and Krylov's methods and can be used without overlap [56]. P.L. Lions [45] proposes to replace the transmission conditions concerning the value of the function by conditions of Robin type (or Fourier in thermal), which gives the following algorithm.

Let α be a positive number, the modified algorithm reads:

$$\begin{cases} -\Delta(u_1^{n+1}) = f, & \text{in } \Omega_1, \\ \left(\frac{\partial}{\partial n_1} + \alpha\right)(u_1^{n+1}) = \left(\frac{\partial}{\partial n_1} + \alpha\right)(u_2^n) & \text{on } \gamma_1 \end{cases} \quad (2.15)$$

and

$$\begin{cases} -\Delta(u_2^{n+1}) = f, & \text{in } \Omega_2, \\ \left(\frac{\partial}{\partial n_2} + \alpha\right)(u_2^{n+1}) = \left(\frac{\partial}{\partial n_2} + \alpha\right)(u_1^n) & \text{on } \gamma_2 \end{cases} \quad (2.16)$$

Non-overlapping domain decomposition

The domain Ω is divided into two non overlapping subdomains Ω_1 and Ω_2 with interface γ . In this case, we have: $n_1 = -n_2$. The optimized Schwarz algorithm reads:

$$\begin{aligned} -\Delta u_1^{n+1} &= f, & \text{in } \Omega_1, \\ \frac{\partial u_1^{n+1}}{\partial n_1} + \alpha u_1^{n+1} &= -\frac{\partial u_2^n}{\partial n_2} + \alpha u_2^n & \text{on } \gamma \\ -\Delta u_2^{n+1} &= f, & \text{in } \Omega_2, \\ \frac{\partial u_2^{n+1}}{\partial n_2} + \alpha u_2^{n+1} &= -\frac{\partial u_1^n}{\partial n_1} + \alpha u_1^n & \text{on } \gamma \end{aligned} \quad (2.17)$$

A direct discretization would require the computation of the normal derivatives along the interface in order to evaluate the right hand side of Eq.(2.17). This can be avoided by introducing new coefficients:

$$\lambda_1^n = -\frac{\partial u_2^n}{\partial n_2} + \alpha u_2^n \quad \text{and} \quad \lambda_2^n = -\frac{\partial u_1^n}{\partial n_1} + \alpha u_1^n$$

The algorithm (2.17) becomes

$$\begin{aligned} -\Delta u_1^{n+1} &= f, \text{ in } \Omega_1, \\ \frac{\partial u_1^{n+1}}{\partial n_1} + \alpha u_1^{n+1} &= \lambda_1^n \text{ on } \gamma \\ -\Delta u_2^{n+1} &= f, \text{ in } \Omega_2, \\ \frac{\partial u_2^{n+1}}{\partial n_2} + \alpha u_2^{n+1} &= \lambda_2^n \text{ on } \gamma \end{aligned} \tag{2.18}$$

The two coefficients introduced can be updated by:

$$\begin{aligned} \lambda_1^{n+1} &:= -\frac{\partial u_2^{n+1}}{\partial n_2} + \alpha u_2^{n+1} = -\left(\frac{\partial u_2^{n+1}}{\partial n_2} + \alpha u_2^{n+1}\right) + 2\alpha u_2^{n+1} = -\lambda_2^n + 2\alpha u_2^{n+1} \\ \lambda_2^{n+1} &:= -\frac{\partial u_1^{n+1}}{\partial n_1} + \alpha u_1^{n+1} = -\left(\frac{\partial u_1^{n+1}}{\partial n_1} + \alpha u_1^{n+1}\right) + 2\alpha u_1^{n+1} = -\lambda_1^n + 2\alpha u_1^{n+1} \end{aligned} \tag{2.19}$$

Equations (2.19) can be seen as a fixed point iteration in the new variables $\lambda_j, j = 1, 2$ to solve the substructured problem

$$\begin{aligned} \lambda_1 &= -\lambda_2 + 2\alpha u_2(\lambda_2, f) \\ \lambda_2 &= -\lambda_1 + 2\alpha u_1(\lambda_1, f) \end{aligned} \tag{2.20}$$

where $u_j = u_j(\lambda_j, f), j = 1, 2$, are solutions of:

$$\begin{aligned} -\Delta u_j &= f, \text{ in } \Omega_j, \\ \frac{\partial u_j}{\partial n_j} + \alpha u_j &= \lambda_j \text{ on } \gamma \end{aligned} \tag{2.21}$$

Overlapping domain decomposition

The trick explained in the non overlapping case cant not be used in the overlapping case. Indeed, the normal derivatives are computed on two distinct interfaces. Here as well, it is possible to write an algorithm equivalent to P.L. Lion's algorithm but where the iterate is a function $u^n : \Omega \rightarrow R$.

Suppose that the domain is divided into two overlapping subdomains Ω_1 and Ω_2 with a partition of unity χ_1 and χ_2 :

$$\chi_1 + \chi_2 = 1, \text{ supp}\chi_i \subset \Omega_i, i = 1, 2$$

Let $u^n : \Omega \rightarrow R$ be an approximation to a Poisson equation. Then the update u^{n+1} is computed by the following algorithm:

1 Compute the residual $r^n : \Omega \rightarrow R$:

$$r^n := f + \Delta(u^n)$$

2 For $i = 1, 2$ solve for a local correction v_i^n :

$$\begin{aligned} -\Delta v_i^n &= r^n \text{ in } \Omega_i, \\ \left(\frac{\partial}{\partial n_i} + \alpha\right)(v_i^n) &= 0 \text{ on } \gamma_i \end{aligned}$$

3 Compute an average of the local correction and update u^n :

$$u^{n+1} = u^n + E_1(\chi_1 v_1^n) + E_2(\chi_2 v_2^n). \quad (2.22)$$

where $(\chi_i)_{i=1,2}$ and $(E_i)_{i=1,2}$ define a partition of unity as cited previously.

2.2.3 Schur complement method

The Schur methods have often been called substructuring methods. Nevertheless, the Schwarz methods can also be written in a substructured form. There are two main variants, the primal Schur method and the dual Schur method. Suppose that the domain Ω is divided into two non-intersecting subdomains Ω_1 and Ω_2 , as depicted in Figure 2-8.

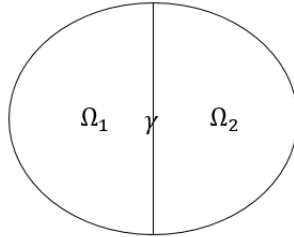


Figure 2-8: Domain divided into two non-overlapping subdomains

Let the interface between the subdomains be $\gamma = \Omega_1 \cap \Omega_2$, and $(n_i)_{i=1,2}$ be the outward normal to the interface Γ corresponding to $\Omega_{1,2}$. Local problems become [27]:

$$\begin{cases} -\Delta u_i = f, & \text{in } \Omega_i, i = 1, 2 \\ u_1 = u_2, & \text{on } \gamma, \\ \frac{\partial u_1}{\partial n_1} + \frac{\partial u_2}{\partial n_2} = 0 & \text{on } \gamma \end{cases} \quad (2.23)$$

Since the Poisson equation is a scalar second order PDEs, we have a continuity equation and an equilibrium equation on the interface. The difference between primal and dual Schur methods is listed below:

- **Primal approaches** [57]: a unique interface displacement unknown $u_\gamma = u|_\gamma$ satisfying the continuity equation is introduced, then an iterative process enables to satisfy the equilibrium equation while always verifying the Poisson equation within each sub-domain.
- **Dual approaches** [58]: a unique interface effort unknown $\lambda_\gamma = \frac{\partial u}{\partial n}|_\gamma$ satisfying the equilibrium equation is introduced, then an iterative process enables to satisfy the continuity equation while always verifying the Poisson equation within each sub-domain.

Iterative Neumann-Neumann algorithm

The process of preconditioning the primal Schur method by a dual Schur method has been presented in the literature as the Neumann-Neumann method [59]. Let u_i^n denote an approximation to the solution u in a subdomain Ω_i , $i = 1, 2$ at the iteration n . Starting from an initial guess u_i^0 , the Neumann-Neumann iteration [60] computes the approximation (u_1^{n+1}, u_2^{n+1}) by solving a local Dirichlet problem with a continuous data at the interface

$$\begin{cases} -\Delta(u_i^{n+1/2}) = f, & \text{in } \Omega_i, \\ u_i^{n+1/2} = \frac{1}{2}(u_j^n + u_i^n) & \text{on } \gamma \end{cases} \quad (2.24)$$

followed by a correction for the jump of the fluxes on the interface

$$\begin{cases} -\Delta(e_i^{n+1}) = 0, & \text{in } \Omega_i, \\ \frac{\partial e_i^{n+1}}{\partial n_i} = -\frac{1}{2}\left(\frac{\partial u_1^{n+1/2}}{\partial n_1} + \frac{\partial u_2^{n+1/2}}{\partial n_2}\right) & \text{on } \gamma \end{cases} \quad (2.25)$$

The next iteration can be calculated by

$$u_i^{n+1} = u_i^{n+1/2} + e_i^{n+1}, i = 1, 2 \quad (2.26)$$

The rationale of first step (2.24) is to satisfy the Poisson equation in the subdomains while ensuring the continuity equation on interface γ . After this step, the solution is continuous but the fluxes may not match. The jump on the fluxes is corrected after the step(2.25). The Neumann-Neumann method is a primal one which relax the equilibrium equation.

Iterative FETI algorithm

Farhat and Roux [58] propose a method, the Finite Element Tearing and Interconnect (FETI) method which is basically a dual Schur method, but in its original formulation it is written in variational form.

Let u_i^n denote an approximation of the solution u in a subdomain Ω_i , $i = 1, 2$ at the iteration n . Starting from the initial guess u_i^0 , FETI iteration computes the approximation (u_1^{n+1}, u_2^{n+1}) by first

correcting the jump of the flux on the interface

$$\begin{cases} -\Delta(u_i^{n+1/2}) = f, & \text{in } \Omega_i, \\ \frac{\partial u_i^{n+1/2}}{\partial n_i} = \frac{\partial u_i^n}{\partial n_i} - \frac{1}{2} \left(\frac{\partial u_1^n}{\partial n_1} + \frac{\partial u_2^n}{\partial n_2} \right) & \text{on } \gamma \end{cases} \quad (2.27)$$

followed by a correction of the continuity equation:

$$\begin{cases} -\Delta(e_i^{n+1}) = 0, & \text{in } \Omega_i, \\ e_i^{n+1} = \frac{1}{2}(u_j^{n+1/2} - u_i^{n+1/2}) & \text{on } \gamma \text{ for } j \neq i \end{cases} \quad (2.28)$$

then the next iteration is computed by:

$$u_i^{n+1} = u_i^{n+1/2} + e_i^{n+1}, i = 1, 2 \quad (2.29)$$

This is a dual method which ensuring firstly the equilibrium equation, then the continuity one is corrected by Eqs.(2.28).

Iterative Dirichlet-Neumann algorithm

The iterative Dirichlet-Neumann algorithm is based on two fractional steps [61, 62]. Given an initial guess u_γ^0 , we first solve a Dirichlet problem in Ω_1 with Dirichlet data u_γ^0 on γ ,

$$(D) \begin{cases} -\Delta(u_1^{n+1/2}) = f, & \text{in } \Omega_1, \\ u_1^{n+1/2} = u_\gamma^n & \text{on } \gamma \end{cases} \quad (2.30)$$

and then a mixed Neumann-Dirichlet problem in Ω_2 with a Neumann condition on the interface determined by solution of Ω_1 obtained in the previous step.

$$(N) \begin{cases} -\Delta(u_2^{n+1}) = f, & \text{in } \Omega_2, \\ \frac{\partial u_2^{n+1}}{\partial n_2} = -\frac{\partial u_1^{n+1/2}}{\partial n_1} & \text{on } \gamma \end{cases} \quad (2.31)$$

then the next iteration can be given by introducing a relaxation coefficient θ

$$u_\gamma^{n+1} = \theta u_2^{n+1} + (1 - \theta) u_\gamma^n \quad (2.32)$$

with $\theta \in (0, \theta_{max})$.

Since the current work focus on coupling of SC/CFD, computational time of CFD code is dominant and thus the coupling does not need to be parallel. For the case with overlap, Schwarz alternating method is chose from the continuous viewpoint, which has a faster convergence rate than the parallel Schwarz method. At the discrete level, the corresponding multiplicative Schwarz

method is applied. The convergence rate depends on the width of the overlap, which varies with different cases, while in the present study, the width is fixed to $0.2D_h$ based on disturbed length (simulation experience), with D_h the hydraulic diameter.

For the case without overlap, the Dirichlet-Neumann method is more suitable for the coupling work based on available types of boundary conditions for each solver. While it should be noted that in contrast to Eqs.(2.30) and (2.31) where Dirichlet and Neumann conditions are applied to all variables, Neumann boundary is only applied to the transferred pressure variable and Dirichlet condition is only applied to the velocity in current study using classical boundary conditions available in each code.

After the determination of transmission conditions required for each case to obtain global convergent solution, we may consider whether there is an efficient iterative algorithm with a higher convergence rate to search for an approximate solution from a Krylov subspace. The following, some most famous Krylov subspace methods are presented.

2.2.4 Accelerants: Krylov methods

The aim of this section is to present Krylov type methods using domain decomposition methods as pre-conditioners, such as Richardson or Conjugate Gradient (CG) methods. They have higher convergence rates compared to fixed-point method. Consider the following well-posed but difficult to solve linear system

$$Ax = b, x \in R^N$$

We write $A = M - N$, with M an "easy to invert" matrix of the same size than A. Then

$$Mx = Nx + b$$

An iterative way writes

$$\begin{aligned} Mx^{n+1} &= Nx^n + b \\ &= Mx^n + b - Ax^n \\ &= Mx^n + r^n \end{aligned} \tag{2.33}$$

with the residual vector $r^n = b - Ax^n$.

Fixed point iterations

The following algorithm equivalent to Eq.(2.33)

$$x^{n+1} = x^n + M^{-1}r^n \tag{2.34}$$

is called a fixed point algorithm and the solution x is a fixed point of the operator:

$$x \mapsto x + M^{-1}(b - Ax)$$

From Eq.(2.33), one can see that

$$\begin{aligned} x^{n+1} &= M^{-1}(Nx^n + b) \\ &= M^{-1}(Nx^n + Mx - Nx) \\ &= x + M^{-1}N(x^n - x) \end{aligned}$$

We define the error vector $e^n := x^n - x$, it is obvious that

$$e^{n+1} = M^{-1}Ne^n$$

thus

$$e^{n+1} = (M^{-1}N)^{n+1}e^0 \tag{2.35}$$

The iteration converge if and only if the spectral radius of the iteration matrix is inferior to 1, that is $\rho(M^{-1}N) < 1$ where

$$\rho(B) = \max\{|\lambda|, \lambda \text{ eigenvalue of } B\}$$

Krylov spaces

In this part, we will show that the solution of a fixed point method belongs to an affine space called Krylov space [63]. We define a new residual

$$z^n := M^{-1}r^n$$

at the iteration n for the fixed point iteration

$$x^{n+1} = x^n + z^n$$

Then, the fixed point iteration is equivalent to

$$x^{n+1} = x^0 + \sum_{i=0}^n (M^{-1}N)^i z^0 \tag{2.36}$$

The correction $x^{n+1} - x^0$ is given by

$$x^{n+1} - x^0 = S_n(M^{-1}N)z^0$$

where S_n is the polynomial given by $S_n(t) = 1 + t + \dots + t^n$. Moreover, we see that

$$x^{n+1} - x^0 \in \text{Span}\{z^0, (M^{-1}N)z^0, \dots, (M^{-1}N)^n z^0\} \quad (2.37)$$

In conclusion, the solution of a fixed point iteration is generated in a space spanned by powers of the iteration matrix $M^{-1}N = I - M^{-1}A$ applied to a given vector. For a given matrix B and a vector y , we define the Krylov subspaces of dimension n associated to B and y by

$$\kappa^n(B, y) := \text{Span}\{y, By, \dots, B^{n-1}y\}$$

Therefore, a Krylov space is a space of polynomials of a matrix times a vector. According to Eq.(2.37), we have

$$x^{n+1} - x^0 \in \kappa^n(M^{-1}N, z^0)$$

By the same way, we see from Eq.(2.35)

$$e^n \in \kappa^{n+1}(M^{-1}N, e^0)$$

Besides, through Eq.(2.36), it can be inferred that

$$z^n = x^{n+1} - x^n = (M^{-1}N)^n z^0 \Rightarrow z^n \in \kappa^{n+1}(M^{-1}N, z^0)$$

Richardson iteration

We consider the equation (2.34), a more general iteration scheme may be obtained by using a relaxation parameter $\alpha \in R$, which should have the effect of accelerating convergence [64]:

$$x^{n+1} = x^n + \alpha M^{-1}r^n$$

We have

$$\begin{aligned} Mx^{n+1} &= Mx^n + \alpha(b - Ax^n) \\ &= (M - \alpha A)x^n + \alpha b \\ &= ((1 - \alpha)M + \alpha N)x^n + \alpha b \end{aligned} \quad (2.38)$$

The iteration matrix can be defined as

$$B := M^{-1}((1 - \alpha)M + \alpha N) = I - \alpha M^{-1}A$$

Consequently

$$\begin{aligned} e^{n+1} &= B e^n \\ e^n &= B^n e^0 \end{aligned}$$

The parameter α can be chosen in such a way to have the best convergence factor over the iterations. In the case of a symmetric positive definite matrix, the value of α which minimizes the convergence rate is

$$\alpha_{opt} = \frac{2}{\lambda_{min}(A) + \lambda_{max}(A)}$$

Gradient methods

This defines a new class of methods for symmetric positive matrices. A decent method is an iteration of the form

$$x^{n+1} = x^n + \alpha_n p^n, \alpha_n \geq 0$$

where α_n is chosen such that it minimizes $\|e^{n+1}\|_A^2 = \|x^{n+1} - x\|_A^2$ (the square of the A-norm for the error at each iteration, $\|e^{n+1}\|_A^2 := (Ae^{n+1}, e^{n+1})_2$) and vector p^n is called the descent direction. If $p^n = r^n$, the resulting method is called optimal gradient method.

Consider function f :

$$\alpha \mapsto f(\alpha) := \|x^n + \alpha p^n - x\|_A^2$$

and the minimization problem

$$\begin{aligned} f(\alpha_n) &= \min_{\alpha} (A(x^n + \alpha p^n - x), x^n + \alpha p^n - x) \\ &= \min_{\alpha} [\alpha^2 (Ap^n, p^n) + 2\alpha (Ap^n, x^n - x) + (A(x^n - x), x^n - x)] \\ &= \min_{\alpha} [\alpha^2 (Ap^n, p^n) - 2\alpha (p^n, A(x - x^n))] + (A(x^n - x), x^n - x) \end{aligned}$$

We have the optimal parameter α_n which is characterized by:

$$\frac{\partial f}{\partial \alpha}(\alpha_n) = 0 \Rightarrow \alpha_n = \frac{(p^n, r^n)}{(Ap^n, p^n)} \quad (2.39)$$

A Krylov method is presented here that applies to symmetric positive definite (SPD) matrices A. The idea is that the solution at each iteration solves a minimization problem in the A-norm over a Krylov space:

Find $y^n \in \kappa^n(A, r^0)$ such that

$$\|e^n\|_A = \|x - x^n\|_A = \min_{w \in \kappa^n(A, r^0)} \|x - (x_0 + w)\|_A$$

In the following, we will define a new method that extends the idea of gradient methods. Starting

from an initial guess x^0 and an initial decent direction $p^0 = r^0 = b - Ax^0$, a conjugate gradient method [65] is an iteration of the form

$$\begin{aligned} x^{n+1} &= x^n + \alpha_n p^n \\ r^{n+1} &= r^n - \alpha_n A p^n \\ p^{n+1} &= r^{n+1} + \beta_{n+1} p^n \end{aligned} \quad (2.40)$$

Until r^{n+1} is sufficiently small. Where α_n and β_n are chosen such that they minimize the norm of the error $\|e^{n+1}\|_A^2 = \|x^{n+1} - x\|_A^2$ at each iteration.

It remains to find expressions of α_n and β_{n+1} . Firstly for α_n , by taking the dot product of the second relation of Eqs.(2.40) by p^n and by using Eq.(2.39), we see that

$$(r^{n+1}, p^n) = (r^n, p^n) - \alpha_n (A p^n, p^n) = 0$$

By taking the dot product of the third relation of Eqs.(2.40) by r^{n+1} and by using the previous orthogonality relation, we obtain

$$(p^{n+1}, r^{n+1}) = (r^{n+1}, r^{n+1}) + \beta_{n+1} (r^{n+1}, p^n) = (r^{n+1}, r^{n+1}), \forall n \geq 0.$$

Replacing the last relation taken in n into Eq.(2.39) we get

$$\alpha_n = \frac{(r^n, r^n)}{(A p^n, p^n)} = \frac{\|r^n\|_2^2}{\|p^n\|_A^2} \quad (2.41)$$

To calculate β_{n+1} , we can replace the Eq.(2.41) taken in n+1 into $\|e^{n+2}\|_A^2$ and use the third relation of Eqs.(2.40) to replace p^{n+1}

$$\begin{aligned} \|e^{n+2}\|_A^2 &= \|e^{n+1} + \alpha_{n+1} p^{n+1}\|_A^2 \\ &= \|e^{n+1}\|_A^2 + 2(A e^{n+1}, \alpha_{n+1} p^{n+1}) + \alpha_{n+1}^2 \|p^{n+1}\|_A^2 \\ &= \|e^{n+1}\|_A^2 - 2\alpha_{n+1} (r^{n+1}, r^{n+1}) + \alpha_{n+1}^2 \|p^{n+1}\|_A^2 \\ &= \|e^{n+1}\|_A^2 - \frac{(r^{n+1}, r^{n+1})^2}{(A p^{n+1}, p^{n+1})} \\ &= \|e^{n+1}\|_A^2 - \frac{(r^{n+1}, r^{n+1})^2}{(A(r^{n+1} + \beta_{n+1} p^n), (r^{n+1} + \beta_{n+1} p^n))} \end{aligned}$$

Therefore, it is equivalent to minimize the norm $(A(r^{n+1} + \beta_{n+1} p^n), (r^{n+1} + \beta_{n+1} p^n))$ with respect to β_{n+1} . Following the same way to calculate Eq.(2.39), we can obtain

$$\beta_{n+1} = -\frac{(A r^{n+1}, p^n)}{(A p^n, p^n)} \quad (2.42)$$

By taking the A-dot product of the third relation of Eqs.(2.40) by p^n and with the equation of Eq.(2.42), we get

$$(Ap^{n+1}, p^n) = (Ar^{n+1}, p^n) + \beta_{n+1}(Ap^n, p^n) = 0$$

Using this identity and taking the A-dot product of the third relation of Eqs.(2.40) by p^{n+1} , one have

$$(Ap^{n+1}, p^{n+1}) = (Ar^{n+1}, p^{n+1}) + \beta_{n+1}(Ap^{n+1}, p^n) = (Ap^{n+1}, r^{n+1}) \quad (2.43)$$

Using Eq.(2.43) into the dot product of the second relation of Eqs.(2.40) by r^n

$$(r^{n+1}, r^n) = (r^n, r^n) - \alpha_n(Ap^n, r^n) = (r^n, r^n) - \alpha_n(Ap^n, p^n) = 0 \quad (2.44)$$

Finally, taking the dot product of the second relation of Eqs.(2.40) by r^{n+1} and with Eq.(2.44)

$$(r^{n+1}, Ap^n) = -\frac{\|r^{n+1}\|_2^2}{\alpha_n} \quad (2.45)$$

Plugging Eq.(2.45) into Eq.(2.42) we conclude by using the expression of Eq.(2.41) that

$$\beta_{n+1} = \frac{\|r^{n+1}\|_2^2}{\|r^n\|_2^2} \quad (2.46)$$

Toti et al. [30] has applied the Richardson iteration in his STH/CFD coupling for multi-scale simulations of pool-type reactors where one-cell value obtained by the STH code and the surface average value of CFD code are concerned; while current work focus on flow simulations in an assembly between CFD and SC codes, the coupling interface is more complex since more cell values should be considered during the data exchange. The gain between Richardson and fixed-point iterations is not significant, consequently, only the latter is taken into account currently.

For the SC/CFD coupling, one important aspect is the treatment of different mesh refinements during data exchange between two solvers. The Local Defect Correction (LDC) methods can explain the way to improve global solution based on local discretizations. More precisely, it contains the data treatment from coarse domain to fine one and vice versa.

2.3 Different mesh refinements: LDC methods

In this section, we present some LDC methods [66] using domain decomposition methods as preconditioners to consider different mesh refinements between two subdomains, which consist of prolongation and restriction procedures [67]. We briefly recall the local defect correction method

applied to the boundary value:

$$\begin{cases} Lu = f \text{ in } \Omega \\ Bu = g \text{ on } \Gamma = \partial\Omega \text{ (boundary condition)} \end{cases} \quad (2.47)$$

Where L is a second order elliptic operator. Let

$$L_h u_h = f_h \quad (2.48)$$

be a discretization (by finite difference or finite elements) with mesh parameter h [68]. The usual multi-grid iteration:

smoothing step:

u_h^i : given i -th iterate

\tilde{u}_h result of v steps of some smoothing iteration applied to u_h^i

coarse-grid correction:

$d_h := L_h \tilde{u}_h - f_h$ (defect of u_h)

$d_{2h} := r d_h$ (r : restriction)

v_{2h} : solution of $L_{2h} v_{2h} = d_{2h}$

$u_h^{i+1} := u_h^i - p v_{2h}$ (p :prolongation)

2.3.1 Model case of decomposition into two domains

There are two different strategies based on the type of domain decomposition. First one can decompose the domain Ω into two or several disjunct subdomains. Figure 2-2 shows the situation with two subdomains Ω^l and Ω^r connected by the interface $\Gamma = \partial\Omega^l \cap \partial\Omega^r$. The equations can be expressed as:

$$\begin{cases} Lu^l = f \text{ in } \Omega^l, Bu^l = g \text{ on } \partial\Omega^l \setminus \Gamma \\ Lu^r = f \text{ in } \Omega^r, Bu^r = g \text{ on } \partial\Omega^r \setminus \Gamma \\ u^l = u^r \text{ on } \Gamma \\ \frac{\partial u^l}{\partial n^l} + \frac{\partial u^r}{\partial n^r} = 0 \text{ on } \Gamma \end{cases} \quad (2.49)$$

Where (n^l, n^r) is outer normal direction with respect to (Ω^l, Ω^r) .

The second approach uses overlapping subdomains. In the situation of Figure 2-2, two computational domains are partially overlapping with two boundaries: $\Gamma^l = \partial\Omega^r \setminus \partial\Omega$ and $\Gamma^r = \partial\Omega^l \setminus \partial\Omega$.

Any solution of Eqs.(2.47) gives rise to solution $u^l = u|_{\Omega^l}, u^r = u|_{\Omega^r}$ of

$$\begin{cases} Lu^l = f \text{ in } \Omega^l, Bu^l = g \text{ on } \partial\Omega^l \setminus \Gamma^l, \\ Lu^r = f \text{ in } \Omega^r, Bu^r = g \text{ on } \partial\Omega^r \setminus \Gamma^r, \\ u^l = u^r \text{ on } \Gamma^l, u^r = u^l \text{ on } \Gamma^r \end{cases} \quad (2.50)$$

On the other hand, any pair of solution u^l, u^r of Eqs.(2.50) coincides with the restriction of u from Eqs.(2.47) to Ω^l and Ω^r , provided that the boundary value problem in $\Omega^l \cap \Omega^r$ is uniquely solvable.

A discretization of Eqs.(2.50) is represented by

$$\begin{cases} L_h^l u_h^l = f_h^l \text{ in } \Omega_h^l, L_h^r u_h^r = f_h^r \text{ in } \Omega_h^r, \\ u_h^l = \gamma^l u_h^r \text{ on } \Gamma_h^l, u_h^r = \gamma^r u_h^l \text{ on } \Gamma_h^r \end{cases} \quad (2.51)$$

Where $\gamma^l u_h^r$ denotes the interpolation of the grid function u_h^r at points of the discrete boundary Γ_h^l . We permit different grids or different kinds of discretization in $\Omega_h^l \cap \Omega_h^r$ and $\Omega_h^r \cap \Omega_h^l$. As a consequence, there are two possibly different solutions in $\Omega^l \cap \Omega^r$.

Domain decomposition methods with non-intersecting subdomains are presented by Bjorstad-Widlund [69] and Dryja [70]. In these papers, the local problems are solved directly, while the global system is solved iteratively by conjugate gradient methods.

Overlapping subdomains are used by Starius [71], Glowinski-Periaux-Dinh [72], and Hackbusch [73]. Starius applies the Schwarz algorithm. The converging algorithm is the following iterations:

- (A1) find $u_h^{l,i+1}$ solution in Ω_h^l with the boundary condition $u_h^{l,i+1} = u_h^{r,i}$ on Γ_h^l ,
- (A2) find $u_h^{r,i+1}$ solution in Ω_h^r with the boundary condition $u_h^{r,i+1} = u_h^{l,i+1}$ on Γ_h^r ,
- (A3) repeat (A1)-(A2).

2.3.2 Multi-grid method for domain decomposition

We shall describe a multi-grid algorithm [74] for solving the coupled discrete equations (2.51). It fulfills the following requirements:

- (a) If there exists multi-grid software for the local problems in Ω_h^l and Ω_h^r , it should be possible to use them inside the global program with at most slight modifications.
- (b) The computation of the different local problems should be as independent as possible.

Requirement (a) is convenient since we can test the local problems first. Requirement (b) enables us to compute the program by parallel processors.

We consider the most general problem

$$\begin{cases} L_h^l u_h^l = f_h^l \text{ in } \Omega_h^l, L_h^r u_h^r = f_h^r \text{ in } \Omega_h^r, \\ u_h^l - \gamma^l u_h^r = g_h^l \text{ on } \Gamma_h^l, u_h^r - \gamma^r u_h^l = g_h^r \text{ on } \Gamma_h^r \end{cases} \quad (2.52)$$

with inhomogeneous boundary conditions. For $g_h^l = 0, g_h^r = 0$ we regain Eqs.(2.51). g_h^l and g_h^r describe jump conditions. We introduce the notations

$$u_h := (u_h^l, u_h^r), f_h := (f_h^l, f_h^r, g_h^l, g_h^r)$$

and abbreviate the system (2.52) by

$$A_h u_h = f_h \quad (2.53)$$

The defect of a given approximation \tilde{u}_h is $d_h = A_h \tilde{u}_h - f_h$. The exact solution of Eq.(2.53) can be written as $\tilde{u}_h - A_h^{-1} d_h$. The coarse-grid correction of the multi-grid iteration approximates $\tilde{u}_h - A_h^{-1} d_h$ by

$$\tilde{u}_h - p A_{2h}^{-1} r d_h$$

where p describes the (e.g. piecewise linear) interpolation

$$p u_{2h} = (p^l u_{2h}^l, p^r u_{2h}^r)$$

of coarse-grid functions in $\Omega_{2h}^l \times \Omega_{2h}^r$, while $r f_h$ represents the restriction of quadruple $f_h = (f_h^l, f_h^r, g_h^l, g_h^r)$ into coarse-grid data

$$r f_h = (f_{2h}^l, f_{2h}^r, g_{2h}^l, g_{2h}^r) = (r_\Omega^l f_h^l, r_\Omega^r f_h^r, r_\gamma^l g_h^l, r_\gamma^r g_h^r)$$

The multi-grid algorithm can be expressed as

(B1) set $u_h^{l,i+1} := \gamma^l u_h^{r,i} + g_h^l$ on Γ_h^l

(B2) perform one smoothing step, solving $L_h^l u_h^{l,i+1} = f_h^l$

(B3) set $u_h^{r,i+1} := \gamma^r u_h^{l,i+1} + g_h^r$ on Γ_h^r

(B4) perform one smoothing step, solving $L_h^r u_h^{r,i+1} = f_h^r$

Given a multi-grid algorithm for solving the local problem $L_h u_h^l = f_h^l$ with fixed boundary data on Γ_h^l , one can use its subroutines (for computing the smoothing iteration, the defect $d_h^l = L_h^l u_h^l - f_h^l$, its restriction $r_\Omega^l d_h^l$, the prolongation p^l) in a multi-grid program for the coupled problem (2.52). One has to add a description of the interpolation Γ^l and of the restriction r_i^l . Therefore, requirement (a) mentioned in the beginning of this section is fulfilled. However, requirement (b) is not satisfactorily satisfied, steps cannot be computed in parallel.

We propose to use the following multi-grid algorithm. Let $u_h^{old} = (u_h^{l,old}, u_h^{r,old})$ be a starting guess.

- (C1) set $u_h^l = \gamma^l u_h^{r,old} + g_h^l$ on Γ_h^l , $u_h^r = \gamma^r u_h^{l,old} + g_h^r$ on Γ_h^r ;
- (C2) apply v smoothing steps $u_h^{l,0} = u_h^l \mapsto u_h^{l,1} \mapsto \dots \mapsto u_h^{l,v}$ to the left sub-problem with fixed boundary values on Γ_h^l ;
- (C3) apply the same procedure to the right sub-problem;
- (C4) proceed with $u_h^{new} = (u_h^{l,v}, u_h^{r,v})$.

Requirement (b) is now satisfied. The only coupling is the interpolation in the first step. Note that we need this interpolation only once and not v -times as in (B).

Although multi-grid algorithms (B) and (C) seem to be very similar, there is a great difference. In the latter case, the boundary values (and thereby their errors) remain fixed. Hence, $v \rightarrow \infty$ does not imply convergence of the solution of $A_h u_h = f_h$ as in the case of (B). Nonetheless, the multi-grid iteration converges. We do not want to give a proof, but we try to explain why the errors on Γ_h^r and Γ_h^l do not disturb the multi-grid convergence. For that reason, assume that the local problems are resolved exactly (i.e. $v = \infty$):

- (D1) set u_h^l and u_h^r as in (C1);
- (D2) solve the subproblems with boundary data exactly.

Two steps of (D) corresponds to one iteration of the Schwarz method. One can show that the Schwarz iterations is fast convergent with respect to high frequency components. The corresponding convergence rate depends on the width of the overlapping. Smooth errors converge slowly, but they are reduced by the coarse-grid correction.

2.3.3 Multigrid data exchange methods

The principle of domain decomposition is relatively simple. The computational domain is divided into subdomains on which the original problem is reformulated in order to couple the solutions via appropriate conditions on the interfaces. To simply present the multi-grid method [75, 76], only two nested grids are considered: a "coarse" grid G_c with a discretization step h_c and a "fine" grid G_f such that $h_f < h_c$. Generally speaking, a two-grid scheme can be divided into two steps [77]:

- *A descent or prolongation step* [78] from a coarse grid G_c to a fine grid G_f . At this stage, an estimation of the solution on the coarse grid has already been calculated. This stage consists in establishing boundary conditions on the boundary Γ_f of the fine grid by interpolation and in solving the discrete problem associated with the fine Grid.
- *An ascent or restriction step* from a fine grid G_f to a coarse grid G_c . The solution on the coarse grid is corrected by the solution obtained on G_f . This correction can be either a simple local restriction on the solution or a local restriction on the defect.

Restriction procedure

The restriction step is relatively easy compared to prolongation step, just the homogenization needs to be applied in the corresponding region of fine domain. At CFD scale, considering the statistically average Navier-Stokes equations, thus the mass, momentum and energy equations are written :

$$\frac{\partial}{\partial t}(\rho) + \frac{\partial}{\partial x_i}(\rho U_i) = 0 \quad (2.54)$$

with ρ , U , the density and the mean velocity. The momentum balance equation is written :

$$\frac{\partial}{\partial t}(\rho U_i) + \frac{\partial}{\partial x_j}(\rho U_i U_j) = \frac{\partial}{\partial x_j}(\tau_{ij} + \Sigma_{ij}^{Re}) - \frac{\partial P}{\partial x_i} + \rho g_i \quad (2.55)$$

with :

P the mean pressure;

g_i the gravity;

$\tau_{ij} = \mu \left(\frac{\partial U_i}{\partial x_j} + \frac{\partial U_j}{\partial x_i} - \frac{2}{3} \text{div}(U) \delta_{ij} \right)$ the viscous stress tensor;

μ the dynamic viscosity;

$\Sigma_{ij}^{Re} = -\rho \langle U'_i U'_j \rangle$, the turbulent stress tensor;

The energy balance equation considered for the total enthalpy $H = e + \frac{1}{2}u^2 + \frac{P}{\rho}$ is written :

$$\frac{\partial \rho H}{\partial t} + \frac{\partial}{\partial x_j}(\rho H U_j) = -\frac{\partial}{\partial x_j}(Q_j) + \frac{\partial P}{\partial t}$$

with $Q = -\lambda \nabla T$ and the thermal conductivity λ which contains both molecular and turbulent contributions.

At the subchannel scale, we can apply a volume average $\langle \rangle$ to the above equations which become :

$$\phi \frac{\partial}{\partial t}(\langle \rho \rangle) + \frac{\partial}{\partial x_i}(\phi \langle \rho \rangle \{U_i\}) = 0$$

$$\phi \frac{\partial}{\partial t}(\langle \rho \rangle \{U_i\}) + \frac{\partial}{\partial x_j}(\phi \langle \rho \rangle \{U_i\} \{U_j\}) = \frac{\partial}{\partial x_j}(\phi \langle \tau_{ij} \rangle + \langle \Sigma_{ij}^{Re} \rangle) - \phi \frac{\partial \langle P \rangle}{\partial x_i} + \phi \langle \rho \rangle g_i - \frac{\partial \phi \langle \rho \rangle \{ \delta U_i \delta U_j \}}{\partial x_j} - \langle \delta p n_i \delta_w \rangle$$

$$\phi \frac{\partial \langle \rho \rangle \{H\}}{\partial t} + \frac{\partial}{\partial x_j}(\phi \langle \rho \rangle \{H\} \{U_j\}) = -\langle \frac{\partial}{\partial x_j}(Q_j) \rangle + \phi \frac{\partial \langle P \rangle}{\partial t}$$

with ϕ the porosity. The spatial deviation is expressed as :

$$\delta A = A - \langle A \rangle$$

and the average weighted by density as $\{B\} = \frac{\langle \rho B \rangle}{\langle \rho \rangle}$ with $B = \{B\} + \delta B$.

Additional terms appear after the application of the volume average which are the dispersion $\frac{\partial \phi \langle \rho \rangle \{ \delta U_i \delta U_j \}}{\partial x_j}$ and the drag $\langle \delta p n_i \delta_w \rangle$ for example. Thus, in the context of coupling between two different scales, it is important to reduce as much as possible the discontinuity at the interface. It can be considered to keep the velocity profile in the CFD domain which usually has a non-uniform profile at a fully developed domain.

Here, we consider that data transferred to SC solver are defined exactly at the position of coupling interface. When passing pressure and velocity data from CFD code to SC code at a given sub-channel interface S_c which consists of n hydraulic interface S_f in the related CFD grid, surface-averaged values are computed:

$$U_c = \frac{1}{S_c} \int_{S_f \in S_c} U_f dS_f = \frac{\sum_{i=1}^n U_i S_{f,i}}{\sum_{i=1}^n S_{f,i}}$$

When the velocity is defined at the cell center, the volume average may be required. The restriction procedure inevitably leads to a loss of information on the 3D profiles, reason why the ideal locations of the interfaces are regions where no significant gradients of field variables are present in coupling implementation. For what concerns data transformation in opposite direction, from sub-channel code to CFD code [36], a number of up-scaling assumptions may be taken into account.

Prolongation procedure

The challenge is then to find an adequate projection operator on the interfaces between the grids. This difficulty becomes important when it comes to interpolating under constraints (here $\nabla \cdot U = 0$). The question is whether there are accurate and conservative operators. In a general way, the interpolations are said to be conservative when the flows (of mass, momentum or heat) passing the interface are determined from the neighbouring grid by a local balance or projection technique [79, 80]. In contrast, the non-conservative interpolations are based on mathematical principles (like Lagrange interpolations). Current work focus on the conservative way since it is important to guarantee the flow conservation between two sides of coupling interface. One should notice that the SC solver uses only structured grid, while the mesh of CFD code can be any type.

Next, a new method proposed for multi-domain computation [81] will be presented. Only the 2D case is considered for simplification. Variation of field variables between neighbouring cells is considered to be linear, which is a common way in the literature. We start with regular grids to

present the accurate operators.

-Regular grids

In this part, mesh density of coarse domain is uniform, while that of fine domain can be different (e.g. progressive mesh density). To introduce more clearly, we choose a case where ratio of cell sizes between coarse and fine domains is an integer.

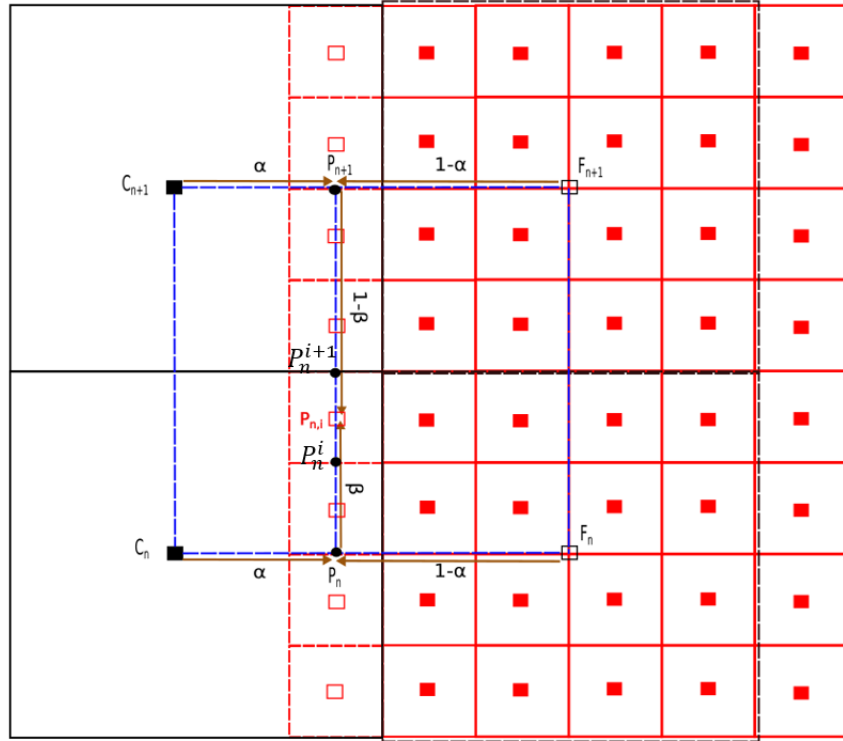


Figure 2-9: Prolongation for fictive cell-centred variables of fine domain

Projection operator The concept of fictive cells [81] is widely used in structured grid, and it also provides advantages to an unstructured grid. The object of fictive cells is to simplify the calculation of flux, gradients, dissipation, etc., on boundary conditions. As indicated in Figure 2-9, the fictive cells designated by black dashed lines belong to coarse domain and that symbolized by red dashed lines are part of fine domain.

It is possible that physical variables are not defined at the same position of the grid within a code. For example, scalar variables (pressure, density, temperature, etc.) are cell-centered values, and vector variables (velocity, etc.) are defined at the surface of each cell. Firstly, we consider the case where velocity is a cell-centered value. In Figure 2-9, C_n and C_{n+1} are results of coarse domain, F_n and F_{n+1} are fictive cell values of coarse domain which are obtained by surface average of all fine cell values contained in each fictive coarse cell.

To implement the interpolation, a dual cell (designed by blue dashed lines) is constructed based on two coarse cell values and two corresponding fictive coarse cell values. Dual cells are staggered with real coarse cells, and velocity field $U(x,y)$ is bilinear over there. Supposing that coarse domain has M cells at the coupling interface, and fine domain has N_n (for $n= 0, \dots, M$) fine cells for each coarse dual cell, noted that there are $M+1$ dual cells. Then velocities at intersections between lines $C_n F_n$, $C_{n+1} F_{n+1}$ and the line where fictive fine cell centers locate can be expressed as:

$$\begin{aligned} U(P_n) &= \alpha U(C_n) + (1 - \alpha)U(F_n) \\ U(P_{n+1}) &= \alpha U(C_{n+1}) + (1 - \alpha)U(F_{n+1}) \end{aligned}$$

For $n = 1, \dots, M-1$, with $\alpha = \frac{|P_n F_n|}{|C_n F_n|}$. In the same way:

$$U(P_{n,i}) = \beta U(P_n) + (1 - \beta)U(P_{n+1})$$

For $i = 1, \dots, N_n$, with $\beta = \frac{|P_{n,i} P_{n+1}|}{|P_n P_{n+1}|}$. Finally

$$U(P_{n,i}) = \alpha\beta U(C_n) + \beta(1 - \alpha)U(F_n) + \alpha(1 - \beta)U(C_{n+1}) + (1 - \alpha)(1 - \beta)U(F_{n+1})$$

Besides, two particular points should be considered: one point is that at the top/bottom of the domain, the velocity field in each semi dual-cell is calculated through extrapolation of the neighboring dual cell.

$$\begin{aligned} U(P_{0,i}) &= (U(P_1) - U(P_2)) \frac{|P_1 P_{0,i}|}{|P_1 P_2|} + U(P_1) \quad i = 1, \dots, N_0 \\ U(P_{M,i}) &= (U(P_M) - U(P_{M-1})) \frac{|P_M P_{M,i}|}{|P_M P_{M-1}|} + U(P_M) \quad i = 1, \dots, N_M \end{aligned}$$

The other particular point where one fictive fine cell belongs to two successive dual cells can take place (see Figure 2-10). In this case, the fictive cell is divided into two fictive cells, part of each dual cell individually. It can be concluded that

$$U(P'_{n,N_n}) = \frac{U(P_{n+1,1})L_1 + U(P_{n,N_n})L_2}{L_1 + L_2} \quad (2.56)$$

Where $U(P_{n+1,1})$ and $U(P_{n,N_n})$ could be calculated as cited previously. For the case where velocity is defined at the surface center of each cell, as exhibited in Figure 2-11, the prolongation can be performed in the same way, no more details will be presented here.

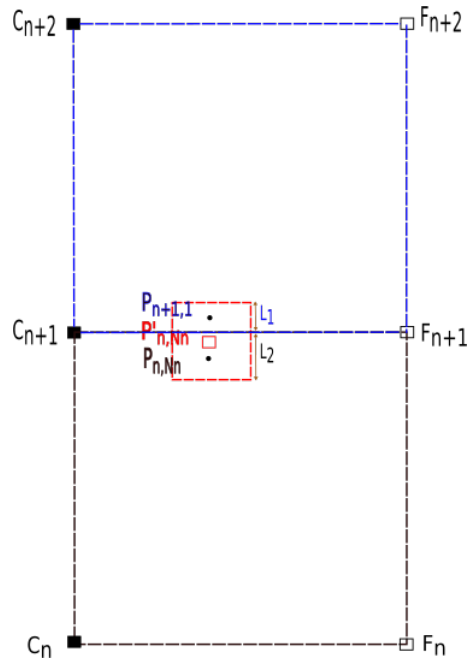


Figure 2-10: Definition of fictive fine cell value at the junction of two dual cells

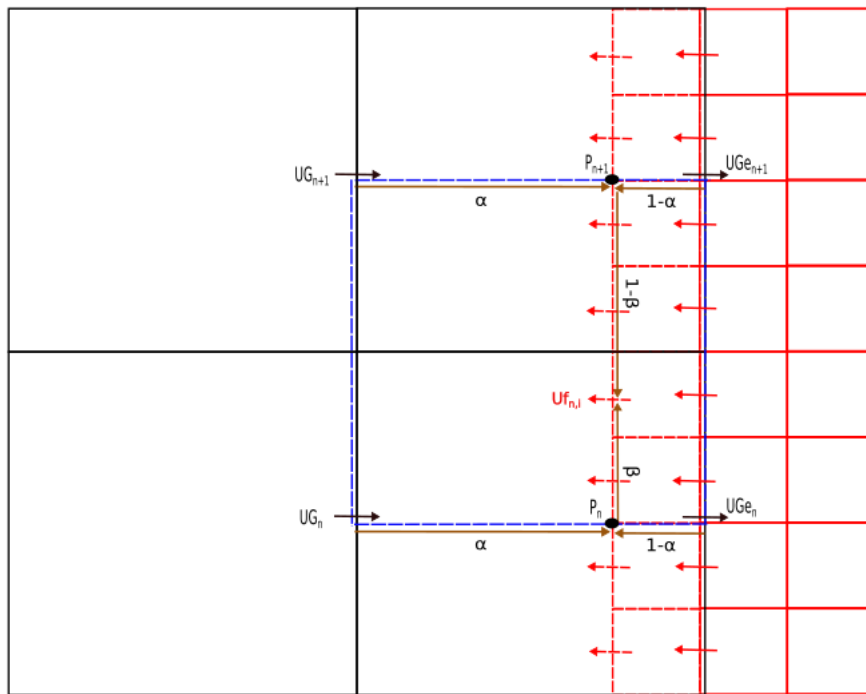


Figure 2-11: Prolongation for fictive surface-centred variables of fine domain

-General case

There are still some limits for model in previous case, since the mesh of the coarse domain must be a regular one, otherwise the flow is not conserved after interpolation. An improved method valid

for general cases is presented here, and we consider in the first step the staggered grids.

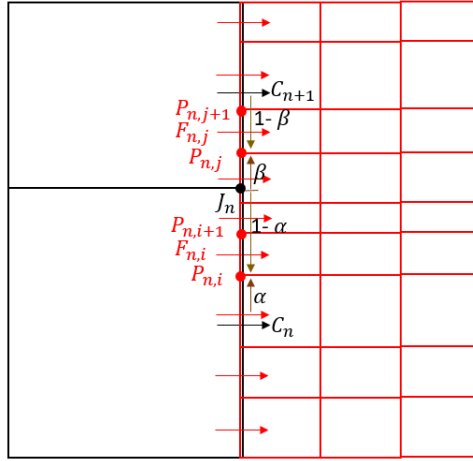


Figure 2-12: Interpolation for general case

Projection operator As depicted in Figure 2-12, the junction between two neighbouring coarse cell is named as J_n , we suppose that velocity field is linear in segment $C_n J_n$ and $J_n C_{n+1}$. The velocity value in the position J_n can be computed through flow conservation in the interval $C_n C_{n+1}$, as shown in Figure 2-13.

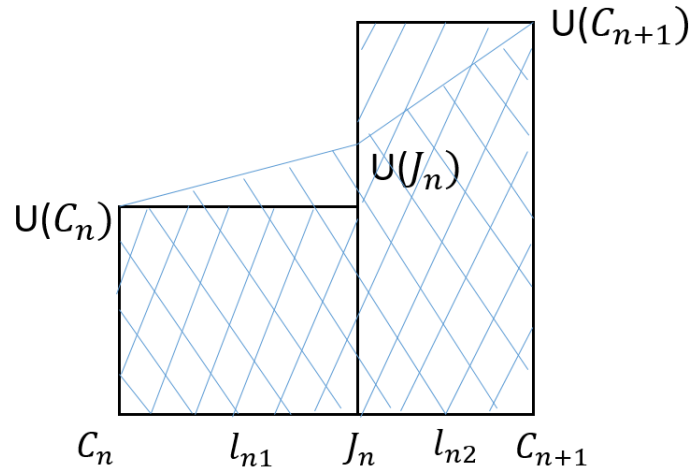


Figure 2-13: Calculation of junction value for general case

Mass flow rate passing $C_n C_{n+1}$ for the coarse domain :

$$\int_{C_n C_{n+1}} U(y) dy = U(C_n) l_{n1} + U(C_{n+1}) l_{n2} = Q C_n \quad (2.57)$$

Mass flow rate passing $C_n C_{n+1}$ after interpolation for fine domain :

$$\int_{C_n C_{n+1}} U(y) dy = \int_{C_n J_n} U(y) dy + \int_{J_n C_{n+1}} U(y) dy = QF_n \quad (2.58)$$

Besides,

$$QF_n = (U(C_n) + U(J_n)) \frac{l_{n1}}{2} + (U(J_n) + U(C_{n+1})) \frac{l_{n2}}{2} = QC_n \quad (2.59)$$

According to Eq.2.57 and 2.59, we have:

$$U(J_n) = \frac{U(C_n)l_{n1} + U(C_{n+1})l_{n2}}{l_{n1} + l_{n2}}$$

Which is also the mean value of mass flow rate in the interval $C_n C_{n+1}$. The interesting thing is that when $l_{n1} = l_{n2}$:

$$U(J_n) = \frac{U(C_n) + U(C_{n+1})}{2}$$

We can retrieve the expression in the previous case. In the interval $C_n J_n$, the vertex value of fine cell is calculated by:

$$U(P_{n,i}) = \alpha U(J_n) + (1 - \alpha) U(C_n)$$

With $\alpha = \frac{|C_n P_{n,i}|}{|C_n J_n|}$. The same way, in the interval $J_n C_{n+1}$, the expression of fine cell vertex value:

$$U(P_{n,j}) = \beta U(C_{n+1}) + (1 - \beta) U(J_n)$$

With $\beta = \frac{|J_n P_{n,j}|}{|J_n C_{n+1}|}$. At the top/bottom of the domain, the velocity field in each semi coarse segment is calculated through extrapolation of the neighbouring coarse segment.

$$U(P_{0,i}) = (U(C_1) - U(J_1)) \frac{|C_1 P_{0,i}|}{|C_1 J_1|} + U(C_1) \quad i = 1, \dots, N_0$$

$$U(P_{M,i}) = (U(C_M) - U(J_{M-1})) \frac{|C_M P_{M,i}|}{|C_M J_{M-1}|} + U(C_M) \quad i = 1, \dots, N_M$$

Finally,

$$U(F_{n,i}) = \frac{U(P_{n,i}) + U(P_{n,i+1})}{2}$$

$$U(F_{n,j}) = \frac{U(P_{n,j}) + U(P_{n,j+1})}{2}$$

Concerning the mass flow rate,

$$Q(F_{n,i}) = \int_{P_{n,i}P_{n,i+1}} U(y)dy = U(F_{n,i})|P_{n,i}P_{n,i+1}|$$

$$Q(F_{n,j}) = \int_{P_{n,j}P_{n,j+1}} U(y)dy = U(F_{n,j})|P_{n,j}P_{n,j+1}|$$

For the collocated grid, velocity is usually defined at the center of each cell, there is a space offset between positions where coarse cell values and fine cell values are extracted. In this case, the domain partially-overlapping method could be applied as shown in Figure 2-14. Then, the interpolation method used for staggered grid is still valid since the grid center of coarse boundary is coincide with the boundary edge of fine domain. We can follow the same way when fictive cells are defined, no more details are presented.

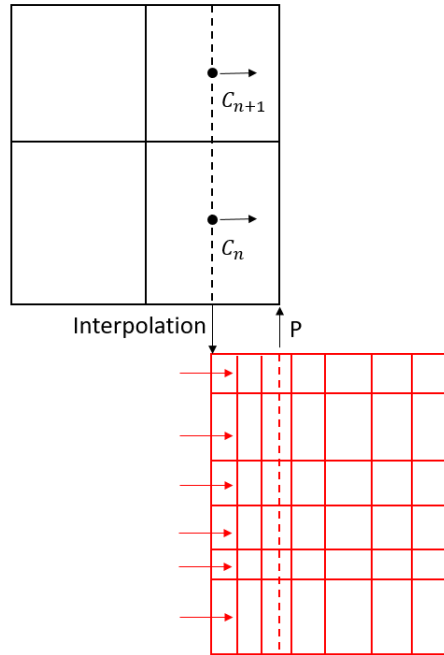


Figure 2-14: Interpolation with space partially overlapping for collocated grid

Methods presented above, such as domain decomposition methods and accelerant techniques, do not take into account the realistic boundary conditions available for each solver which is only applicable to one transferred variable. So practical numerical algorithms should be developed based on available boundary conditions to perform the coupling work. For the case with overlap, the MS method is chose since only Dirichlet transmission conditions are required; while for the case without overlap, a specific Dirichlet-Neumann method is used as cited previously. The fixed-point iteration is applied to develop explicit and implicit numerical schemes described in the following. As for data exchange methods, the previous surface average and linear interpolation approaches are applicable. Figure 2-15 shows a summary of the selected methods.

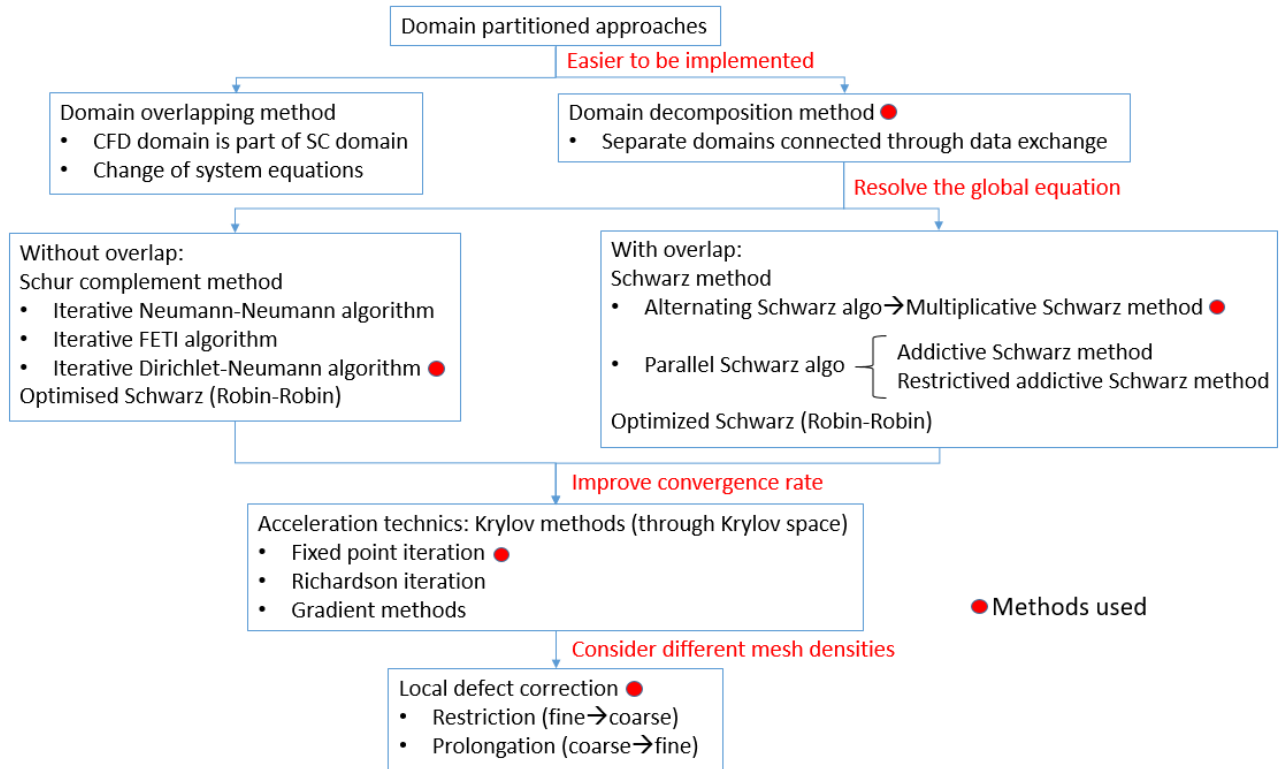


Figure 2-15: Outline of literature review

2.4 Numerical algorithms used in coupling work

2.4.1 Data exchange and time coupling

The selection of thermal-hydraulic variables exchanged at coupling interfaces is an important aspect, it has to guarantee the conservation of transported quantities, in particular mass, momentum and energy, between coupled codes [82]. Since only the isothermal single-phase case is considered hereafter and the flow is assumed to be incompressible, resulting in the uniform and constant value of density. According to input data required by each code, terms related to vapor phase and energy (such as temperature and enthalpy) could be ignored. Finally, velocity information (or mass flow rate) is transferred in one direction and pressure information in the opposite one. This data exchange option, shown in Figure 2-16, is conceived to be valid for the simulation of transients with inversions of the flow [34].

Data exchange is performed directly through memory using a dedicated data structure: MEDCoupling [83]. Its format was developed by EDF and CEA to face the challenges of data exchange between separate mediums. The goal was to design a standardized approach that could be used to exchange data between codes. The MEDCoupling data model has two components:

- Mesh: The mesh contains the domain geometry which is represented by a set of cells and nodes. The type can be hybrid, tetrahedron or hexahedron.

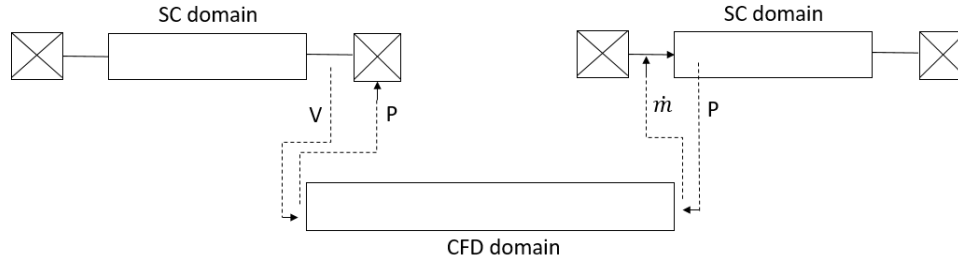


Figure 2-16: Data exchange at coupling interfaces for a single-phase open pipe flow

- Fields: They are results exchanged between codes, which can be stored on mesh cells or nodes.

Fields can be either intensive or extensive.

- Intensive data does not depend on the volume of the physical system, examples are: density, temperature or pressure.
- Extensive data is proportional to the volume of the physical system, examples are: mass flow, power or energy.

Another crucial aspect of the coupling technique is related to the time coupling and synchronization of the solvers, which refers to the choice of time step in each code and data exchange frequency. A straightforward way is to set an identical time step for both codes and exchange data at each time step. But since these two codes are designed to do simulations at different scales, it is quite normal that the time step of CFD solver is smaller than that of sub-channel code in order to optimize accuracy, computational costs and numerical stability. In the current coupling implementation, the advancement of the coupled codes with their internal time step is possible and data exchange is realized at the same time levels.

2.4.2 Problem formulation

Applying the domain decomposition technique, the computational domain consists of two (or more) separate sub-domains Ω_{CFD} and Ω_{SC} . As shown in Figure 2-17, the coupling is executed through data exchange of BCs at coupling interfaces, each of them characterized by a set of thermal-hydraulic field variables.

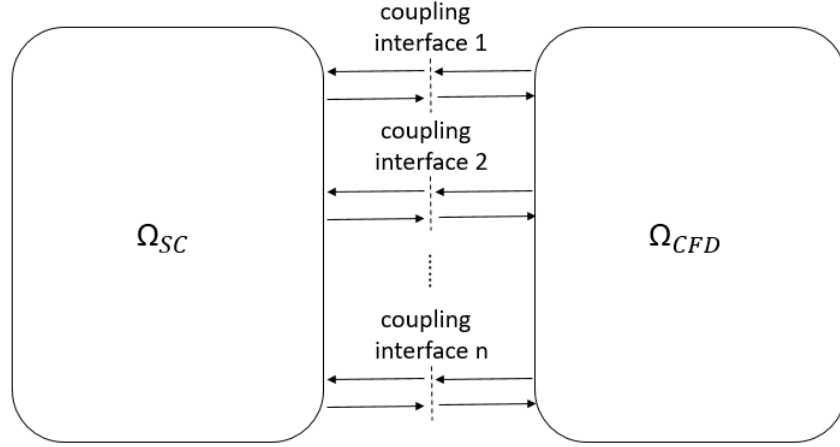


Figure 2-17: Conceptual scheme of a partitioned coupling method

In the following discussion, each coupled solver is considered as black-box [30], a unique input vector \mathbf{U}_{CFD} and \mathbf{U}_{SC} based on a set of thermal-hydraulic field variables exchanged at coupling interfaces is introduced for each solver. It results in the input-output relations:

$$\mathbf{Y}_{CFD} = \phi_{CFD}(\mathbf{U}_{CFD}) \quad (2.60)$$

$$\mathbf{Y}_{SC} = \phi_{SC}(\mathbf{U}_{SC}) \quad (2.61)$$

The operators ϕ_{CFD} and ϕ_{SC} are a synthesis of several operations in the solution process, and generally require additional internal boundary condition input data. As cited previously, the variables stored in the input and output vectors are data exchanged at coupling interfaces. Therefore, we have:

$$\mathbf{Y}_{CFD} = \mathbf{U}_{SC} \quad (2.62)$$

$$\mathbf{Y}_{SC} = \mathbf{U}_{CFD} \quad (2.63)$$

Based on Eqs. (2.60)-(2.63), the SC-CFD coupled problem can be expressed, in its fixed-point formulations, as follows:

$$\mathbf{U}_{CFD} = \phi_{SC}(\mathbf{U}_{SC}) = \phi_{SC}(\phi_{CFD}(\mathbf{U}_{CFD})) \quad (2.64)$$

For what concerns numerical aspects, two numerical schemes can be used, namely the explicit and implicit methods.

2.4.3 Explicit coupling scheme

In the explicit coupling scheme, the coupled solvers compute once every time step and data transfer only occurs at the end of each time step. As presented in Figure 2-18, a sequential communication

pattern has been applied.

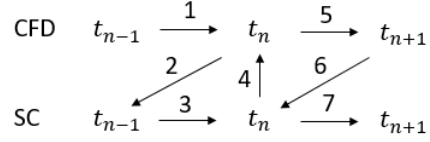


Figure 2-18: Sequential communication pattern implemented in the explicit coupling scheme

The pattern implies that CFD solver advances firstly its time step using boundary conditions given by sub-channel code in the previous time step, the computed updated boundary conditions are then sent to SC code to advance to the same time level. This coupling method can be expressed by the following equations, showing how the input vector for the n^{th} time step can be evaluated through a single coupling iteration.

$${}^n \mathbf{Y}_{CFD} = \phi_{CFD}({}^n \mathbf{U}_{CFD} = {}^{n-1} \mathbf{Y}_{SC}) \quad (2.65)$$

$${}^{n+1} \mathbf{U}_{CFD} = {}^n \mathbf{Y}_{SC} = \phi_{SC}({}^n \mathbf{U}_{SC} = {}^n \mathbf{Y}_{CFD}) = \phi_{SC}(\phi_{CFD}({}^n \mathbf{U}_{CFD})) \quad (2.66)$$

The flowchart of the related numerical scheme is schematically represented in Figure 2-19. In this way, the equation Eq.2.64 is generally not solved at each coupling iteration, resulting in the pressure-velocity imbalance at the coupling interfaces. Especially for the simulations of fast transients, incompressible flow [84], it can lead to numerical stability issues. Consequently, time steps should be strictly restricted during the computation.

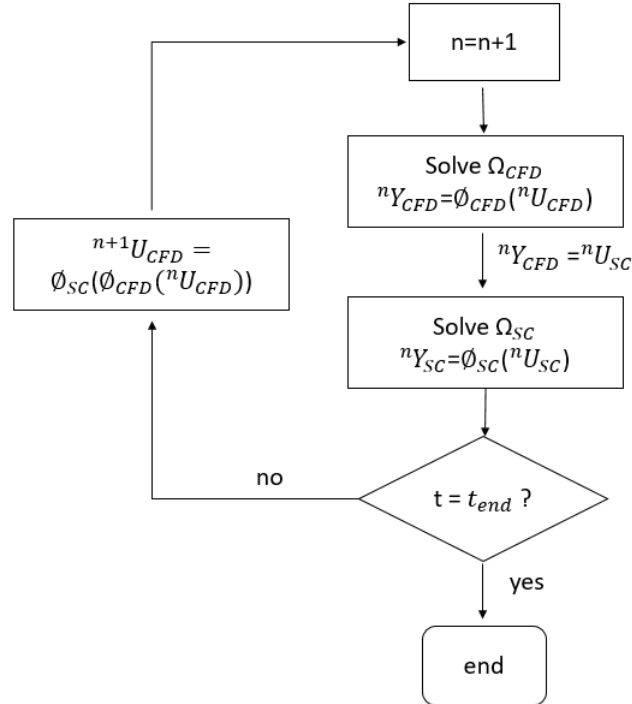


Figure 2-19: Flowchart of the generic sequential explicit coupling numerical algorithm

2.4.4 Implicit coupling scheme

In order to enforce the pressure-velocity equilibrium at the coupling interfaces, an implicit scheme [85, 86] is applied to obtain approximate solutions of Eq.2.64 through several sub-iterations within each time step until the defined convergence criterion is met, it is named as semi-implicit coupling methodology or fixed-point iteration [87]. In this way, global conservation of transported quantities can be assured, leading to improved accuracy and numerical stability. Using the sequential communication pattern introduced previously, the Gauss-Seidel fixed-point iteration scheme can be expressed as:

$${}^n \mathbf{Y}_{CFD}^k = \phi_{CFD}({}^n \mathbf{U}_{CFD}^k = {}^n \mathbf{Y}_{SC}^{k-1}) \quad (2.67)$$

$${}^n \mathbf{U}_{CFD}^{k+1} = {}^n \mathbf{Y}_{SC}^k = \phi_{SC}({}^n \mathbf{U}_{SC}^k = {}^n \mathbf{Y}_{CFD}^k) = \phi_{SC}(\phi_{CFD}({}^n \mathbf{U}_{CFD}^k)) \quad (2.68)$$

where k refers to k^{th} iteration of the n^{th} time step. Concerning the convergence criterion for coupling iteration, the residual vector is defined as:

$${}^n \mathbf{R}^k = {}^n \mathbf{Y}_{SC}^k - {}^n \mathbf{U}_{CFD}^k \quad (2.69)$$

Only when all components of the residual vector (pressure and velocity) satisfy the corresponding residual criterion, can the time step pass to the next one. Figure 2-20 represents the schematic flowchart of the implicit coupling algorithm.

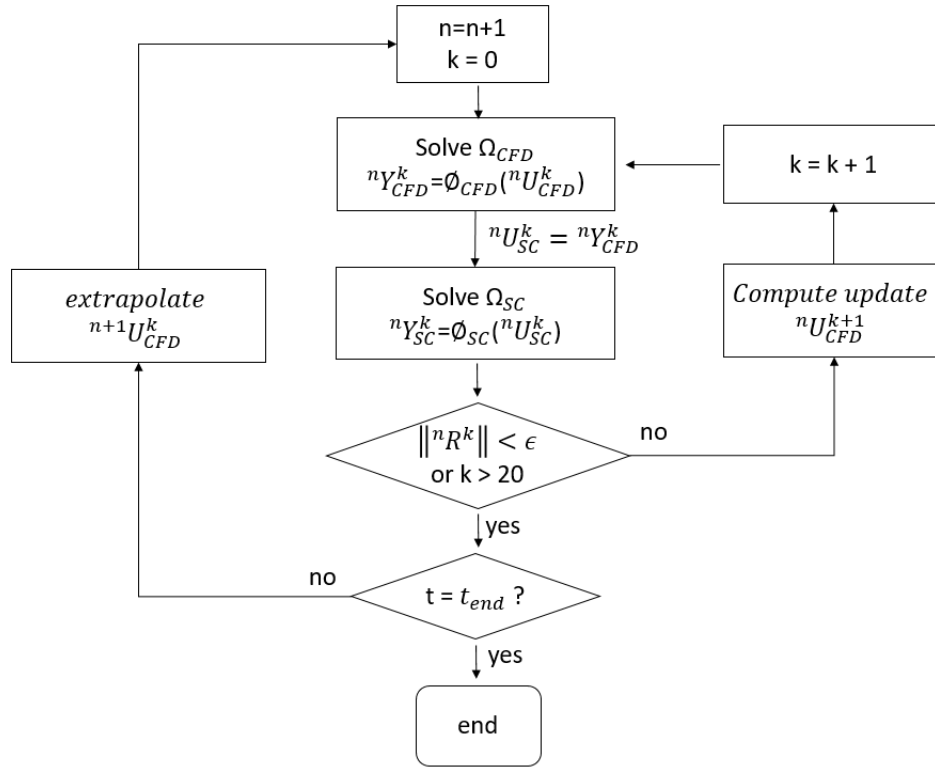


Figure 2-20: Flowchart of the implicit coupling numerical algorithm

2.4.5 General implicit coupling scheme

The implicit coupling scheme proposed by A.Toti et al. [30] is only valid for the case where time steps of two solvers are the same, while in the current coupled work, time step of SC solver is much larger than that of CFD solver. It is significant to propose an implicit numerical algorithm with different time steps for each solver, which can improve greatly the computation efficiency, as shown in Figure 2-21.

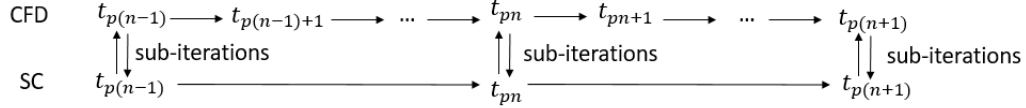


Figure 2-21: General sequential communication pattern implemented in the implicit coupling scheme

We suppose that time step of SC solver is an integral multiple of that of CFD solver. The sub-iterations will be performed at each time level of SC code, as depicted in Figure 2-22. After each sub-iterations, SC solver will wait for CFD solver until the same time level is reached. During this period, CFD code simply launches the stand-alone calculations.

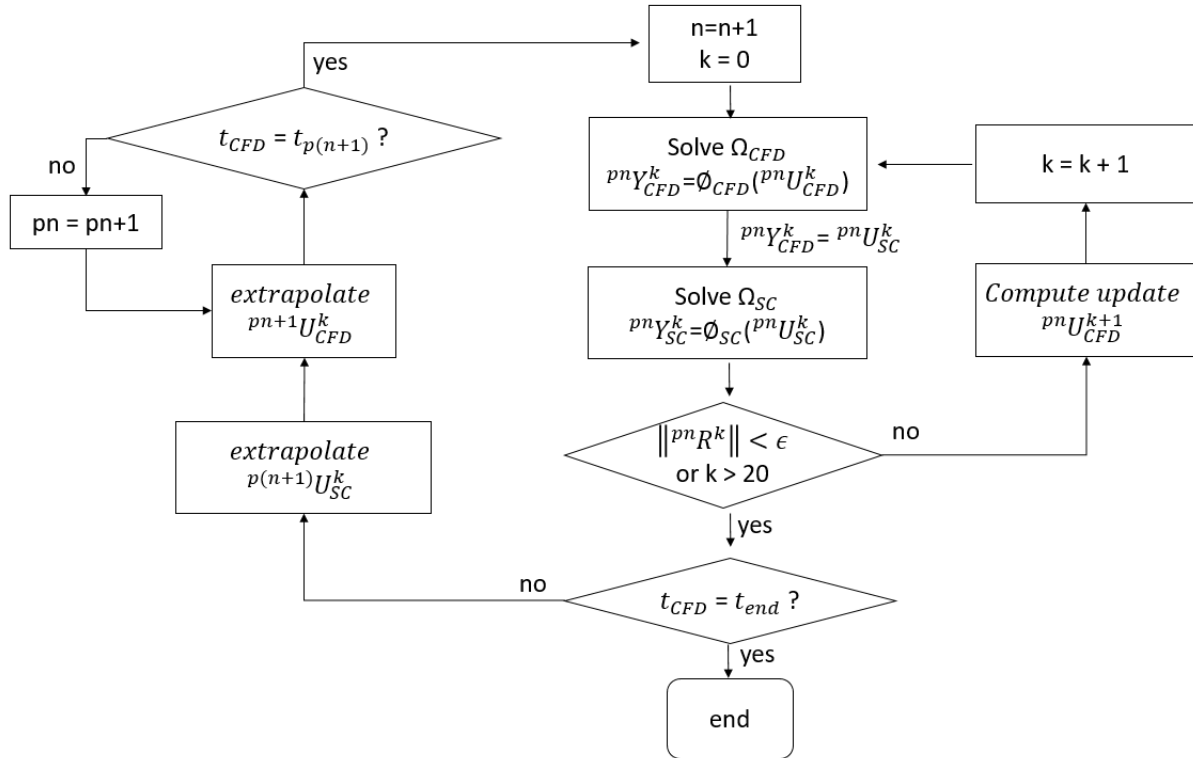


Figure 2-22: Flowchart of general implicit coupling numerical algorithm

2.5 Conclusions

For domain decomposition methods, computational domains of two solvers can be overlapping or not. The used methods are Schwarz alternating and Schur complement, respectively, in current work. The case with overlapping subdomains can converge with all-Dirichlet transmission conditions. In contrast, for non-intersecting subdomains, Robin-Robin, Neumann-Neumann transmission conditions, etc., are required to obtain convergent solutions. Based on types of boundary conditions defined on two sides of interface, Gander et al. [44] proposed the Neumann-Dirichlet method to satisfy the equilibrium equation while only Dirichlet or Neumann method is used for respectively velocity or pressure in our work.

Field variables exchanged are mass flow rate in one direction and the pressure information in the opposite one. Explicit and implicit numerical schemes are developed among which the difference is whether there is sub-iterations within each time step. Residuals of transported quantities are defined to measure the solution convergence. Implicit algorithm allows us to use larger time step and so is more flexible.

To treat the case with different mesh refinements, multigrid data exchange method is developed which consists of restriction and prolongation procedures. Surface or volume average is required during the restriction process while linear interpolation method is applied to construct continuous velocity profile when passing data from coarse domain to fine domain.

Chapter 3

Complex problem of coupling different two-phase flow models

The methods used to perform the coupling between codes were explained in the previous chapter. In this chapter, we will focus on the complex problem of coupling two different two-phase flow models such as the 6 equations model and the porous 4 equations model. The proposed research is only practically implemented for single phase flows in the next chapters for demonstration purposes. Considering the general case of two-phase flow is however mandatory for the perspectives and outcomes of the introduced approach.

3.1 Phasic variables

The time averaged balance equations of a two-fluid model [88] are the macroscopic balance equation and the interfacial transfer conditions derived from the time averaging are applied to the conservation laws of mass, momentum and energy.

Firstly, variables of each phase are considered: $\alpha_k, \rho_k, \mathbf{u}_k = (u_{kz}, u_{kx}, u_{ky})^T, \rho_k E_k$ and $\rho_k H_k$ as the fraction, the density, the velocity vector (with spatial components in z, x and y), the total energy and the total enthalpy of the phase $k = l, v$ (l:liquid, v:vapor). The phases' fractions, or volume rate, are linked by the relation as follow:

$$\alpha_v + \alpha_l = 1 \quad (3.1)$$

Noting the operator $\nabla = (\partial_z, \partial_x, \partial_y)^T$ and $(\nabla \cdot)$ the divergence operator. Considering the conservation equations for each phase, the conservation of mass is expressed in a differential form by:

$$\frac{\partial \alpha_k \rho_k}{\partial t} + \nabla(\alpha_k \rho_k \mathbf{u}_k) = \Gamma_k \quad (3.2)$$

with Γ_k the interfacial mass source due to phase changes, and :

$$\sum_k \Gamma_k = 0 \quad (3.3)$$

which expresses the conservation of mass at the interfaces. The macroscopic momentum balance is expressed by:

$$\frac{\partial \alpha_k \rho_k u_k}{\partial t} + \nabla(\rho_k u_k \otimes u_k) = -\nabla \alpha_k p_k + \nabla \alpha_k (\sigma_k + \sigma_k^T) + \alpha_k \rho_k g_k + M_k \quad (3.4)$$

with σ_k^T and M_k the turbulent flux and the momentum source from the interfacial transfer, and:

$$\sum_k M_k = 0 \quad (3.5)$$

which expresses the conservation of momentum at the interface with the assumption of a mixture momentum source due to the surface tension effect negligible. The energy balances for the macroscopic fields is expressed by:

$$\frac{\partial \alpha_k \rho_k (e_k + u_k^2/2)}{\partial t} + \nabla(\alpha_k \rho_k (e_k + u_k^2/2) u_k) = -\nabla(\alpha_k (q_k + q_k^T)) + \nabla(\alpha_k (\sigma_k - p_k) u_k) + \alpha_k \rho_k g_k u_k + E_k \quad (3.6)$$

and

$$\sum_k E_k - E_m = 0 \quad (3.7)$$

with e_k the internal energy and E_k represents the interfacial supply of energy and E_m is the energy source for the mixture. The turbulent heat flux q_k^T takes account for the turbulent energy convection as well as for the turbulent work.

The interfacial transfer conditions for mass, momentum and energy couple the transport processes of each phase. These equations express the conservation laws and it should be necessary to add constitutive equations that specify molecular diffusions, turbulent transports and interfacial transfer mechanisms as a relation between the thermodynamic state variables.

3.2 Mixture variables

The basic concept of the mixture model is to consider the mixture and then the mixture mass, momentum and energy in terms of the mixture properties with a diffusion equation that takes account for the concentration changes. The mixture mass equation is expressed by:

$$\frac{\partial \rho}{\partial t} + \nabla(\rho u) = 0 \quad (3.8)$$

with $\rho = \sum_k \alpha_k \rho_k$ the mixture density, and $u = \frac{\sum_k \alpha_k \rho_k u_k}{\rho}$ the mixture center of mass velocity. The diffusion equation which expresses the changed in concentration α_1 is given by:

$$\frac{\partial \alpha_1 \rho_1}{\partial t} + \nabla(\alpha_1 \rho_1 u) = \Gamma_1 - \nabla(\alpha_1 \rho_1 u_{r1}) \quad (3.9)$$

with u_{r1} the diffusion velocity of phase 1, namely the relative velocity with respect to the mass center of the mixture defined by :

$$u_{r1} = u_k - u = -c_2 u_r$$

expresses by the relative velocity u_r . Apart from the local fraction α_k a concentration based on mass can be defined (analogy with the theory of diffusion) and is given by:

$$c_k = \frac{\alpha_k \rho_k}{\rho} \quad (3.10)$$

and

$$\sum_k c_k = 1 \quad (3.11)$$

Considering the phase concentration, the mass vapor equation can be expressed by:

$$\frac{\partial \rho c_k}{\partial t} + \nabla(\rho c_k u) = \Gamma_k - \nabla(\rho c_k (1 - c_k) u_r) \quad (3.12)$$

The mixture momentum equation is expressed by:

$$\frac{\partial \rho u}{\partial t} + \nabla(\rho u \otimes u) = -\nabla p + \nabla(\sigma + \sigma^T + \sigma^D) + \rho g + M \quad (3.13)$$

with $p = \sum_k \alpha_k p_k$ the mixture pressure, $\sigma = \sum_k \alpha_k \sigma_k$ the average viscous stress, σ^T the turbulent stress and σ^D the diffusion stress. The average body force is defined by $g = \sum_k \alpha_k \rho_k g_k / \rho$ and M is the interfacial momentum source. The mixture energy equation is given by:

$$\frac{\partial \rho(e + u^2/2)}{\partial t} + \nabla(\rho(e + u^2/2)u) = -\nabla(q + q^T + q^D) + \nabla(\sigma \cdot u) - \nabla(pu) + \rho g \cdot u + E_m \quad (3.14)$$

with $q = \sum_k \alpha_k q_k$, $e = \frac{\sum_k \alpha_k \rho_k e_k}{\rho}$ the mixture energy. E_m is the interfacial energy source, q^T is the turbulent flux and q^D is the diffusion flux.

3.3 Porous 4 equations model : FLICA4

FLICA4 is a three-dimensional two-phase flow computational code dedicated to reactor core analysis (permanent and transient regimes). The code is based on the two-phase drift-flux model that

has been widely used for the analysis of thermal-hydraulic transients. Thus, the system of balance equation is a four-equation system which is a mixture mass, a steam phasic mass, a mixture momentum and a mixture energy. The drift-flux model is used to account for the slip between steam and water phases at the same pressure.

The model of FLICA4 is mainly derived by summing the evaluation of each phase. The detail of this calculation is not presented here, a similar model compared with FLICA4 is provided formally from a two-fluid with two-pressures model [89]. From the physical quantities of each phase, variables of the mixture involved in the description of model with 4 equations of FLICA4 can be expressed as:

- The mixture density $\rho = \alpha_v \rho_v + \alpha_l \rho_l$.
- Vapor mass concentration $c = \alpha_v \rho_v / \rho$. Using the definition of averaged density, we can deduct that $1 - c = \alpha_l \rho_l / \rho$.
- The mixture velocity $\mathbf{u} = (\alpha_v \rho_v \mathbf{u}_v + \alpha_l \rho_l \mathbf{u}_l) / \rho$. In the following, the velocity vector of mixture with its three spatial components are taken into account:

$$\mathbf{u} = (u_z, u_x, u_y)^T.$$

- The mixture kinetic energy $\varepsilon = \frac{1}{2}(\alpha_v \rho_v |\mathbf{u}_v|^2 + \alpha_l \rho_l |\mathbf{u}_l|^2) / \rho$ where $|\cdot|$ is the Euclidean norm.
- The mixture internal energy $e = (\alpha_v \rho_v e_v + \alpha_l \rho_l e_l) / \rho$.
- The mixture total energy $E = (\alpha_v \rho_v E_v + \alpha_l \rho_l E_l) / \rho$.
- The mixture total enthalpy $H = (\alpha_v \rho_v H_v + \alpha_l \rho_l H_l) / \rho$.
- The mixture specific enthalpy $h = (\alpha_v \rho_v h_v + \alpha_l \rho_l h_l) / \rho$.

The relative velocity between the two phases, is defined by the relation:

$$\mathbf{u}_r = \mathbf{u}_v - \mathbf{u}_l$$

Then, the phasic velocity \mathbf{u}_k can be expressed in function of mixture velocity \mathbf{u} and relative velocity \mathbf{u}_r between phases:

$$\mathbf{u}_v = \mathbf{u} + (1 - c)\mathbf{u}_r$$

$$\mathbf{u}_l = \mathbf{u} - c\mathbf{u}_r$$

These two velocities, as well as the previous definitions, lead to the expression of mixture kinetic energy ε as the equivalence of kinetic energy of mixture in which the contribution of the relative standard velocity is added:

$$\varepsilon = \frac{|\mathbf{u}|^2}{2} + c(1 - c)\frac{|\mathbf{u}_r|^2}{2} \quad (3.15)$$

Taking back this equality on kinetic energy, we can define mixture total energy and mixture enthalpy with classic equalities:

$$E = e + \varepsilon, H = h + \varepsilon$$

Otherwise, the specific enthalpy and internal energy are linked by the relation:

$$h = e + \frac{p}{\rho},$$

where p is the mixture pressure. The phases are considered as in mechanical balance. The law of pressure p for the two-phase mixture depends classically on density ρ and internal total energy ρe but also on state of two-phase mixture determined by the vapor mass ρc . Besides, a general expression of pressure law is:

$$p = p(\rho, \rho c, \rho e). \quad (3.16)$$

$$\chi = \left(\frac{\partial p}{\partial \rho}\right)_{\rho c, \rho e}, \xi = \left(\frac{\partial p}{\partial \rho c}\right)_{\rho, \rho e}, \kappa = \left(\frac{\partial p}{\partial \rho e}\right)_{\rho, \rho c} \quad (3.17)$$

$$dp = \chi d\rho + \xi d(\rho c) + \kappa d(\rho e). \quad (3.18)$$

$$a^2 = \kappa h + \chi + c\xi, \quad (3.19)$$

$$a^2 > 0.$$

The system of equations of mixture model can be written in the general case with a certain porosity ϕ and for $t > 0, \mathbf{x} = (z, x, y)^T \in R^3$. The conservative form of the system [90] of equations is:

$$\left\{ \begin{array}{l} \phi \frac{\partial}{\partial t} \rho + \nabla(\phi \rho \mathbf{u}) = 0 \\ \phi \frac{\partial}{\partial t} (\rho c) + \nabla(\phi \rho c \mathbf{u}) + \nabla(\phi \rho c (1 - c) \mathbf{u}_r) - \nabla(\phi K_{cv} \nabla C) = \phi \Gamma_v \\ \phi \frac{\partial}{\partial t} (\rho \mathbf{u}) + \nabla(\phi \rho \mathbf{u} \otimes \mathbf{u} + \phi p I) + \nabla(\phi \rho c (1 - c) \mathbf{u}_r \otimes \mathbf{u}_r) - \nabla(\sigma) = p \nabla \phi + \phi \tau + \phi \rho \mathbf{g} \\ \phi \frac{\partial}{\partial t} (\rho E) + \nabla(\phi \rho H \mathbf{u}) + \nabla(\phi \rho c (1 - c) (H_v - H_l) \mathbf{u}_r) - \nabla(\mathbf{q}) = \phi Q + \phi \rho \mathbf{g} \cdot \mathbf{u} \end{array} \right. \quad (3.20)$$

with :

K_{cv} the concentration dispersion coefficient from the numerical turbulent fluxes at the interfaces of the phasic mass balance;

\mathbf{u}_r the relative velocity;

Γ_v the interphase mass exchange;

Q the power density;

τ the friction forces;

q the heat flux;

The first equation explain the evolution of total mass of the mixture. The second equation correspond to vapor mass balance. The third is the equation of momentum evolution of the mixture. The last equation correspond to the energy balance.

3.4 Six equations model : NEPTUNE_CFD

NEPTUNE_CFD is a system designed to solve the Navier-Stokes equations in the cases of 2D, 2D axisymmetric or 3D multiphase flows. It deals with free surface flow, droplet-laden flow, bubbly or boiling flow and particle-laden flow. It can simulate flows which may be steady or unsteady, laminar or turbulent, incompressible or compressible, isothermal or not. NEPTUNE_CFD relies on a finite volume discretisation and allows the use of various mesh types which may be hybrid (containing several kinds of elements) and may have structural non-conformities (hanging nodes).

In the following, the mass, momentum and energy balance equations for two-phase flows used in NEPTUNE are presented [91].

3.4.1 Mass balance equations

The two-phase mass balance equation for the phase k is written as

$$\frac{\partial}{\partial t}(\alpha_k \rho_k) + \frac{\partial}{\partial x_i}(\alpha_k \rho_k U_{k,i}) = \Gamma_k \quad (3.21)$$

with α_k, ρ_k, U_k the volume fraction, the density and the mean velocity of phase k, respectively. Γ_k is the interface mass transfer rate on phase k

$$\Gamma_k = \sum_{p \neq k} \Gamma_{(p \rightarrow k)}^c + \Gamma_{(w \rightarrow k)}^{nuc} \quad (3.22)$$

$\Gamma_{p \rightarrow k}^c$ is the interface mass transfer from phase p to phase k. $\Gamma_{(w \rightarrow k)}^{nuc}$ represents the mass transfer contribution to phase k induced by wall nucleate boiling. In our model, only terms near heated wall are considered which verify

$$\Gamma_{(w \rightarrow 1)}^{nuc} + \Gamma_{(w \rightarrow 2)}^{nuc} = 0 \quad (3.23)$$

and

$$\Gamma_{(w \rightarrow 2)}^{nuc} \geq 0 \quad (3.24)$$

since steam is produced by nucleation, conservation relations for mass and volume lead to

$$\sum_k \alpha_k = 1, \quad (3.25)$$

$$\sum_k \Gamma_k = 0 \quad (3.26)$$

3.4.2 Momentum equations

The two-phase momentum balance equation for the phase k is firstly presented in its semi-conservative form (all the contributions are conservative except for the pressure gradient one)

$$\frac{\partial}{\partial t}(\alpha_k \rho_k U_{k,i}) + \frac{\partial}{\partial x_j}(\alpha_k \rho_k U_{k,i} U_{k,j}) = \frac{\partial}{\partial x_j}(\alpha_k \tau_{k,ij} + \sum_{k,ij}^{Re}) - \alpha_k \frac{\partial P}{\partial x_i} + \alpha_k \rho_k g_i + \sum_{p \neq k} I_{(p \rightarrow k)} + \alpha_k S_k \quad (3.27)$$

with P the mean pressure and g_i acceleration due to gravity. The viscous stress tensor is defined by

$$\tau_{k,ij} = \mu_k \left(\frac{\partial U_i}{\partial x_j} + \frac{\partial U_j}{\partial x_i} - \frac{2}{3} \text{div}(U) \delta_{ij} \right). \quad (3.28)$$

where μ_k is the dynamic viscosity. $\sum_{k,ij}^{Re} = -\alpha_k \rho_k \langle U'_{k,i} U'_{k,j} \rangle_k$ is the turbulent stress tensor. $S_k = S_k(\alpha_l, U_l, P)$ with $l = 1, \dots$ number of phases, is the external source terms such as head losses for instance. $I_{(p \rightarrow k)} = (I'_{(p \rightarrow k),i} + \Gamma_k U_{pk,i}^I)$ represents the average interface momentum transfer rate from phase p to phase k. $I'_{p \rightarrow k}$ is the part of the interface momentum transfer rate that remains after substitution of the mass transfer contribution.

The non-conservative form is obtained after decomposition of the non stationary term with respect to the mass balance equation, and dividing by the volume fraction.

$$\begin{aligned} \rho_k \frac{\partial}{\partial t} U_{k,i} - U_{k,i} \frac{1}{\alpha_k} \frac{\partial}{\partial x_j}(\alpha_k \rho_k U_{k,j}) + \frac{1}{\alpha_k} \frac{\partial}{\partial x_j}(\alpha_k \rho_k U_{k,i} U_{k,j}) = \\ \frac{1}{\alpha_k} \frac{\partial}{\partial x_j}(\alpha_k \tau_{k,ij} + \sum_{k,ij}^{Re}) - \frac{\partial P}{\partial x_i} + \rho_k g_i + \sum_{p \neq k} (J'_{(p \rightarrow k),i}) + S_{k,i} \end{aligned} \quad (3.29)$$

with

$$J'_{(p \rightarrow k),i} = \frac{I'_{(p \rightarrow k),i}}{\alpha_k}. \quad (3.30)$$

3.4.3 Energy equations

The total enthalpy is defined by

$$H_k = e_k + \frac{1}{2}u_k^2 + \frac{P}{\rho_k} \quad (3.31)$$

The energy equation in conservative form is written

$$\begin{aligned} \frac{\partial \alpha_k \rho_k H_k}{\partial t} + \frac{\partial}{\partial x_j} (\alpha_k \rho_k H_k U_{k,j}) = \\ \frac{\partial}{\partial x_j} (\alpha_k U_{k,i} \tau_{k,ij}) - \frac{\partial}{\partial x_j} (\alpha_k Q_{k,j}) + \alpha_k \frac{\partial P}{\partial t} + \alpha_k \rho_k U_{k,i} g_i + \Pi_k + \varphi_{wall \rightarrow k} + \sum_{p \neq k} I'_{(p \rightarrow k),i} U_{k,i} \end{aligned} \quad (3.32)$$

with $Q_k = -\lambda_k T_k$ and λ_k the thermal conductivity. $\varphi_{wall \rightarrow k}$ represents the heat exchanges with boundaries and is described by the nucleate boiling model. Π_k is the bulk interface heat transfer, sum of the interface transfer between phase p and phase k, which complies with conservation relation

$$\Pi_k = \sum_{p \neq k} \Pi_{p \rightarrow k} \quad (3.33)$$

The interface heat transfer between two phases are divided into two contributions, one related to mass transfer term, the second independent of the mass transfer

$$\Pi_{p \rightarrow k} = \Gamma_{p \rightarrow k}^c H_{p \rightarrow k}^\sigma + \Pi'_{p \rightarrow k} \quad (3.34)$$

In order to verify the conservation relation, two choices are possible for the jump of enthalpy for the two phases: it may be the same or independent. If it's the same, we have $H_{p \rightarrow k}^\sigma = H_{k \rightarrow p}^\sigma = H^\sigma$ so that the relation $\Pi'_{p \rightarrow k} + \Pi'_{k \rightarrow p} = 0$ is easily to be verified. If the jump of enthalpy are independent, then the following relation must be verified

$$\Gamma_{p \rightarrow k}^c = -\frac{\Pi'_{p \rightarrow k} + \Pi'_{k \rightarrow p}}{H_{p \rightarrow k}^\sigma - H_{k \rightarrow p}^\sigma} \quad (3.35)$$

Note that in our case of two-phase flows, the last model is written as

$$H_{2 \rightarrow 1}^\sigma = H_1, H_{1 \rightarrow 2}^\sigma = H_2 \quad (3.36)$$

and introducing independent models for heat transfers, for each phase we have

$$\Pi'_{2 \rightarrow 1} = \Pi_1'^{w/s}, \Pi'_{1 \rightarrow 2} = \Pi_2'^{w/s} \quad (3.37)$$

so we have the condensation rate

$$\Gamma_1^c = \frac{\Pi_1'^{w/s} + \Pi_2'^{w/s}}{H_2 - H_1} \quad (3.38)$$

The non-conservative form is obtained after decomposition of the unsteady term with respect to the mass balance equation, and after division by the volume fraction

$$\begin{aligned} & \rho_k \frac{\partial}{\partial t} H_k - H_k \frac{1}{\alpha_k} \frac{\partial}{\partial x_j} (\alpha_k \rho_k U_{k,j}) + \frac{1}{\alpha_k} \frac{\partial}{\partial x_j} (\alpha_k \rho_k H_k U_{k,j}) = \\ & - \frac{1}{\alpha_k} \frac{\partial}{\partial x_j} (\alpha_k Q_{k,j}) + \frac{\partial P}{\partial t} + \rho_k U_{k,i} g_i + \frac{\varphi_{wall \rightarrow k}}{\alpha_k} + \frac{1}{\alpha_k} \sum_{p \neq k} [\Pi'_{(p \rightarrow k)} + \Gamma_{(p \rightarrow k)}^c H_{(p \rightarrow k)}^\sigma] - \frac{\Gamma_k H_k}{\alpha_k} \end{aligned} \quad (3.39)$$

Notice that in the standard case where $H_{(p \rightarrow k)}^\sigma$ is taken equal to H_k , and where nucleate transfer does not exist ($\sum \Gamma_{p \rightarrow k}^c = \Gamma_k$), the mass transfer terms do not appear in the equation.

3.5 Coupling of two-phase flow models

Various two-phase flow models are used by the nuclear community, among which we should at least mention the standard six-equation two-fluid model (noted STFMM afterwards) and four-equation homogeneous relaxation model (noted HRM in the following) [92]. The interfacial coupling of hyperbolic systems of conservation laws has emerged recently which basically focus on the interfacial state coupling [93] or alternatively on the flux coupling techniques. Roughly speaking, the former favours the continuity of the conservation variable, whereas the latter aims at ensuring the intrinsic conservation laws [94].

3.5.1 Left STFMM model

The code on the left hand side of "coupling interface" is assumed to use the classical two-fluid model (where $k=1,v$), whose derivation may be found in [95]:

$$\begin{cases} \partial_t(m_k) + \partial_x(m_k U_k) = 0; \\ \partial_t(m_k U_k) + \partial_x(m_k U_k^2) + \alpha_k \partial_x(P) = I_k(W); \\ \partial_t(\alpha_k E_k) + \partial_x(\alpha_k U_k (E_k + P)) + P_I^* \partial_t(\alpha_k) = V_I^* I_k(W) \end{cases}$$

where the state variable is: $W_{STFMM}^t = (m_1, m_2, m_1 U_1, m_2 U_2, \alpha_1 E_1, \alpha_2 E_2)$. The equilibrium pressure P is the same for both phases. A closure law for the interfacial momentum transfer term I_k , which takes drag effects into account, must be given:

$$I_k = (-1)^k \frac{m_1 m_2}{\tau_U (m_1 + m_2)} (U_1 - U_2)$$

where τ_U is the velocity relaxation time. We consider here the rough closure: $P_I^* = P$ and the interface velocity V_I^* is usually taken as the velocity of the dilute phase.

3.5.2 Right HRM model

On the right hand side, the second code uses an homogeneous two-phase flow model whose derivation is straightforward when starting from the two-fluid approach [95]:

$$\begin{cases} \partial_t(\rho) + \partial_x(\rho U) = 0 \\ \partial_t(\rho C) + \partial_x(\rho UC) = 0 \\ \partial_t(\rho U) + \partial_x(\rho U^2) + \partial_x(P) = 0 \\ \partial_t(E) + \partial_x(U(E + P)) = 0 \end{cases}$$

where field variables are quantities of mixture. We assume a vanishing relative velocity $U_r = U_2 - U_1 = 0$, and the state variable is $W_{HRM}^t = (\rho, \rho C, \rho U, E)$.

3.5.3 Father model

The father model enables us to retrieve the left STFM model by enforcing a pressure equilibrium, while it also leads to the right HRM model by imposing a pressure-velocity-temperature equilibrium. The state variable of the coupling model is: $W^t = (\alpha_1, m_1, m_2, m_1 U_1, m_2 U_2, \alpha_1 E_1, \alpha_2 E_2)$. We will thus focus on the following two-fluid model (see [96]):

$$\begin{cases} \partial_t(\alpha_1) + V_I \partial_x(\alpha_1) = \phi_1(W) \\ \partial_t(m_k) + \partial_x(m_k U_k) = 0 \\ \partial_t(m_k U_k) + \partial_x(m_k U_k^2) + \alpha_k \partial_x(P_k) + (P_k - P_I) \partial_x(\alpha_k) = I_k(W) \\ \partial_t(\alpha_k E_k) + \partial_x(\alpha_k U_k (E_k + P_k)) + P_I \partial_t(\alpha_k) = V_I I_k(W) \end{cases} \quad (3.40)$$

A closure law for the source term must be added: $\phi_k = (-1)^k \alpha_1 \alpha_2 (P_2 - P_1) / \tau_P \Pi_0$, where τ_P stands for the pressure relaxation time and Π_0 refers to some pressure constant given by user. In practice, nuclear applications in PWR obviously leads to the choice $(V_I, P_I) = (U_1, P_2)$, where the index 1 refers to the dilute phase. In the following, we note $Z = (\alpha_1, \rho_1, U_1, P_1, \rho_2, U_2, P_2)$. By introducing the entropy $\eta = m_1 s_1 + m_2 s_2$ and the entropy flux $f_\eta = m_1 U_1 s_1 + m_2 U_2 s_2$, the physical entropy inequality of the coupling model is satisfied [92]:

$$\partial_t(\eta) + \nabla \cdot (f_\eta) \geq 0$$

3.5.4 Main ideas of the coupling algorithm

Boundary conditions are imposed on each side of the coupling interface that separates the STFM and the HRM finite volume codes, by solving the 1D Riemann problem associated with the LHS of Eqs.(3.40) together with initial conditions Z_L, Z_R as defined below.

Defining initial conditions

Starting from the STFM-cell value on the LHS of the interface:

$$Z_{STFM}^- = (\alpha_1^-, \rho_1^-, U_1^-, \rho_2^-, U_2^-, P^-)$$

We define Z_L on the left side of the coupling interface:

$$Z_L = (\alpha_1^-, \rho_1^-, U_1^-, P_1^- = P^-, \rho_2^-, U_2^-, P_2^- = P^-)$$

Starting from the HRM-cell value on the RHS of the interface:

$$Z_{HRM}^+ = (\rho^+, \rho^+ C^+, \rho^+ U^+, E^+)$$

We define Z_R on the RHS of the coupling interface:

$$Z_R = (\alpha_1^+, \rho_1^+, U_1^+, P_1^+ = P^+, \rho_2^+, U_2^+, P_2^+ = P^+)$$

This is achieved by enforcing a pressure, velocity and temperature equilibrium between phases. For more details, one can refer to [92].

Solving the Riemann problem

The Riemann problem at the coupling interface associated with father model, Z_L and Z_R is solved using either the Rusanov scheme or an approximate Godunov scheme [97]. The interface state $Z^* = Z^{Riemann}(Z_L, Z_R, (x - x_{int})/\Delta t = 0)$ is accounted for as a boundary conditions through a flux prescription. Once the Z^* is known, the flux on RHS of the interface may be calculated as:

$$F_\rho^+ = (\alpha_1 \rho_1 U_1 + \alpha_2 \rho_2 U_2)^*$$

$$F_{\rho U}^+ = (\alpha_1 (\rho_1 U_1^2 + P_1) + \alpha_2 (\rho_2 U_2^2 + P_2))^*$$

$$F_E^+ = (\alpha_1 U_1 (E_1 + P_1) + \alpha_2 U_2 (E_2 + P_2))^*$$

The mass flow rate for the vapor is $F_{\rho C}^+ = (\alpha_1 \rho_1 U_1)^*$.

3.6 Conclusions

Considering objectives of current thesis, only single-phase flow is taken into account since there are some particular difficulty when performing two-phase flow coupling:

- there are few related experiments which can be considered as reference to validate coupling results;

- computational codes are limited since certain codes are designed to launch single-phase flow simulation;
- field variables exchanged between two solvers should contain terms related to gas phase which will aggravate the numerical instability of coupling work;
- physical phenomenon of two-phase flow is more complex compared to single-phase one.

The coupling of pre-existing two-phase flow codes represents a challenging research framework. A first obvious reason is that there exists no consensual model for the description of two-phase flows. A second reason is that there is little theoretical work available in the current literature for the interfacial coupling of distinct codes. Consequently, it is better to start with some simple cases, only the single-phase adiabatic water flow is taken into account hereafter. By considering a single-phase approach, all models derive to a single-phase equation system, and thus implicitly, the two-phase coupling problem is eliminated.

Chapter 4

Verification and validation through test cases

This chapter presents the verification of the developed multi-scale computational methodology with tests on simple pipe flow calculations which are published in an international conference [98] and a peer-reviewed journal [99]. The technique is based on partitioned approach and fixed-point iteration. Field variables exchanged between solvers along with explicit and implicit numerical schemes are presented in previous chapter. The coupled works between CFD/CFD codes and CFD/SC codes are realized successively to test the reliability of current coupling methods.

The flow is generally turbulent and the used turbulence model is $k - \varepsilon$. The used boundary conditions for the full domain in all cases of the current section are described in Table 4-1.

Table 4-1: Boundary conditions

Boundary conditions	Inlet velocity	Outlet pressure
Types	Dirichlet	Neumann

4.1 Coupling of CFD/CFD

In the present section, the coupling between CFD and CFD codes is performed in a first stage to test the coupling method's flexibility and the specific influence of the mesh density ratio between coupled domains. A verification procedure with increasing complexity from one-dimensional flow to a more complex two-dimensional one, including the reverse flow, is presented below. Only 2D cases are considered in this stage, so "one/two-dimensional flow" means that there is one/two non-zero velocity component(s) at the coupling interface.

Different test cases are performed to verify the coupling methods. The influence of domain overlap (or not) are tested on all cases except the open pipe flow one with uniform inlet flow where the

difference of explicit/implicit algorithms is investigated. Besides, when the flow is perpendicular to the interface, the cases with non-uniform inlet flow are implemented to test linear interpolation method. Then, test cases are carried out to verify the prolongation and restriction procedures when there is transverse flow at the interface. Finally, different types of boundary conditions (Neumann/Dirichlet) are used to check the possibility of reverse flow simulation when there is feed-back effect at interface.

4.1.1 One-dimensional flow

In the current implementation, the flat velocity profiles are imposed firstly in the CFD code. On the other hand, for pressure transformation, extrapolation of the interface value should be performed based on the volume-centered pressures in the nearest volume and pressure variation slope from the upstream code.

Uniform inlet flow

The preliminary object is to couple NEPTUNE and FLICA4 together, since both codes are able to launch two-phases simulations. But as the coupling is realized through a master-slave way, NEPTUNE_CFD is temporarily chosen to replace FLICA4 as the SC solver due to technical issues. To test the numerical algorithm, a simple coupled problem consisting of single-phase water flow in an open pipe has been addressed. Computational domains considered are square tubes with different lengths. The analyzed pipe is of length $L = 6$ m and the side of the square is $a = 0.0661$ m. Using the domain decomposition method, the original domain is divided into an SC domain simulating the upstream part of length $L_{SC} = 1$ m, and a CFD domain resolving the remaining part of the pipe. Computation mesh for SC solver is quite coarse with only one cell in transverse section while that for CFD code is fine enough, both in radial and axial direction.

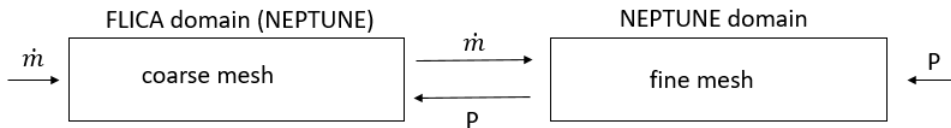


Figure 4-1: Schematic diagram of computational domains

For simplification, only one coupling interface is created, boundary conditions at the inlet/outlet are set as constants, field variables are exchanged once from one scale code to another scale code. The representation of the implemented model is depicted in Fig.4-1. Both explicit and implicit numerical algorithms mentioned previously are implemented in our test cases. To validate their results, a reference CFD simulation of the analyzed pipe (named as stand-alone method) is launched with fine computation mesh. Besides, NEPTUNE_CFD allows us to run simulations with a non-conforming mesh (named as face joining method) [100], which geometrically connect two sub-

meshes with different mesh densities. Different validation cases cited previously are represented in Figure 4-2.

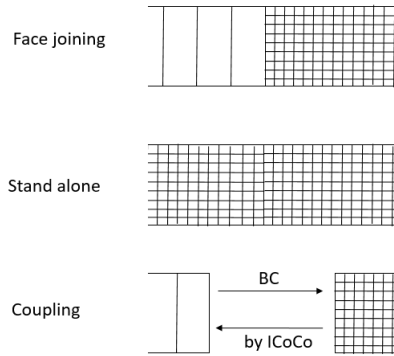


Figure 4-2: Different validation cases

One important indicator for the validation of coupling results is to verify the conservation of transported quantities at the coupling interface. Concerning the mass conservation, the gap between the mass flow rate from the SC domain and that to the CFD domain is less than 0.1%. It is more interesting to present pressure variation along the overall pipe as shown in Figure 4-3. Results of the implicit coupling method are closer to reference ones compared to the explicit coupling method and there is no significant difference between two cases, but for more complex cases, the difference will be significant and cannot be ignored.

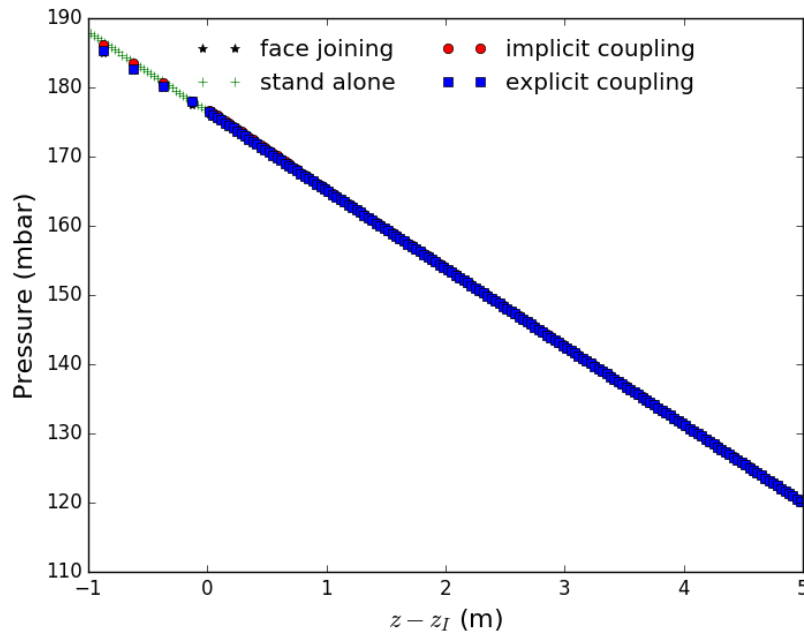


Figure 4-3: Pressure variation along the pipe

Considering field variables transferred from SC code to CFD solver, especially for mass flow rate which depends on flow velocity, a flat velocity profile is generally imposed at the coupling interface of CFD. The spatial dispersion information is lost and is not coherent with the real situation. To keep the spatial dispersion profile relative to a mean value, a non-uniform velocity profile based on the profile of CFD solution at the previous time step is applied. Flow velocity at cell i for the time level n is defined as $v_i^n = \bar{v}^n A_i^n$ with A_i^n the coefficient homogenized by the averaged velocity at interface, expressed in the following form:

$$A_i^n = \frac{v_i^{n-1}}{\bar{v}^{n-1}} \quad (4.1)$$

As mentioned previously, a non-uniform radial velocity distribution has been imposed based on simulation results of CFD domain at the previous time step. Improved results are depicted in Figure 4-4, the use of a non-uniform profile at the coupling interface enhances the results in the CFD domain while there is still improvement to make since the discrepancy compared to the reference is not negligible.

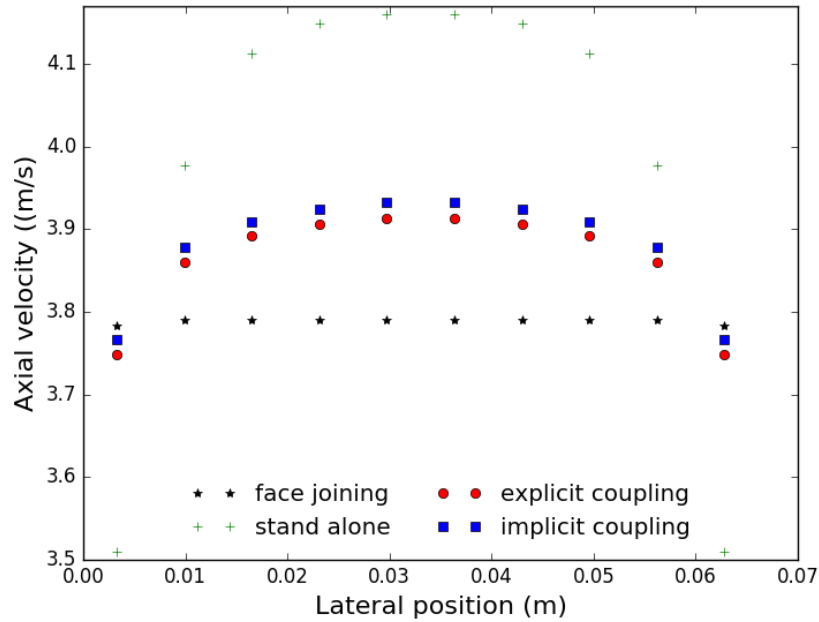


Figure 4-4: Radial velocity distributions at different cases

Then, we try to construct a continuous velocity profile through linear interpolation method from results of SC code, the coarse domain is not one cell in test section anymore. What's more, the influence of domain partially overlapping is investigated. The following, the implicit coupling scheme is used because it is more flexible and needs fewer time steps to converge. In the first step, the coupling is checked with identical mesh densities, then restriction and prolongation procedures are applied for different mesh densities. To test the developed interpolation method, a non-

uniform velocity profile is imposed at the inlet. Besides, the relative error is defined to present the advantages of the interpolation method quantitatively over the classic one.

Non-uniform inlet flow

A simple coupled problem consisting of single-phase isothermal water flow in a two-dimensional open pipe has been addressed to test the developed data exchange method. The analyzed pipe is of length $L = 0.2$ m and internal diameter $D = 0.1$ m. In the coupled problem, the original domain is divided into a coarse domain simulating the upstream part of length $L_1 = 0.1$ m, and a fine domain resolving the remaining portion of the pipe. The representation of the implemented model is depicted in Figure 4-5.

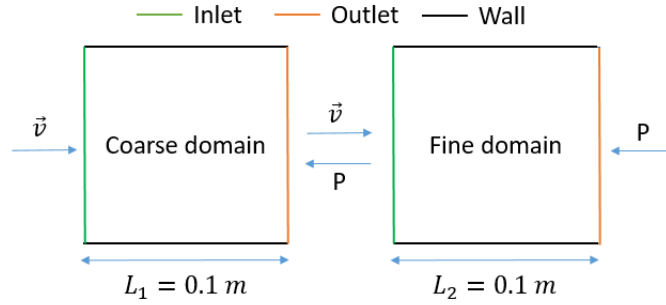


Figure 4-5: Schematic diagram of one-dimensional flow configuration

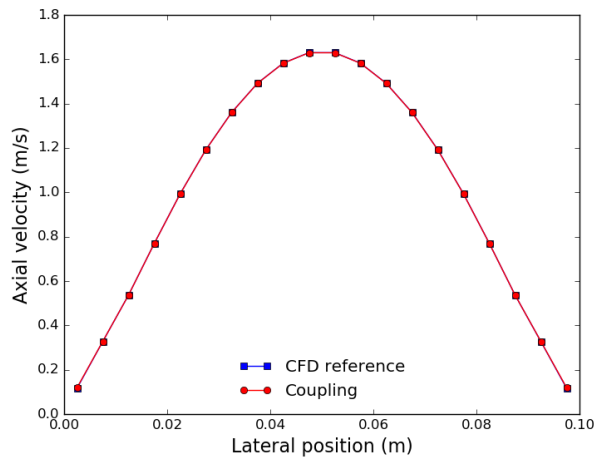
We compare lateral velocity profiles after the interpolation with that of the classic coupling method (uniform by pieces) [21]. The relative error (δ) compared to reference results is defined as:

$$\delta = \frac{|U - U_{ref}|}{U_{ref}} \quad (4.2)$$

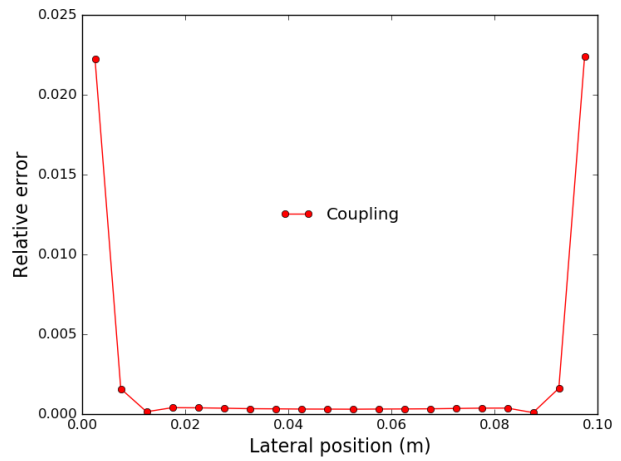
Three different cases are considered based on the ratio of mesh densities (fine/coarse domain), which are named as R1, R2 and R4 hereafter for the case where ratio = 1, 2 and 4 respectively. A non-uniform velocity profile is imposed at the inlet of the coarse domain as the following:

$$U(y_i) = 4 \sin\left(\frac{y_i}{D} \pi\right) \text{ m/s} \quad (4.3)$$

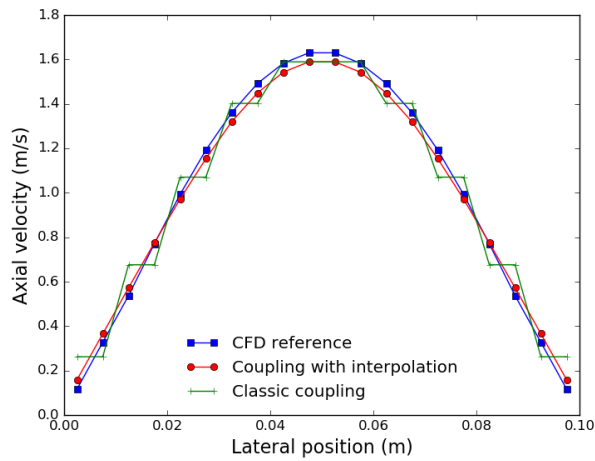
Without overlap Figure 4-6 shows the comparison of the lateral velocity profiles normalized by average velocity between coupling results and reference ones. For coupling with same mesh densities, results are close to reference ones, which means that errors due to the coupling operation could be ignored.



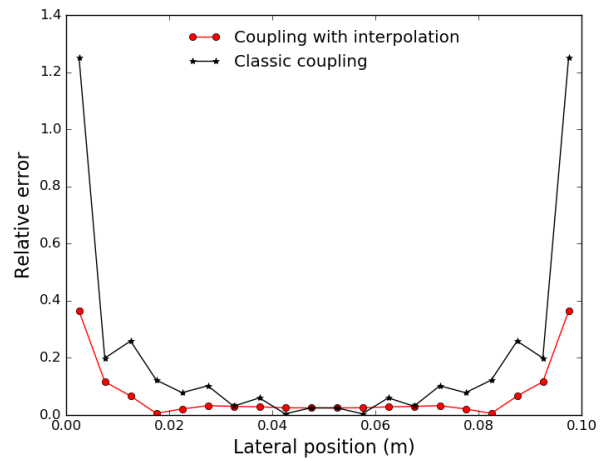
(a) R1



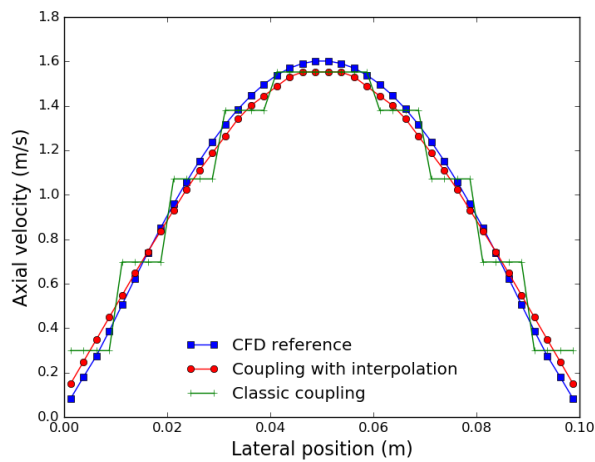
(b) Relative error for R1



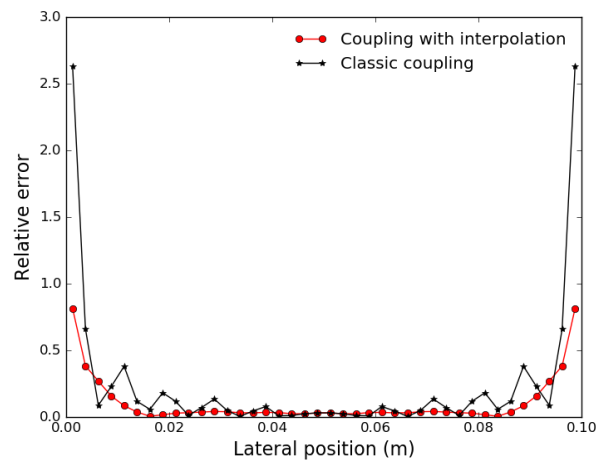
(c) R2



(d) Relative error for R2



(e) R4



(f) Relative error for R4

Figure 4-6: Velocity profiles without domain overlapping for different cases (left) and corresponding relative errors (right)

Profiles after interpolation show good agreement with reference ones and their relative errors have overall lower values in the transverse section than that of classic coupling. For each case, relative errors are more significant at the boundary region since velocities at this region are close to zero; even a tiny deviation can lead to a relatively more significant error. Besides, the interpolation error increases when the ratio increases, which is logical since more information is lost during the data exchange.

With partial overlap To test the domain partially overlapping method, the same case with upstream domain partially extended as depicted in Figure 4-7 has been realized.

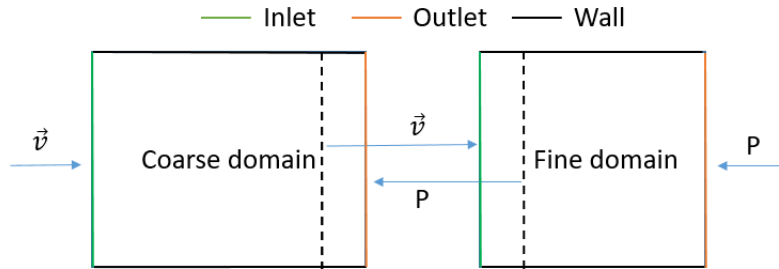


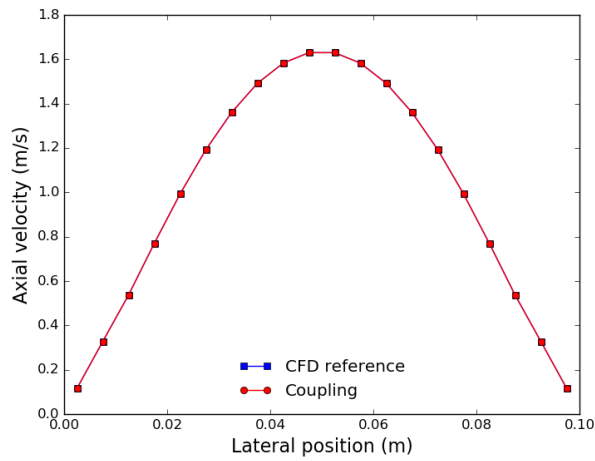
Figure 4-7: Schematic diagram of one-dimensional flow configuration with domain partially overlapping

Results are close to the case without overlap, as shown in Figure 4-8 and Table 4-2. Domain partially-overlapping method is more complex to be implemented compared to the one without overlap since internal cell information is concerned. So for one-dimensional flow, the method with non-intersecting subdomains is enough to perform the coupling work.

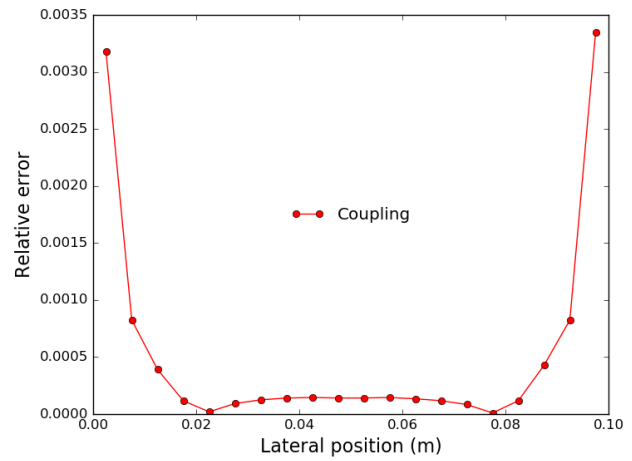
Table 4-2: Relative errors for cases with and without overlap

Run name	Without overlap		With overlap	
	Max error	Min error	Max error	Min error
R1	3.08E-2	2.56E-4	3.18E-3	2.01E-5
R2	3.64E-1	5.83E-3	3.45E-1	6.61E-3
R4	8.15E-1	5.21E-3	7.92E-1	5.92E-3

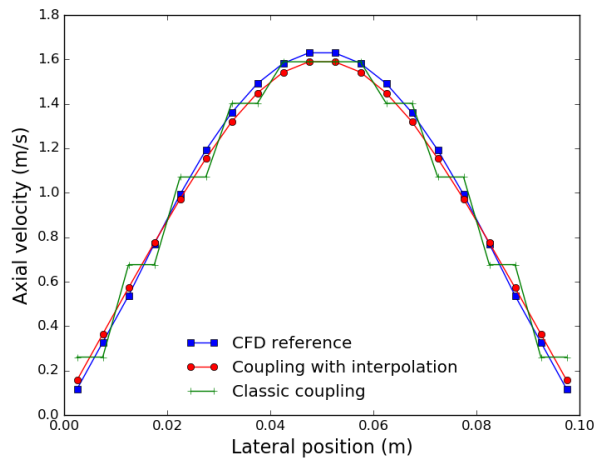
During the data exchange between two solvers, it has to guarantee that mass flow rates are conserved at the coupling interfaces. For test cases with different ratios, Table 4-3 represents results at two sides of coupling interface, relative errors are all inferior to 1% and could be considered as negligible. Cases with and without overlap show good agreement with each other.



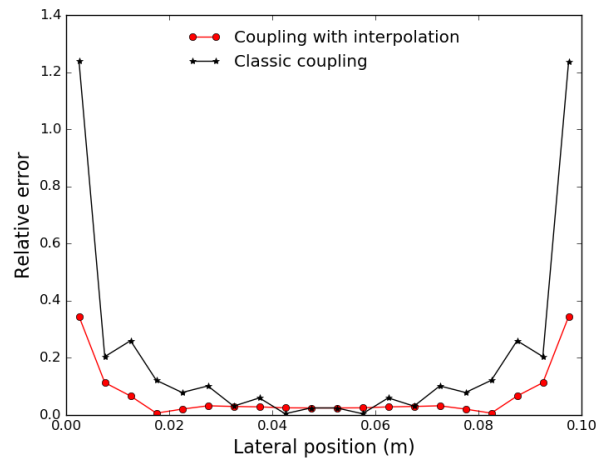
(a) R1



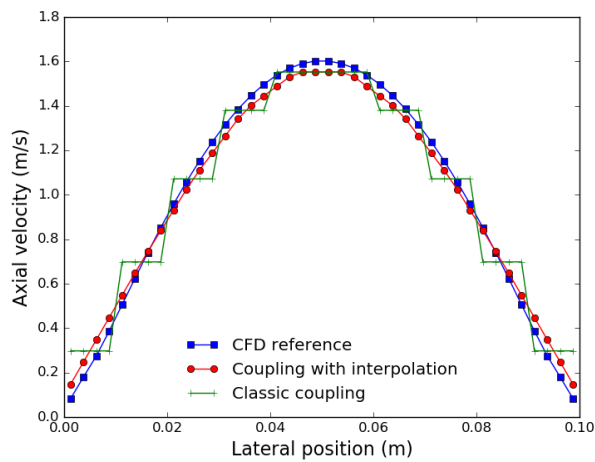
(b) Relative error for R1



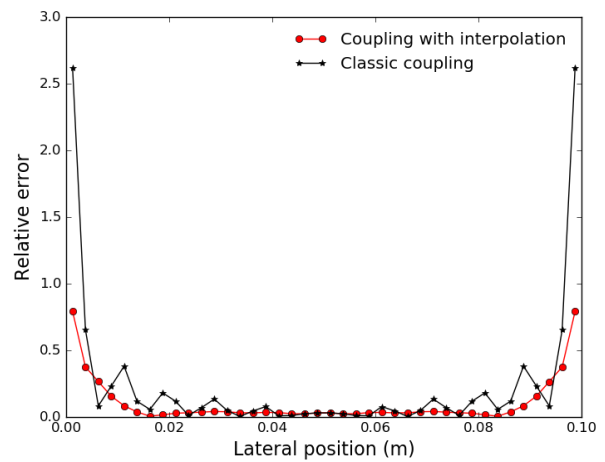
(c) R2



(d) Relative error for R2



(e) R4



(f) Relative error for R4

Figure 4-8: Velocity profiles with domain partially overlapping for different cases (left) and corresponding relative errors (right)

Table 4-3: Mass flow balance for different test cases

Cases	Without overlap			With overlap		
	Coarse (kg/m·s)	Fine (kg/m·s)	Error	Coarse (kg/m·s)	Fine (kg/m·s)	Error
R1	1.00E-1	1.00E-1	-	1.00E-1	1.00E-1	-
R2	9.99E-2	9.89E-2	1.02E-2	1.00E-1	9.89E-2	1.04E-2
R4	9.99E-2	9.90E-2	9.90E-3	1.00E-1	9.89E-2	1.00E-2

To show the pressure distribution at the coupling region, we chose the case with same mesh densities. As depicted in Figure 4-9, the pressure is conserved when passing the coupling interface, related analysis is also presented in the previous work [98]. The case without overlapping shows a slightly better agreement with the reference but the discrepancy between two coupling cases is not significant and is not further investigated.

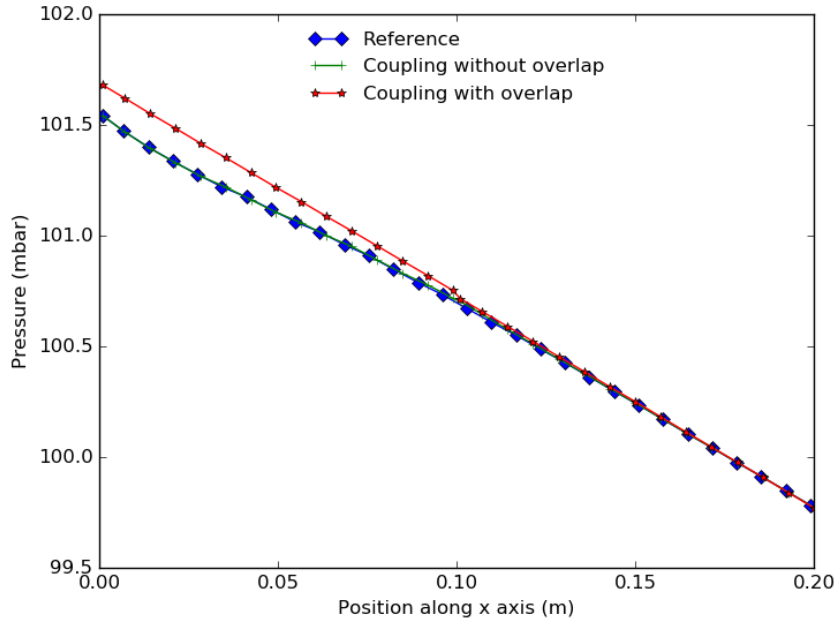


Figure 4-9: Pressure distribution at the coupling region for the case R1

4.1.2 Two-dimensional flow

The flow in a fuel assembly is not constrained to being perpendicular to the domain interface(s), especially when cross flow occurs. A more general case must thus be considered. A two-dimensional flow in an open field is introduced, derived from the open pipe model by changing boundary condition type of each side and the velocity profile imposed at the inlet. Horizontal and vertical components of the velocity field are denoted U and V respectively. The interface exchange of boundary conditions data between coupled domains, shown in Figure 4-10, follows the same way as that of previous case. The mesh densities of domains 1 and 2 can change to test the prolongation

and restriction procedures.

$$U(x_i) = V(x_i) = \begin{cases} 4\sin\left(\frac{2(x_i - D/4)}{D}\pi\right) \text{ m/s}, & D/4 \leq x \leq 3D/4, \\ 0 \text{ m/s}, & \text{else.} \end{cases} \quad (4.4)$$

The computational domain is in the atmospheric pressure, and a non-uniform velocity profile is imposed at the inlet of upstream domain as the above.

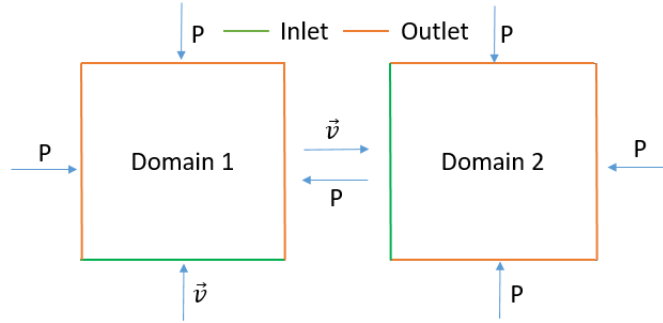


Figure 4-10: Schematic diagram of two-dimensional flow configuration

Without overlap

From the distribution diagram of velocity vectors, as shown in Figure 4-11 (left), one can conclude that the flow is heavily distorted in the region close to the coupling boundary. As a result, flow features in the downstream domain are not consistent with the reference, velocity component parallel to the coupling boundary tends to vanish. This is due to the classic pressure boundary condition which should be reconstructed to correct this situation, while that would reduce the generality of the proposed approach and is not the object of the current work.

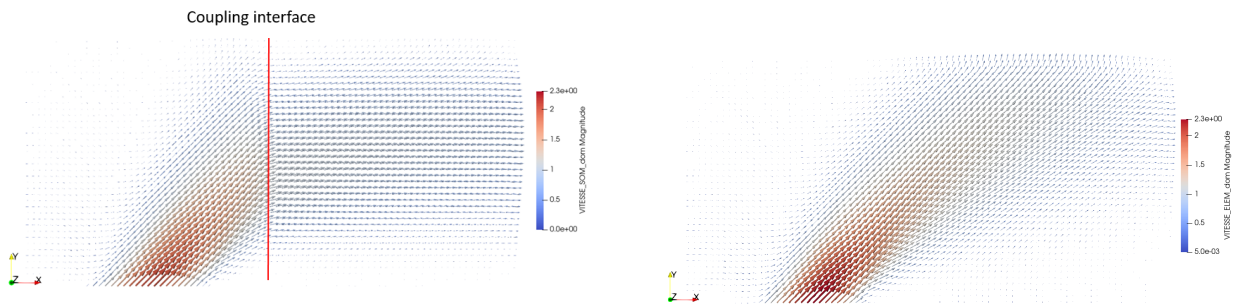


Figure 4-11: Velocity vector distribution: (left) classic coupling, (right) the reference.

With partial overlap

The space partially-overlapping method has been applied to this case. Instead of extracting the velocity profile at the Neumann boundary, velocity information in an interior layer is transferred to the downstream solver, as presented in Figure 4-12.

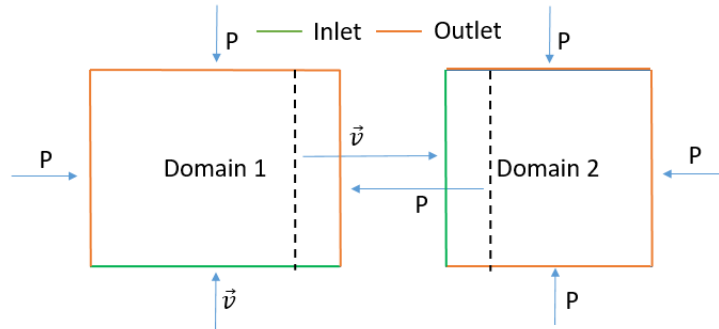


Figure 4-12: Schematic diagram of two-dimensional flow configuration with SPO method

A coupled problem between two domains with the same mesh density has been realized in the first instance to verify the reliability of coupling results. Then a coarser mesh with a cell size twice as large as that of fine mesh is used to perform the coupling work. For simplification, the coupling between fine/fine, fine/coarse and coarse/fine domains is named FF, FC and CF coupling, respectively hereafter.

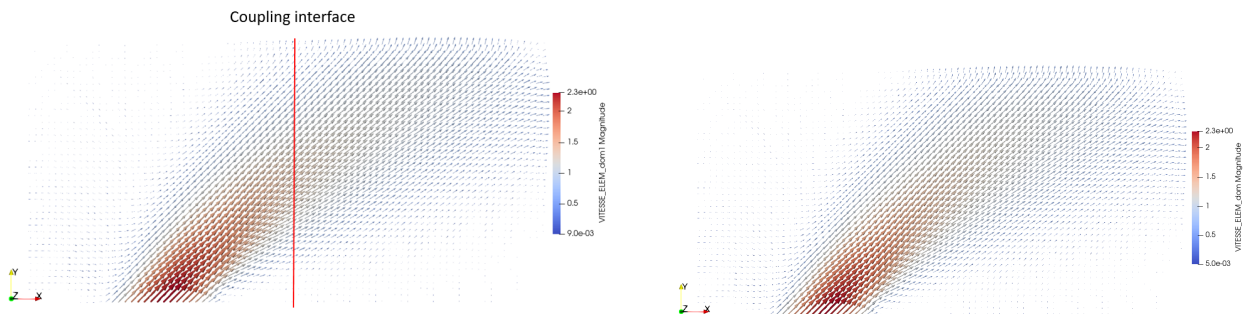


Figure 4-13: Velocity vector distribution: (left) FF coupling, (right) the reference.

Distribution visualizations are close between coupling results and reference ones, as depicted in Figure 4-13. In order to have a quantitative comparison between two cases, velocity profiles of each component at the interface are presented below:

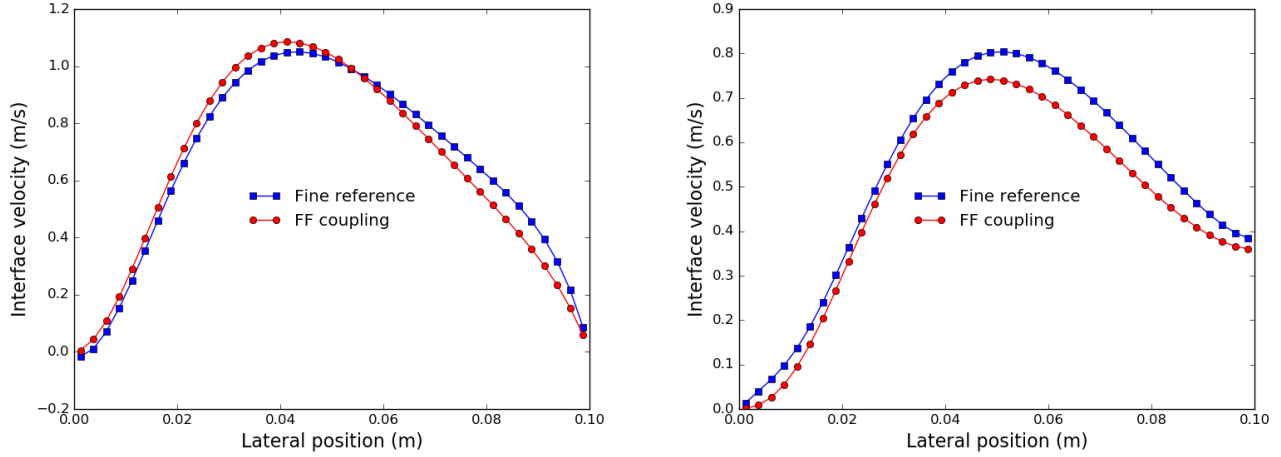


Figure 4-14: Velocity profile at the coupling interface: (left) U, (right) V.

For what presents in Figure 4-14, velocity profiles for U component are pretty close between two cases, while for V component, discrepancies become significant at the semi-upper region of the interface. As a result, coupling of one-dimensional flow gives better results than the two-dimensional one.

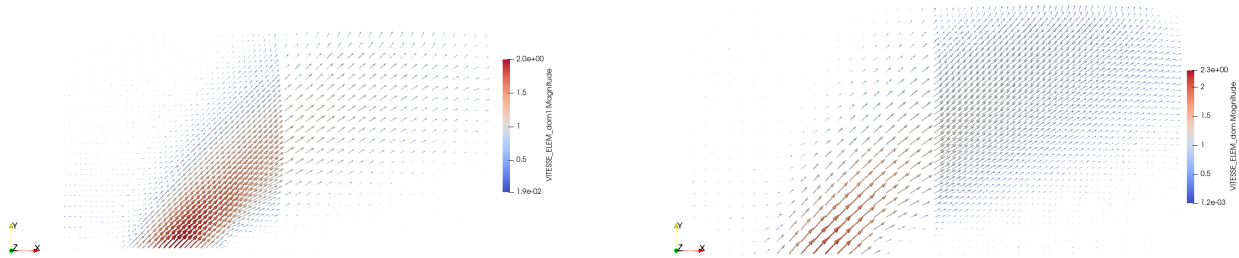


Figure 4-15: Velocity vector distribution: (left) FC coupling, (right) CF coupling.

Then, restriction and prolongation procedures are applied in this case, as exhibited in Figure 4-15. The flow direction has been conserved when passing the coupling interface due to the partially overlapping domain decomposition approach. More precise analysis concerning the velocity distribution of different components along the interface is presented below.

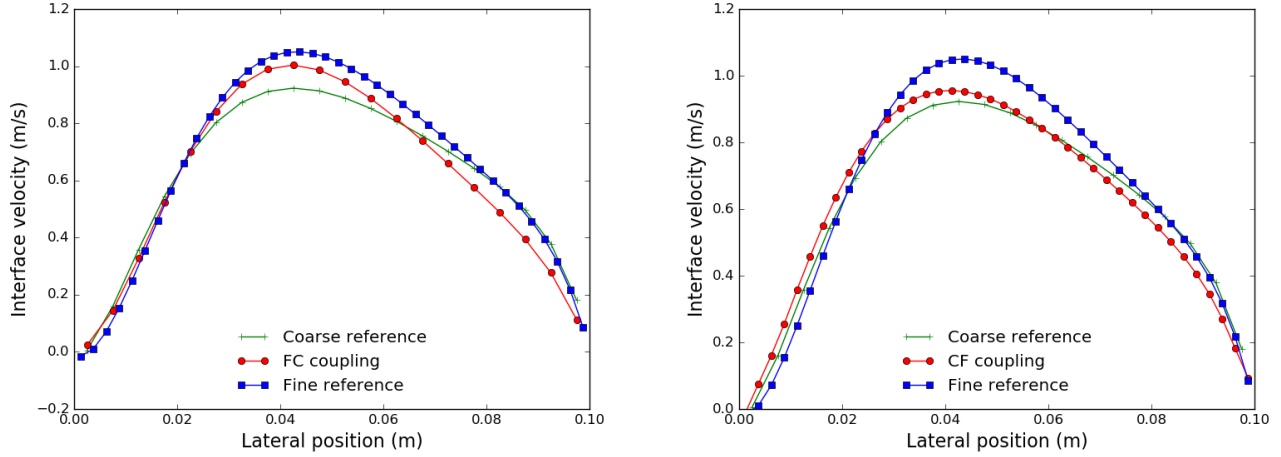


Figure 4-16: U profile at the interface: (left) FC coupling, (right) CF coupling.

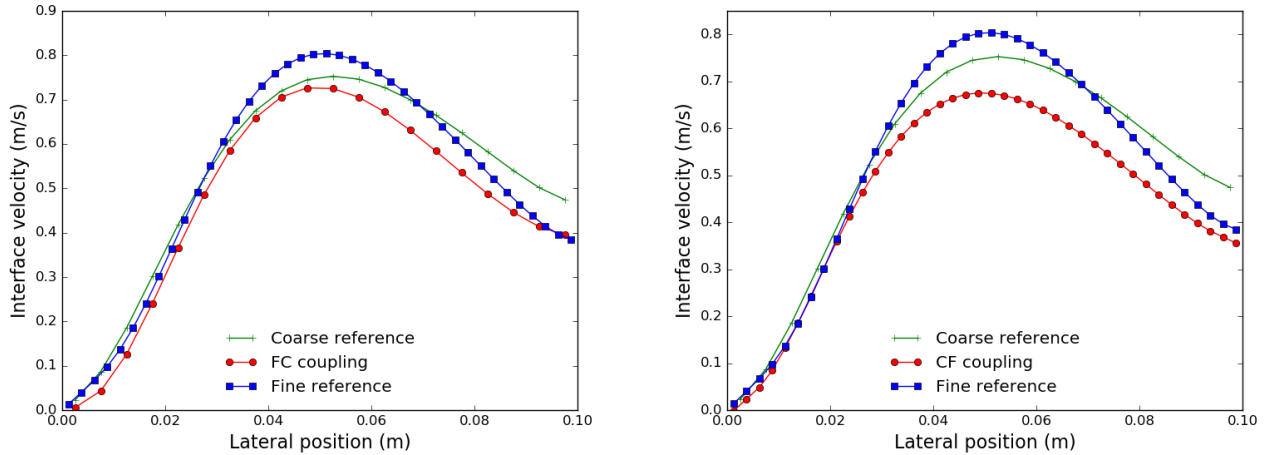


Figure 4-17: V profile at the interface: (left) FC coupling, (right) CF coupling.

As shown in Figure 4-16, velocity profiles of the U component show good agreement between two cases (FC coupling and CF coupling). In contrast, for the V component depicted in Figure 4-17, especially for the CF case, deviation becomes significant in the central region of the interface. As it could have been anticipated, the velocity component perpendicular to the interface seems more stable when performing a multi-scale coupling where the flow is not perpendicular to the interface. However, the partial overlap allows to retrieve a sufficiently accurate flow parallel to the interface, given the expectations associated to the SC/CFD coupling.

4.1.3 Reverse flow

A more complex case is considered in the present section to simulate a reverse flow, in order to test some limits of the proposed coupling framework, as well as the capabilities of alternating boundary

conditions compared to those previously used for data exchange between computational domains. No mesh transition is investigated in this section. Figure 4-18 (left) illustrates the domain. It is composed of a square whose side is $L = 0.3m$; at the bottom right side, there is a segment with Dirichlet boundary whose length is $L/3$ where a unit velocity is exerted, while at the upper left side of the domain, there is a segment of the same length with Neumann condition where the atmospheric pressure is imposed.

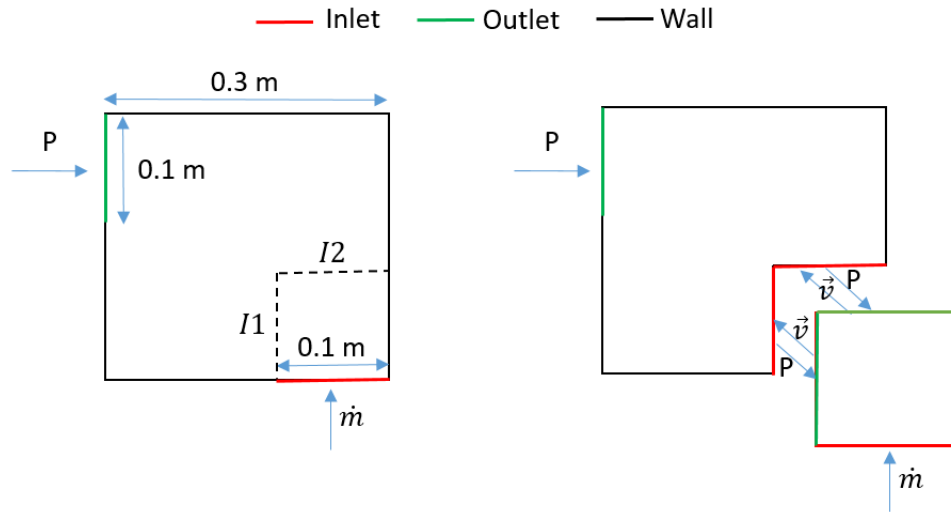


Figure 4-18: Diagram of reverse flow configuration: (left) the reference, (right) classic coupling.

Without overlap

In the coupled problem, the little square divided by two interfaces I1 and I2 is the upstream domain, the downstream solver simulates the rest. The classic coupling methods transfer the pressure information from the downstream code to the upstream one, as depicted in Figure 4-18 (right).

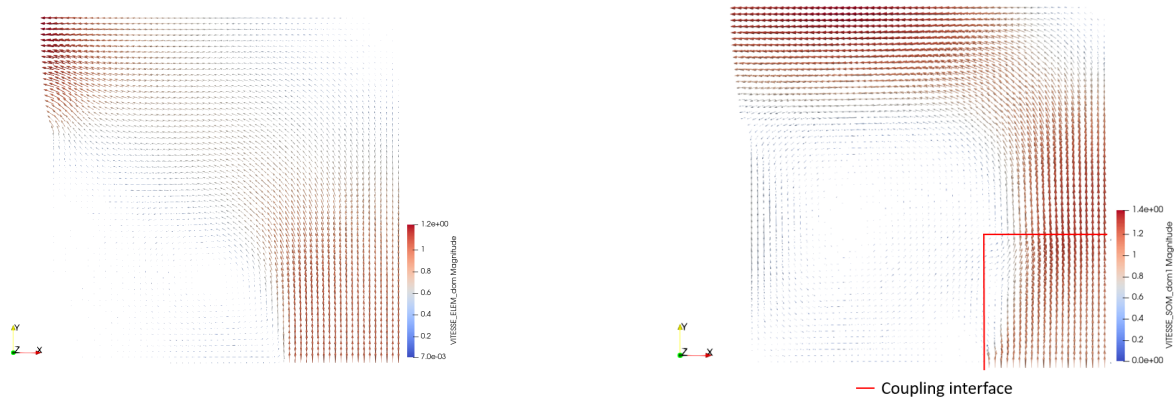


Figure 4-19: Velocity vector distribution: (left) the reference and (right) classic coupling.

Figure 4-19 shows the velocity vector distribution for each case. Considering vector distribution in the upstream domain, it has a relatively uniform feature for the reference, while for the coupling case, velocities in the left upper region have lower values.

With partial overlap and improved coupling conditions

Since the flow is disturbed in the region close to coupling interfaces, the partially overlapping method previously introduced is expected to provide some improvement in this case. Besides, another configuration is tested where the Neumann boundary conditions of upstream domain are replaced by Dirichlet ones, as shown in Figure 4-20. To ensure the mass conservation, the inflow is imposed to be equal to the outflow.

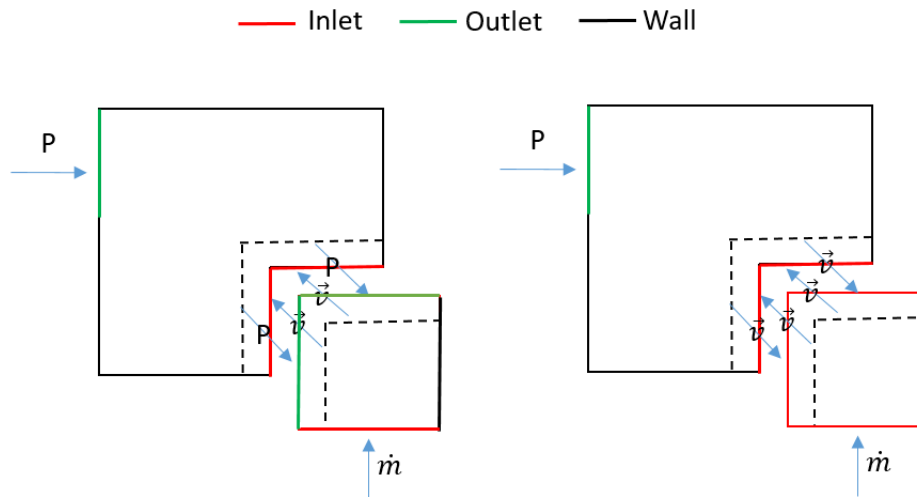


Figure 4-20: Reverse flow configuration with partial overlap: (left) pressure-velocity coupling , (right) velocity-velocity coupling.

Each solver must use a lower time step to reduce the numerical instability in the beginning phase of simulation. Here, time steps used by each solver are the same. In the end, velocity features with coupling shown in Figure 4-21 are improved compared to the reference.

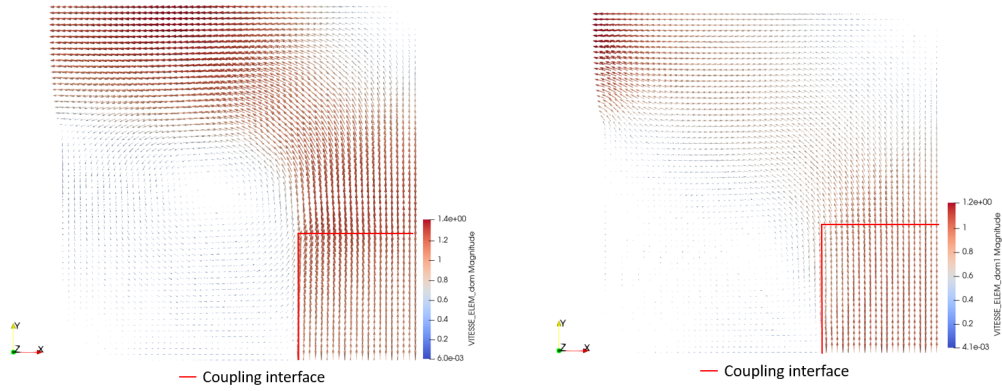


Figure 4-21: Velocity vector distribution: (left) pressure-velocity coupling (right) velocity-velocity coupling.

Figure.4-21 (left) and 4-22 show that velocities at the coupling interfaces have higher values compared to reference ones, and their directions are not consistent between the two cases. The pressure variation has little influence on the flow, and as a consequence, this way cannot treat the reverse flow correctly. The Dirichlet-Dirichlet coupling conditions thus significantly improve the coupled solution in this case.

To show more details, Figure 4-23 exhibits a comparison of each velocity component at the interface I2 for both coupling types. Significant discrepancies exist for both components in the coupling case, with again much better results obtained with the Dirichet-Dirichet coupling. Remaining discrepancies exist at the CFD level, but it is a practical limitation for the current approach which can yet be seen as consistent with what the porous SC code can accept.

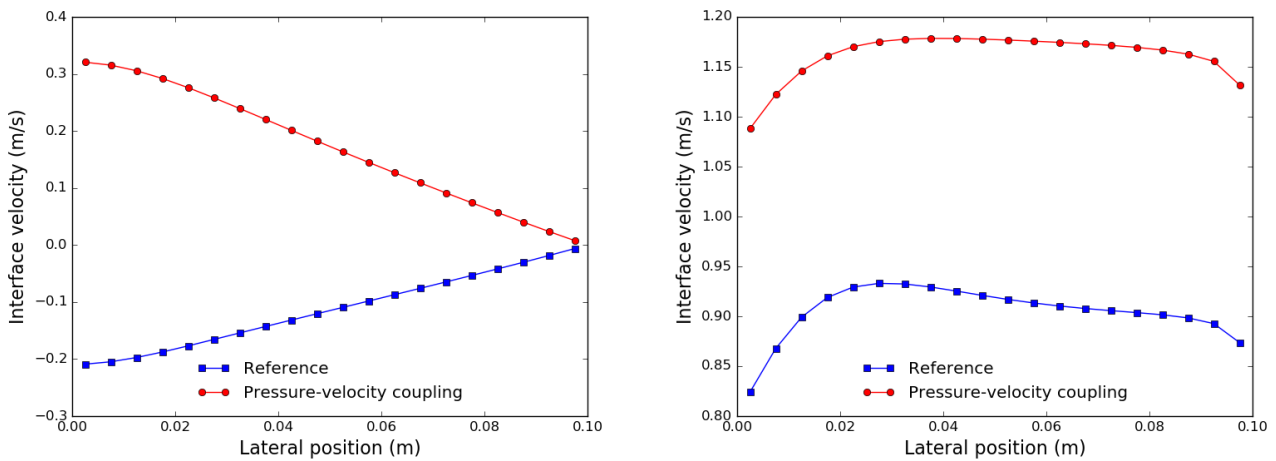


Figure 4-22: Velocity profiles at the interface I2 for pressure-velocity coupling: (left) U and (right) V.

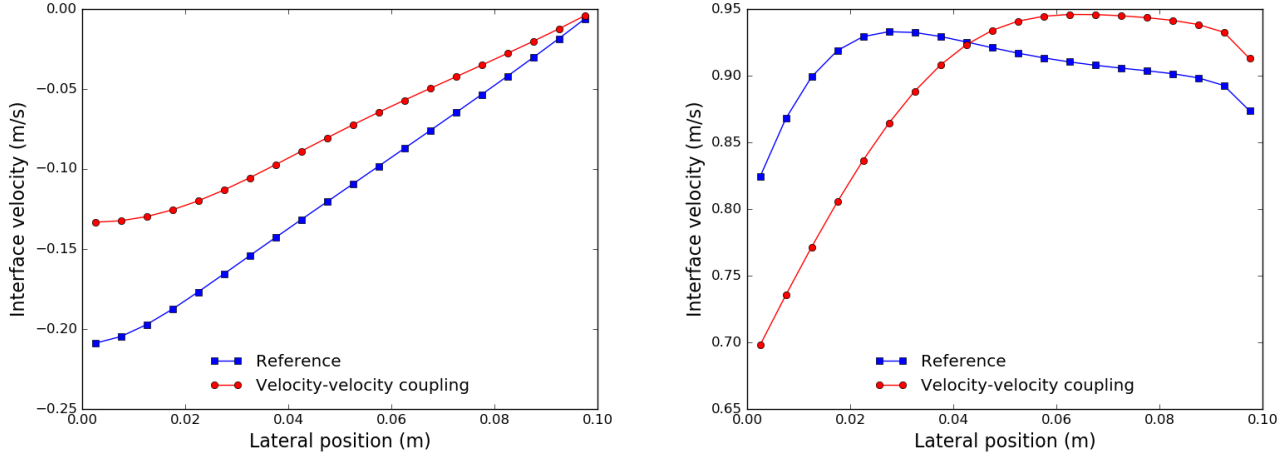


Figure 4-23: Velocity profiles at the interface I2 for velocity-velocity coupling: (left) U and (right) V.

It can be concluded that there are some limitations to simulating the reverse flow with a partitioned coupling such as that proposed in the present paper. However, the discrepancies are acceptable for the target SC/CFD coupling, with the general feature of the flow well captured with a Dirichlet-Dirichlet partially overlapping strategy.

The object of the following SC/CFD coupling is to perform the preliminary verification when considering two solvers with different scales and check that implicit numerical scheme works well in this case. Besides, a monophasic code is employed as the CFD solver while the SC code uses two-phase flow models which allows us to test the interoperability of the approach with another solver.

4.2 Coupling of SC/CFD

Another coupling work between FLICA4 and TrioCFD which is designed for single-phase simulation has been realized to be able to monitor two different solvers at the same time. Besides, the coupling work is realized in a generic way that is more flexible. There is no significant influence on results between different numerical algorithms, while for our case, the implicit one is chosen since it is more flexible and needs fewer time steps to converge.

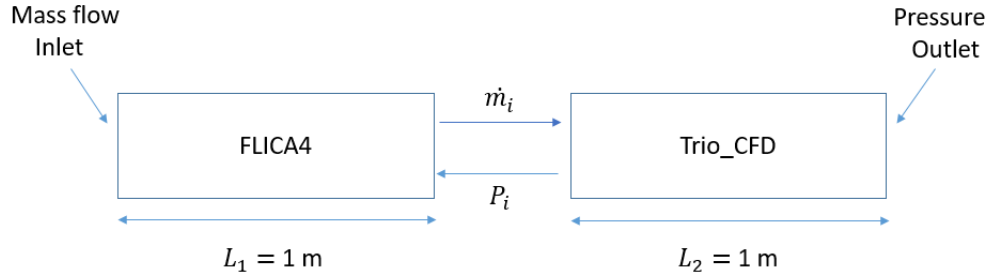


Figure 4-24: Schematic diagram of FT configuration

4.2.1 FT mode

The configuration of the coupled run is depicted in Figure 4-24 with the same transverse section as before. The first part is modeled in FLICA4, while the second one is modeled using TrioCFD. This configuration is referred to as "FT", shorthand for FLICA4/TrioCFD, indicating that the CFD code is downstream of the SC component. The data exchange at the coupling interface is the same way as previously mentioned. Firstly, a constant mass flow rate is imposed at the inlet of SC domain. The pressure variation along the computational domain is shown in Figure 4-25 where TrioCFD and FLICA4 correspond to standalone simulations performed respectively with TrioCFD code and FLICA4 code, results between different cases are quite coincident.

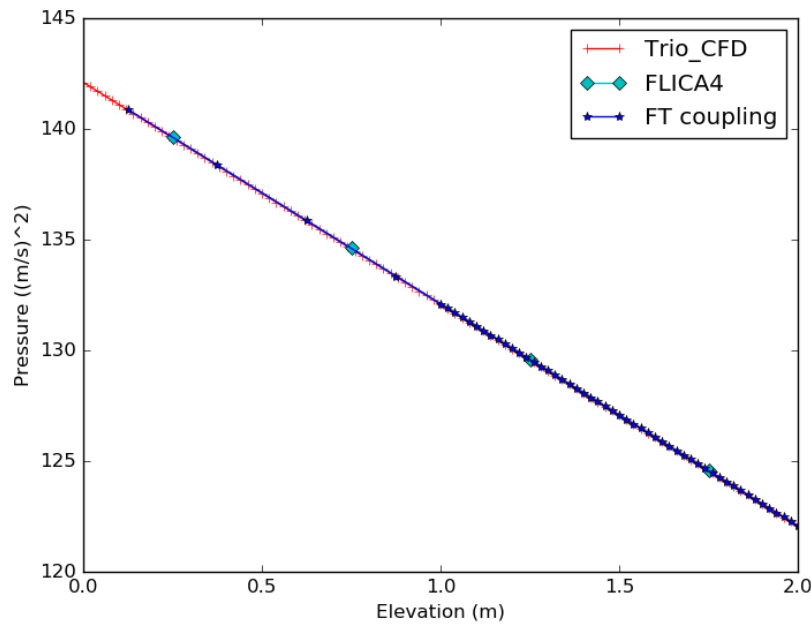


Figure 4-25: Pressure variation along the computational domain in FT configuration

Secondly, a transient scenario is considered, more precisely, a transient inlet mass flow was applied to the inlet of the pipe:

$$\dot{m}_{in} = \begin{cases} 1200.0 \text{ kg}/(m^2s), t < 1.0s, \\ 1200.0 + 1000 \times (t - 1.0s) \cdot s^{-1} \text{ kg}/(m^2s), 1.0s \leq t \leq 2.0s, \\ 2200.0 \text{ kg}/(m^2s), t > 2.0s. \end{cases} \quad (4.5)$$

The resulting pressure drops of the entire domain are shown in Figure 4-26. Coupling results show good agreement with reference ones. It should be noticed that the time steps used in this mode are the same in the first instance.

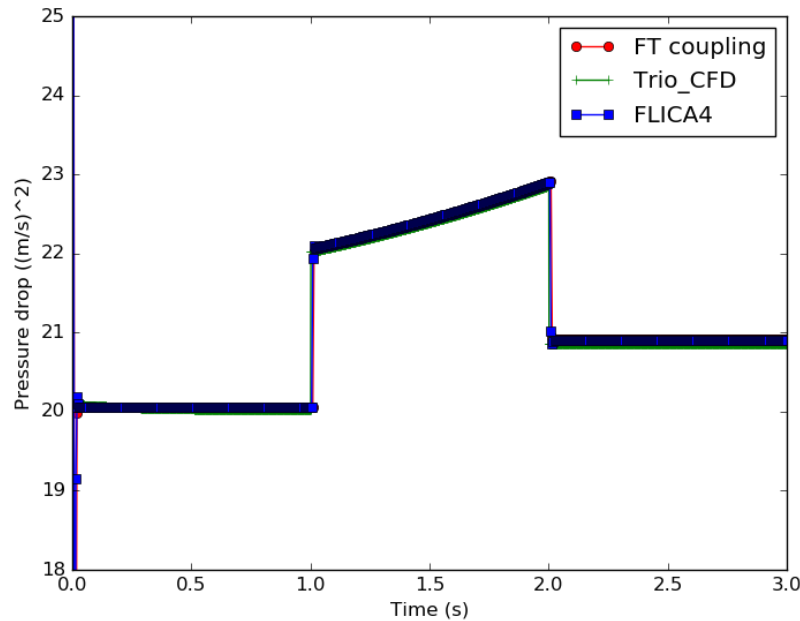


Figure 4-26: Transient results in FT mode with same time step

But with a different time step for each code, results could be different, as shown in Figure 4-27, because mass flow rate at the inlet of CFD solver should remain constant during each larger time step of SC solver which is not coherent with the real situation. The SC code is considered as a filter and the velocity variation will be filtered.

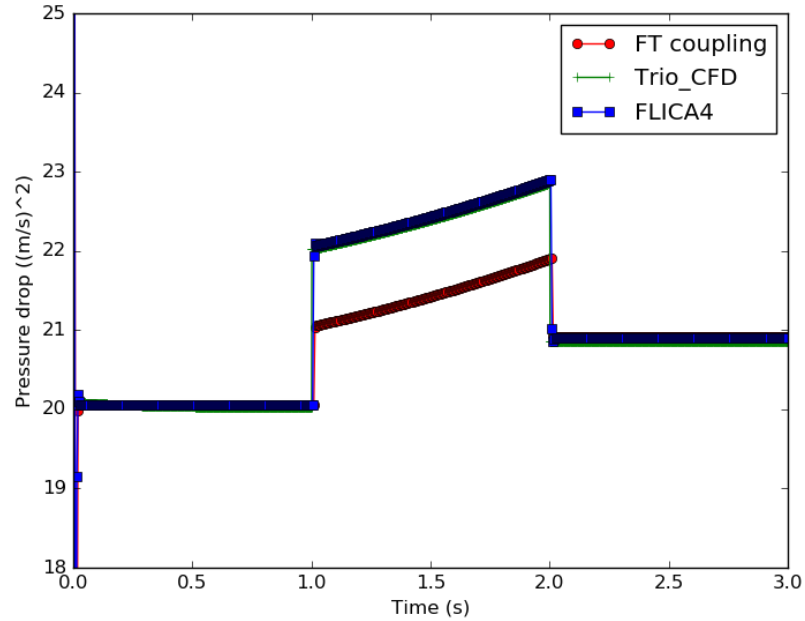


Figure 4-27: Transient results in FT mode with different time steps

4.2.2 TF mode

An imposed mass flow rate coupled case can be performed with TrioCFD on the upstream side, as the configuration shown in Figure 4-28. The data exchange is the same way as previously.

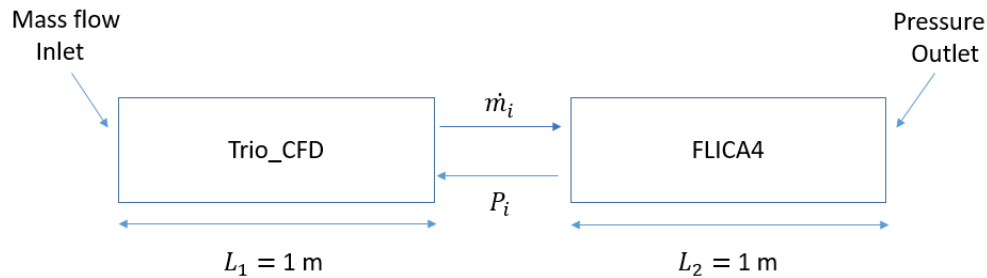


Figure 4-28: Schematic diagram of TF configuration

Steady-state pressure variations for TF case are shown in Figure 4-29. Results are similar to that of FT mode.

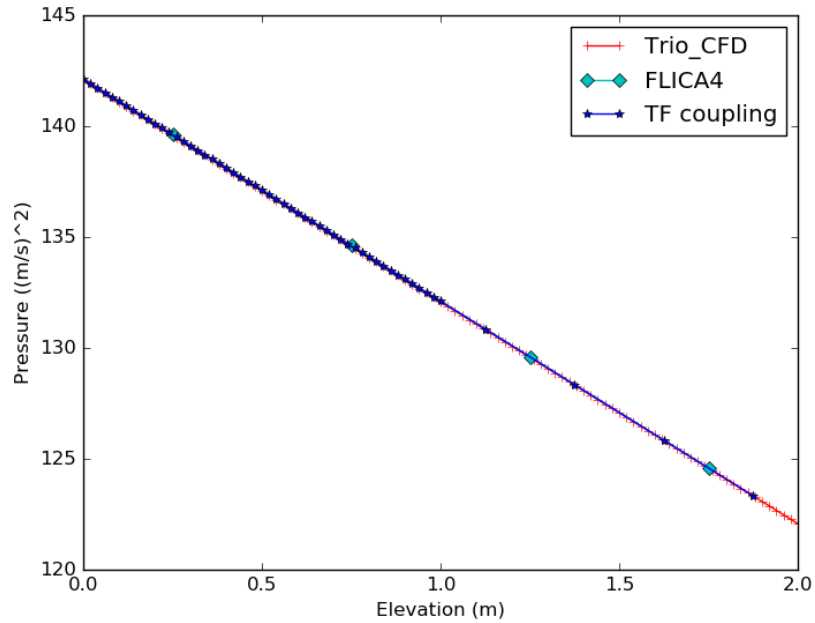


Figure 4-29: Pressure variation along the computational domain in TF configuration

While for the transient scenario, results remain the same with time step of SC solver larger than (or equal to) that of CFD solver because SC solver is in the downstream side, there is no loss of information for both codes, as shown in Figure 4-30. It can be concluded that this mode is more flexible compared to the previous one.

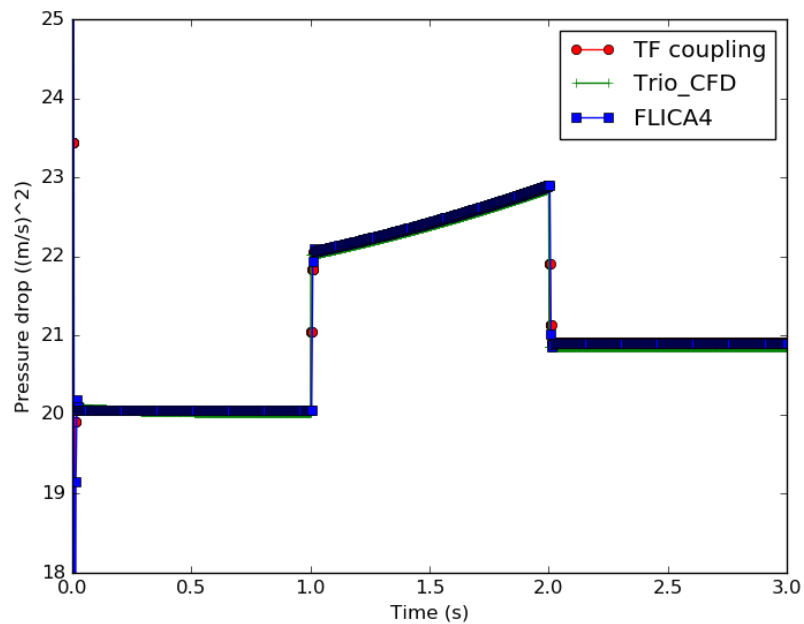


Figure 4-30: Transient results in TF mode compared to standalone reference values

4.3 Conclusions

The domain decomposition approach is chosen as the spatial coupling method. Multi-grid data exchange methods such as prolongation and restriction procedures are used to transfer velocity information in one direction and pressure in the reverse direction. Explicit and semi-implicit numerical coupling algorithms are implemented in the case of a multi-scale coupling between a coarse and a fine CFD domain with the use of a spatial enrichment method that aims at preserving the velocity profiles in the fine domain.

For the one-dimensional case with uniform inlet flow, the coupling results are compared by reference CFD simulations and some also with the face joining method. Mass conservation is ensured by comparing mass flow rates at two sides of coupling interface with an error less than 0.1%. The pressure variation along the pipe in the coupling cases is close to the reference one and the radial velocity profile has been improved by imposing a non-uniform profile based on the spatial dispersion of the previous time step.

Considering other cases of CFD/CFD coupling, the results for flow perpendicular to the coupling interface are similar for both overlapping and non-overlapping approaches. The linear interpolation integrated in the prolongation procedure improves the solution in the fine domain which is closer to the reference solution. When the types of boundary conditions available in each solver are classical (Dirichlet or Neumann) and the flow is non-orthogonal to the coupling interface, the overlapping approach gives better results because the flow direction is conserved. In the case of non-overlapping approach, the pressure boundary condition is not recommended since it imposes an orthogonal flow direction that is propagated in all the domain via the data exchange. In the case of reverse flow, when the flow leaves the domain via a pressure boundary condition and goes back, the re-entering flow rate cannot correctly be taken into account by the upstream domain using Neumann conditions for the outlet flow. It is thus better to switch to Dirichlet boundary condition type for the coupling interface with the overlapping approach, situation that is closer to the MS method.

In the case of SC code and CFD code coupling approach, coupling results are compared with reference CFD and SC ones both in TF mode and FT mode. The mode with CFD code in upstream seems to be more flexible for transient scenarios since there is no loss of information for both codes, while there is some information lost with SC code in the upstream. The dynamic is well reproduced in both cases according to the pressure profiles obtained with the coupling simulations. The preliminary verification of coupling methods between different solvers has been realized and the possibility to use a monophasic code has been checked.

It should be reminded that the classical boundary conditions available for each solver are applicable

to only one transferred variable which is different from the original domain decomposition methods. The development of specific boundary conditions is recommended in the future work to better simulate the reverse flow and have a more intricate coupling between codes.

Chapter 5

Semi-industrial implementation and experimental validation

5.1 MANIVEL experiment

This section presents the MANIVEL experimental facility used as the reference to validate coupling results between SC and CFD codes. It can also be used to construct a CFD reference calculation from which numerical parameters set in the coupling work could be copied. The benchmark experiment consists of two test series: axial velocity distribution and pressure drop. Run conditions and related experimental data are provided in the following.

5.1.1 Context of benchmark experiment

The NESTOR project, carried out by the CEA-EDF-EPRI group in the framework of Crud-Induced Power Shift (CIRS) risk assessment analyses of PWR cores, was designed to produce accurate thermal-hydraulic (T/H) experimental data on 5x5 rod bundles. This project has obtained high fidelity data on the single-phase heat transfer and the ONB boundary in a nuclear fuel bundle based on dedicated single-phase heat transfer correlations, and an associated ONB wall superheat criterion. More precisely, it consists of:

- Exercise 1: hydraulic isothermal MANIVEL loop (measurement of grid pressure loss, and determination of axial velocity field by Laser-Doppler Velocimetry (LDV) in single-phase flow);
- Exercise 2: T/H OMEGA loop (rod inner-surface temperature measurements during *Single-phase tests* and ONB *tests* performed at PWR prototypical T/H conditions).

Here, only MANIVEL experiment was taken into account.

5.1.2 Description of the facility

A 5×5 square array of tube rods used as the test section for MANIVEL tests. The rod outer diameter was 9.5 ± 0.02 mm, the array pitch was 12.6 mm, and the rod-to-wall gap was 3.1 mm, resulting a $66.1 \text{ mm} \times 66.1 \text{ mm}$ bundle casing composed of 316 L stainless steel and plexiglass along the downstream LDV measuring area (see Figure 5-1). The overall length was about 5 meters.

The bundle were equipped with Simple Support Grids (SSG) spaced axially at 279 mm intervals. The SSG material is stainless ref.A.P.X4 from AUBERT & DUVAL supplier, as shown in Figure 5-2.

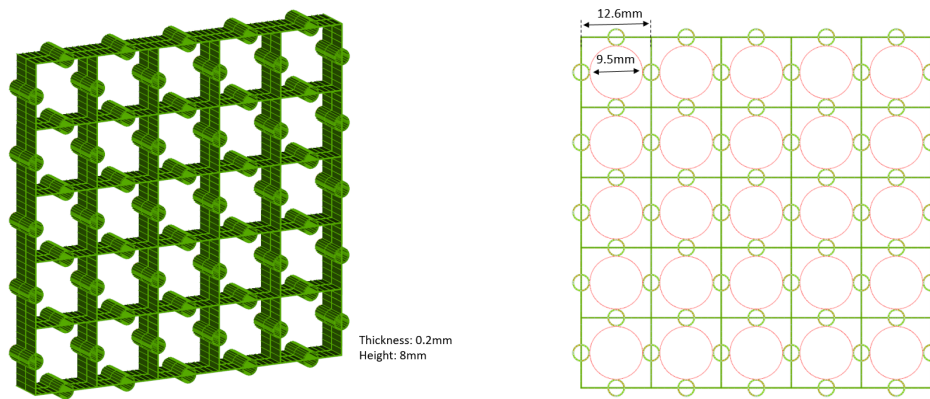


Figure 5-1: Schematics of the simple support grid

For the isothermal experiment (MANIVEL test), the dimension of the outer diameter of these rods was the same, as 9.5 ± 0.02 mm, but their inner diameter was different for 9 inner rods and 16 peripheral rods as follows (see Figure 5-3):

- The inner diameter of the 9 inner rods was 7.7 ± 0.02 mm; the thickness was 0.9 mm.
- The inner diameter of the 16 peripheral rods was 8.15 ± 0.02 mm; the thickness was 0.675 mm.

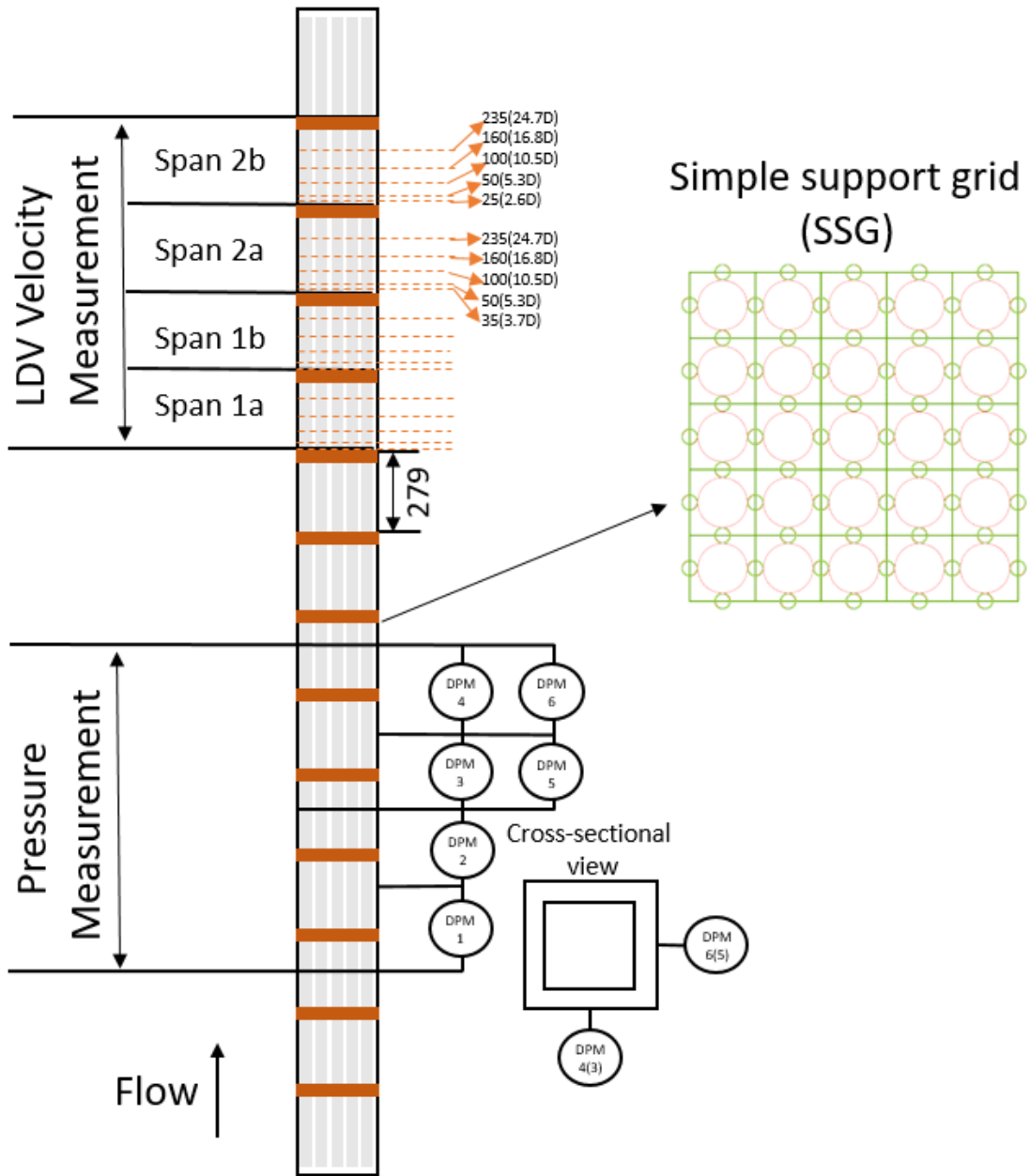


Figure 5-2: Schematics of the MANIVEL bundles

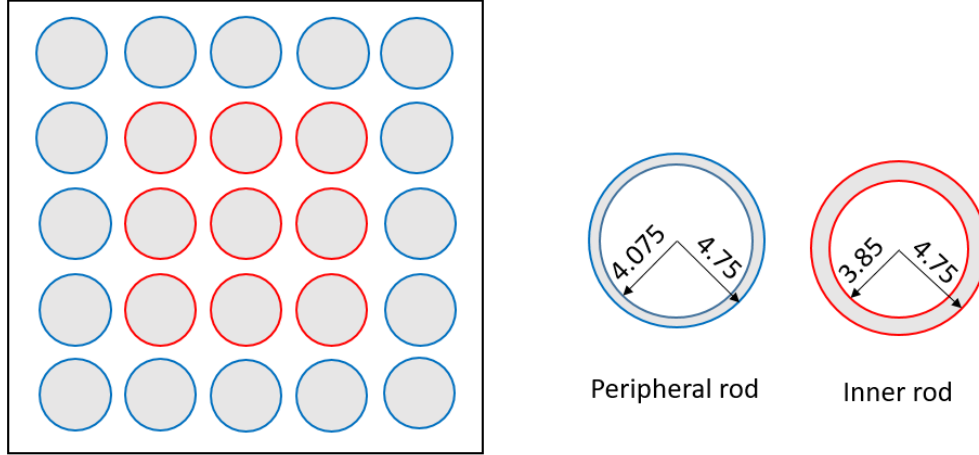


Figure 5-3: Rods configuration

MANIVEL hydraulic isothermal tests are a single-phase water flow consisting of (i) a pressure drop test series and (ii) a mean axial velocity test series. Both test run types were performed at steady-state flow rate and inlet temperature boundary conditions; the associated 2σ measurement uncertainties for these conditions are $\pm 0.5\%$ and $\pm 0.5K$, respectively.

Pressure drop test series

The SSG pressure drop test series consists of eight test runs at a temperature close to 17 and 30°C, a flow rate ranging from 20 to 65 m^3/h , and a resulting sub-channel Reynolds number Re_{SC} from 24,000 to 104,000 (see Table 5-1 in which run PD-7 is special because its operating conditions are almost the same as the mean axial velocity test run conditions). Table 5-1 also indicates that the errors of data acquisition were acceptable, with an impact on the sub-channel Reynolds number Re_{SC} less than 3%.

During each pressure drop test run, six pressure differences DPM1 to DPM6 were measured across four successive SSGs using eight pressure taps distributed along the test section on two perpendicular walls of the casing at 279 mm axial intervals (see Figures 5-2 and 5-4). The maximum 2σ measurement uncertainty for pressure drop was ± 0.3 mbar.

A brief consistency analysis of DPM1 to DPM6 measurement (which are related a priori to the same quantity) shows two main results:

- (i) A significant scatter in ΔP_i measurement for each run (with maximum differences in ΔP_i measurement results up to 9%), scatter however much smaller for DP-7 and DP-8 Runs with Reynolds number Re_{sc} close to 100,000;

(ii) A quasi-systematic relative behavior of ΔP_i results with respect to mean value (ΔP_{mean})

See Figure 5-4 which presents the DPMi measurement result-to-mean value ratios ($\Delta P_i / \Delta P_{mean}$) for the different runs – Reynolds number Re_{sc} in abscissa are representative of performed test runs.

Table 5-1: Pressure drop test run conditions (mean value and variation amplitude) [101]

Run name	Volumetric Flow Rate		Outlet Temperature		SC Reynolds Number	
	Mean (m^3/h)	Amplitude	Mean ($^{\circ}C$)	Amplitude	Mean (Re_{sc})	Amplitude
PD-1	20.22	1.4 %	17.6	0.11	23939	1.6%
PD-2	30.27	1.3 %	17.3	0.05	35500	1.5%
PD-3	39.57	1.3 %	17.1	0.04	46237	1.4%
PD-4	50.61	1.6 %	17.0	0.04	58967	1.7%
PD-5	60.51	2.0 %	17.0	0.02	70442	2.1%
PD-6	70.71	2.6 %	16.9	0.03	82244	2.7%
PD-7	60.76	0.9 %	30.4	0.30	96296	1.5%
PD-8	65.54	1.8 %	30.4	0.25	103974	2.4%

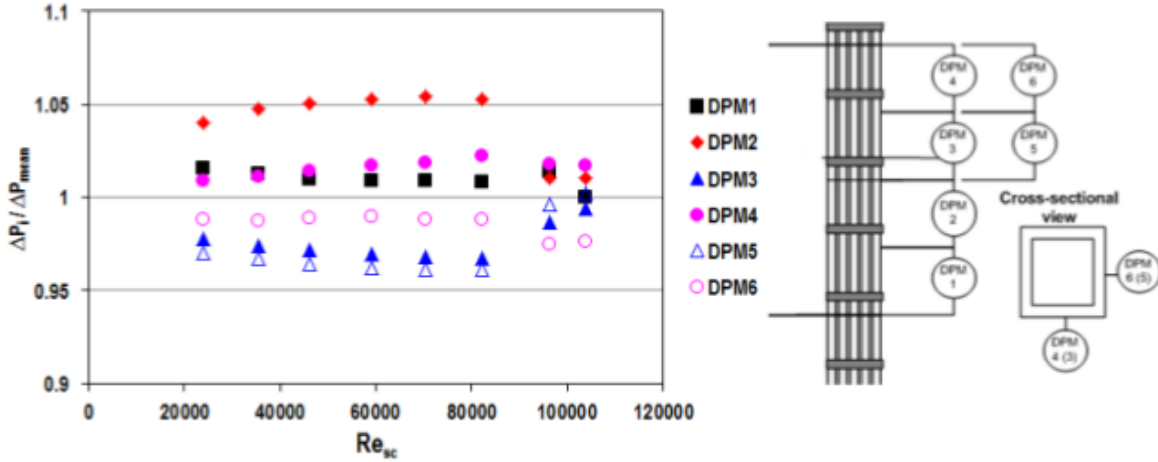


Figure 5-4: DPMi measurement-to-mean value ratios [101]

Mean axial velocity

2D axial velocity distributions were obtained by LDV scans over five cross-sections per span 2a and 2b (identified in Figure 5-2). Similar flow rate, inlet temperature and outlet pressure results in a sub-channel Reynolds number (Re_{sc}) close to 96,000. The test run conditions are provided in Table 5-2, along with their standard deviation over the measurement duration of each run.

The LDV-scanned cross-section elevations are provided in Table 5-3. They were chosen to get a sufficiently refined evolution of the axial flow field along the grid wake. The reference LDV

ellipsoidal measurement mesh in each cross-section is given in Figure 5-5 and is composed of 1908 locations. Each plane scan was performed in two sets of 954 points each, respectively obtained along the blue x and green y directions, so that in theory, nine points were measured twice at every sub-channel center region.

The LDV ellipsoidal measurement volume was 0.6 mm long, 0.07 mm wide and 0.07 mm high; its accurate location was achieved by refined geometric calibration of the coordinate system of the LDV probe positioning system with respect to the bundle casing. As a result, the (maximal) positioning error is 0.2 mm in the transverse x and y directions, and 0.5 mm in axial z direction.

Every velocity measurement corresponded to the acquisition of 1024 validated Doppler bursts, or a maximum acquisition time of 30 seconds, which was a good compromise between measurement quality and the duration of the test runs. Additionally, a minimum of 300 bursts was specified to validate an axial velocity measurement; such a threshold was defined by looking at the mean velocity convergence. Most rejected data points were located in the peripheral sub-channel with such a criterion. The 2σ uncertainty estimate for the local axial velocity measurement is $\pm 1.5\%$.

Table 5-2: MANIVEL LDV test run conditions [101]

Run name	Grid span	Duration (hr)	Volumetric flow rate, Q (m^3/h)	Temperature, T_{in} ($^{\circ}C$)	Pressure, P_{out} (bar)
V_Z035_Z050	2a	19.5	60.68 ± 0.098	30.4 ± 0.14	1.15
B_Z035_Z050	2a	15.2	60.28 ± 0.114	30.5 ± 0.16	1.44
V_Z100_Z160	2a	16.9	60.68 ± 0.096	30.4 ± 0.17	1.14
B_Z100_Z160	2a	11.0	60.61 ± 0.09	30.8 ± 0.36	1.38
V_Z235	2a	7.9	60.7 ± 0.079	30.5 ± 0.11	1.14
B_Z235	2a	6.5	60.66 ± 0.124	30.2 ± 0.2	1.13
V_Z304_Z329	2b	17.6	60.72 ± 0.089	30.4 ± 0.06	1.24
B_Z304_Z329	2b	11.3	60.77 ± 0.080	30.4 ± 0.06	1.13
V_Z379_Z439	2b	12.5	60.76 ± 0.079	30.4 ± 0.05	1.17
V_Z379_Z439	2b	10.4	60.74 ± 0.076	30.4 ± 0.06	1.12
V_Z514	2b	6.5	60.71 ± 0.080	30.3 ± 0.08	1.12
B_Z514	2b	5.8	60.67 ± 0.075	30.5 ± 0.05	1.11

Table 5-3: Axial elevation of LDV-scanned cross-sections in Spans 2a and 2b [101]

Grid span ID	Distance from upstream grid (mm)				
2a and 2b	25(35)	50	100	160	235

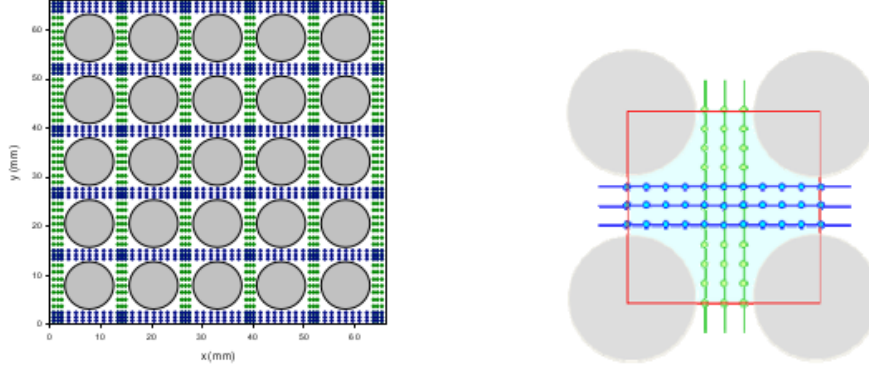


Figure 5-5: LDV target measurement mesh, with a zoom over a typical sub-channel [101]

5.1.3 Analysis of experiment

Definition of one-span pressure loss coefficient

Here, the McAdams correlation [102] is used to define the reference grid span fraction pressure loss (ΔP_{BR})

$$f_{MCA} = 0.184 Re_{D_h}^{-0.2} \quad (5.1)$$

where Re_{D_h} is the Reynolds number based on the mean cross-sectional velocity V_0 and the hydraulic diameter D_h accounting for the total test section wetted perimeter ($D_h = 10.28\text{mm}$ for the test sections). Thus, the one-span friction related pressure loss coefficient (K_{BR}) can be expressed as

$$K_{BR} \equiv \frac{\Delta P_{BR}}{P_{dyn}} = \frac{f_{MCA} H}{D_h} = 0.184 Re_{D_h}^{-0.2} \frac{H}{D_h} \quad (5.2)$$

where H is the one-span length (0.279 m) and the dynamic pressure $P_{dyn} = \frac{1}{2} \rho V_0^2$ with ρ the fluid density.

On the other hand, the one-span grid-related pressure loss coefficient (K_{SSG}), which is defined as

$$K_{SSG} \equiv \frac{\Delta P_{SSG}}{P_{dyn}} \quad (5.3)$$

can be estimated for isothermal MANIVEL experiment conditions using the extrapolation of one-span grid-related pressure loss coefficient based on the total grid span pressure (ΔP_{1sp}) data measured in the MANIVEL pressure drop tests. Table 5-4 presents the related Reynolds numbers and corresponding one-span pressure loss coefficients for each test (Re_{sc} is the Reynolds number based on the typical sub-channel hydraulic diameter $D_{h,sc} = 11.778\text{mm}$).

Table 5-4: One-span pressure loss coefficients based on the MANIVEL pressure drop tests

Run name	Re_{sc}	Re_{D_h}	$\Delta P_{1sp}(kPa)^*$	K_{1sp}^*	f_{McA}	K_{BR}	$K_{SSG} = K_{1sp} - K_{BR}$
PD-1	23939	20895	2895 \pm 1	1.2396	0.025169	0.68307	0.55656
PD-2	35500	30986	6005 \pm 2	1.1473	0.023253	0.63107	0.51621
PD-3	46237	40358	9745 \pm 3	1.0895	0.022063	0.59876	0.49072
PD-4	58967	51470	15213 \pm 5	1.0397	0.021014	0.57029	0.46942
PD-5	70442	61486	21007 \pm 7	1.0043	0.020276	0.55027	0.45403
PD-6	82244	71787	27907 \pm 10	0.9770	0.019664	0.53367	0.44334
PD-7	96296	84053	19998 \pm 3	0.9513	0.019047	0.51693	0.43441

* Measured values

The resulting regression-fit equation based on K_{SSG} values for PD-1 to PD-7 tests is

$$K_{SSG} = 3.3424Re_{D_h}^{-0.181}(\text{with } R^2 = 0.9975) \quad (5.4)$$

The reference one-span pressure loss coefficients for the upper four spans in isothermal experiment [based on Eqs.(5.2) and (5.4)] are presented in Table 5-5. The total pressure loss coefficient ($K_{BR} + K_{SSG}$) is the value directly measured in the experiment (see the PD-7 result in Table 5-4).

Table 5-5: Reference pressure loss coefficients for isothermal experiment

K_{BR}	K_{SSG}
0.517	0.434

Evolution of mean axial velocity profiles

Velocities at several axial locations over two spans (Spans 2a and 2b) were compared, but it seemed to be difficult for direct comparison between simulation results and all measured data. Thus, the mean axial velocities along Line 1 parallel to the x axis [see Figure 5-6 (a)] were compared between two cases.

It's obvious that simulation results show lateral symmetry of the flow while there are some discrepancies in the symmetry for measured data especially in regions near downstream of the support grid. In order to minimize the influence of measurement error, measurements were separately averaged at symmetrical locations for (i) Line 1 and 2, (ii) Line 3 and 4 [see Figure 5-6 (a)]. Values at each axial position except $z - z_G = 25$ mm and 35 mm were averaged for span 2a and 2b [Figure 5-6 (b)].

Figure 5-7 shows the average profiles of the measured mean axial velocity. Here, upper and lower values of the error bars indicate the maximum and minimum of measured values, respectively.

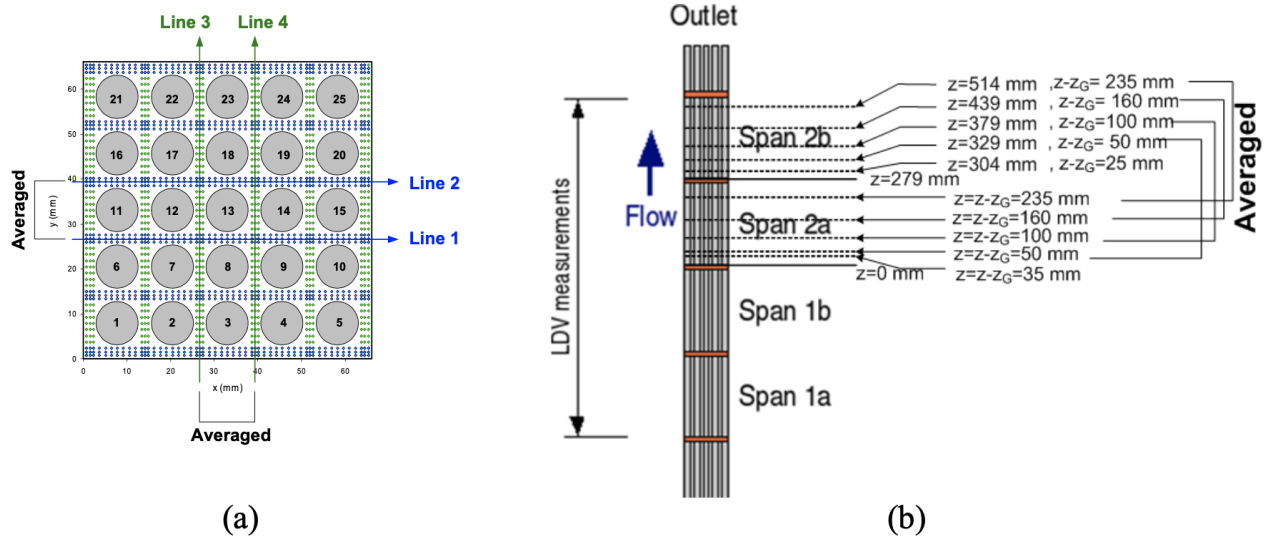


Figure 5-6: Averaging measured values in (a) lateral positions and (b) axial positions

Hollows were observed at regions close to spacer grids, while for regions far away from spacer grids, velocity profiles are pretty harmonic.

Stand-alone simulations are performed separately with corresponding SC code and CFD code in order to have reference results in both simulation types. At the moment, it is better to start with cases where there is not transverse flow within the rod bundles. Boundary conditions are coherent with experimental ones, axial velocity and pressure drop results are compared to the reference data. Besides, the literature investigation about CFD computation of Benchmark experiment is realized to help us choose appropriate turbulence model and wall treatment. After that, same parameters could be set in the coupled work to obtain reliable results in both sides.

5.2 Simulation with SC code: average modeling

The code, FLICA4, is a code of thermal-hydraulic dedicated essentially to two-phase flow within nuclear reactor core for permanent or transient regimes in the normal, incidental or accidental situation. This is a code averaged: it means that it solves the evolution of the mean value of the velocity field, average corresponds theoretically to an infinite number of experiments (averaged statistical). Here, it's used to simulate the benchmark MANIVEL experiment.

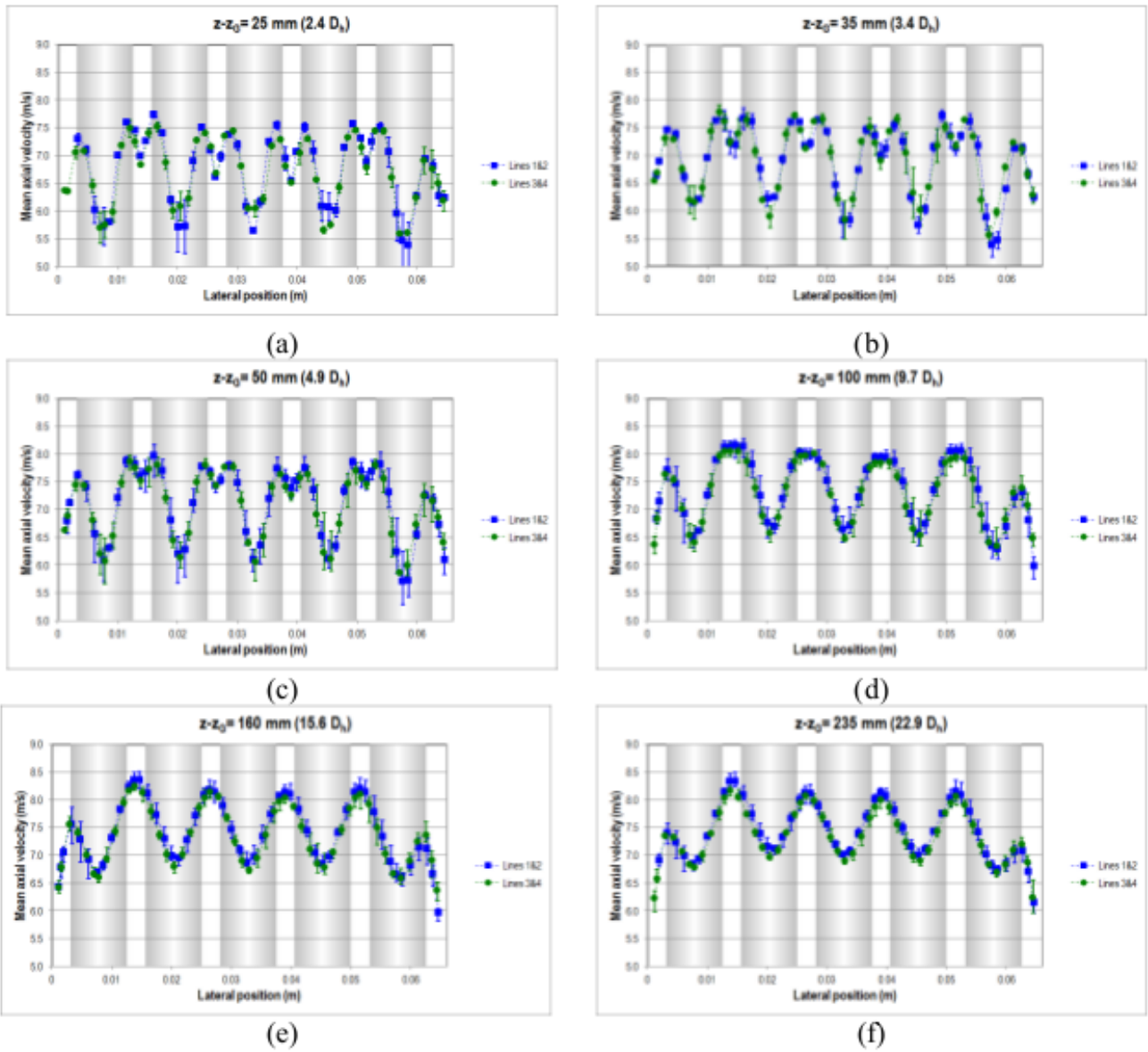


Figure 5-7: Averaged experimental mean axial velocity data along probe lines at different elevations

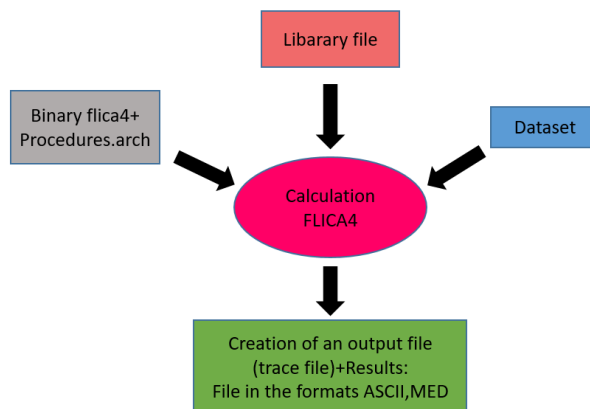


Figure 5-8: General flowchart of FLICA4 calculation

The code uses libraries contained thermodynamics functions of the fluid as shown in Figure 5-8; besides, physical models based on experimental data are applied, as such, the sub-channel code can provide reliable solutions at a sub-channel scale.

5.2.1 Description of mesh and parametric parameters

Since the bundle casing is totally symmetric, in order to reduce simulation time and save computational resources, one eighth geometry of the bundle in the view of cross section is used to launch the simulation and it's located in the south-west of the center point (see Figure 5-9). For the axial configuration, each span is divided into segments with length of 0.01 m, 0.011 m and 0.008 m; the segment of 0.008 mm is with simple support grid, therefore, for the part without SSG, there are 26 segments of 0.01 m and one segment of 0.011 m. Each span has the same mesh configuration and it begins with SSG at the bottom. The total height of the bundle is 5 m, so there is 17 spans plus 25 segments of 0.01 m and one segment of 0.007 m without SSG.

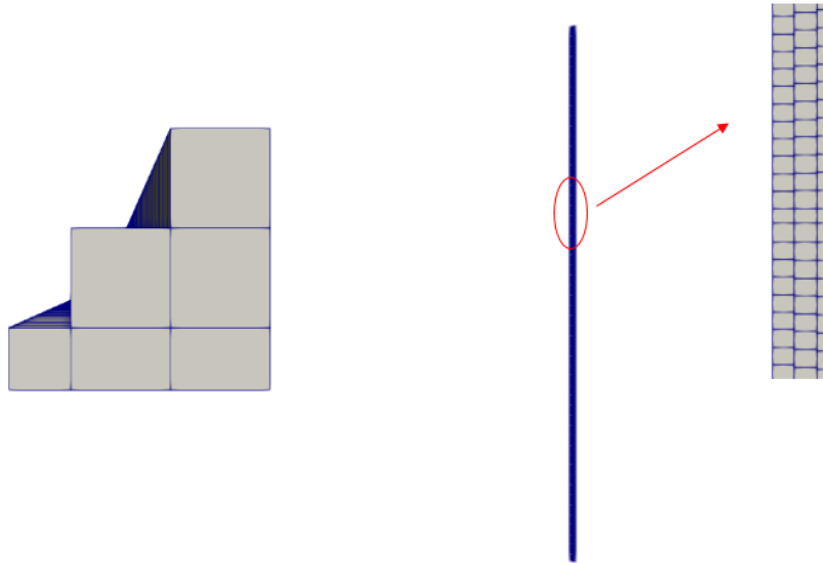


Figure 5-9: Mesh configuration used in FLICA4: cross section(left) and axial view (right)

For the parameters set during the simulation, the library file chose for water data is that in low pressure; models used are boiling, re-condensation, strong wall correction and turbulence. According to test conditions used in experience, table of water physical properties is applied to set the boundary conditions for the simulation using FLICA4 as Table 5-6.

Table 5-6: Boundary conditions in FLICA4

Parameter (unit)	Value
Outlet pressure (pa)	1.2E5
Inlet gas concentration	0.
Inlet liquid mass flow rate ($kg/m^2/s$)	6353.1
Inlet gas mass flow rate ($kg/m^2/s$)	0.
Inlet liquid enthalpy (J/kg)	127.3E3
Inlet gas enthalpy (J/kg)	2556.3E3

5.2.2 Results

Table 5-7 shows comparisons of calculation results obtained by FLICA4 and experimental results. Here, the averaged axial velocity is obtained in the axial position: $z - z_G = 35mm$ (see Fig 5-2), the pressure loss per span was obtained from averaging the pressure losses over four spans (see Fig 5-2). Errors between two cases are quite acceptable, this sub-channel code is proved, as a result, to be able to predict the overall physical properties of flow within the rod bundle while it cannot provide detail results in microscopic level and it is impossible to capture some important physical phenomenons.

Table 5-7: Comparison of calculation/experiment

	Experimental	Numerical	Relative error
Input temperature ($^{\circ}C$)	30.40	30.32	0.26%
Output pressure (bar)	~ 1.20	1.20	0.08%
Averaged axial velocity (m/s)	~ 6.70	6.41	4.39%
Grid span pressure loss (mbar)	200	218	9.00%

Axial mean velocity distribution is presented in Figure 5-10. It can be concluded that flow velocity in center region is higher than that in the periphery which is coherent with experimental data.

5.3 CFD Simulation : influence of inlet turbulent flow

This section is an extension of a conference proceeding [103] which presents the CFD modeling of the adiabatic rod bundle test (MANIVEL) with a Simple Support Grid (SSG) at a Reynolds number of 100 000. Calculations are carried out on grid using a one-block fully hexahedral mesh. To reduce the computational power requirements, the computational domain is limited to one span with one SSG. The inlet is a fully developed turbulent flow obtained using periodic computations that are applied on two different domains: an inlet box and a span box. The mean axial velocity distribution at different elevations and pressure drop are compared with measurements.

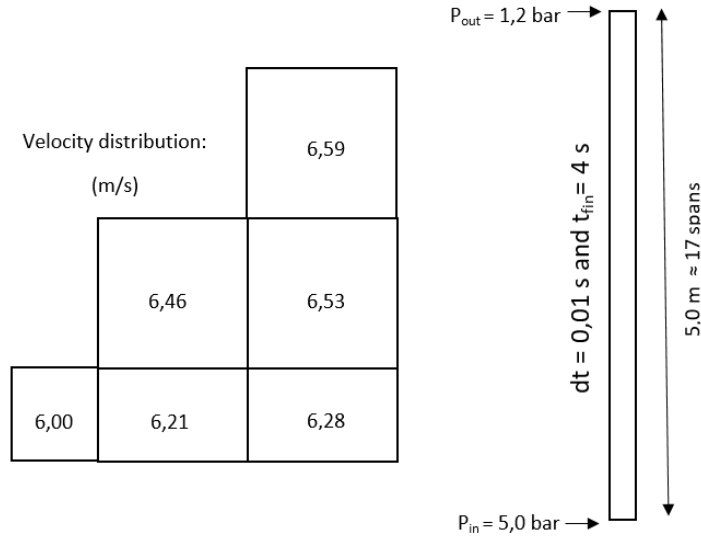


Figure 5-10: Axial mean velocities distribution

5.3.1 Introduction

The nuclear safety analysis of thermal-hydraulic situations encountered during normal operating conditions or accidents, traditionally, used system codes and sub-channel analysis codes which combine numerous empirical correlations based on simple governing equations to evaluate the synthetic effect with a relative low accuracy. Simulations are performed with large control volume (components or subchannels) with validation based on global variables (pressure, temperature or void fraction) [104]. Classically, for reactor cores, two levels of applications can be applied which are respectively the fuel assembly and the subchannel level. The subchannel level is mostly used to assess the Critical Heat Flux (CHF) [105] margin, using local parameters such as mass flow and quality. These 3D tools have several number of restrictions related to nodalization, field equations and other aspects of physical modeling. For particular situation, in a limited region of the system, a detailed understanding of the flow could be required with the help of a 3D Reynolds Averaged Navier-Stokes (RANS) code which may be applied for the detailed analysis [106].

The CHF could be considered as the key thermal performance parameter for Pressurized Water Reactor (PWR) fuel. In recent years, assessment of crud-related risks, such as Crud-Induced Power Shift (CIPS) [107] and Crud-Induced Localized Corrosion (CILC) [108], observed in upper spans of high-duty PWR cores, have been important issues in terms of safety and fuel performance which requires local heat transfer coefficient around each rod [109].

The subchannel codes cannot predict such local heat transfer information and it is difficult to obtain effectively such data with experiments which are expensive even for small test facilities. The computational fluid dynamics (CFD) codes can extract the local information more easily in a large computational domain and cost less [110]. Two-phase flow is much more complex to measure,

model, and understand than single-phase flow. This is especially true in nuclear fuel assemblies which contain complex structures in the flow domain. It is logical to start with CFD models of single-phase conditions which are easier and less costly [111].

Heat transfer plays an important role in thermal-hydraulic analyses of fuel rod bundle, but similarly, it is much more complex to model and understand than adiabatic conditions. Firstly, it is logical to start with adiabatic hydraulic simulations, after that, influence of temperature could be taken into account to carry out thermal-hydraulic simulations which are more pertinent to operational conditions in nuclear reactor core.

In CFD analysis, the domain is subdivided into a sufficiently large number of control volumes in order to obtain an adequate resolution of the flow geometry and the flow phenomena in the domain. Some recommendations are given concerning the type of element, especially the use of hexahedral elements which are the most efficient from the numerical point of view, the mesh quality with the use of a finer and more regular mesh in regions with high gradients or large changes and the use of wall functions which compute the wall shear stress and wall heat fluxes based on linear/logarithmic velocity and temperature profiles in RANS turbulence models.

For simplicity, the benchmark experiment MANIVEL [112] which considers only the type of Simple Support Grid (SSG) rod bundle is selected to be a reference. Considering the smallest geometrical element's size of a grid (less than 0.5 mm) included in a fuel rod bundle with 4 m of height, total cells number for a mesh fine enough of a span is more than 10 million, while there are around 14 spans for the complete rod bundle, thus the simulation with a full axial domain using CFD codes is too expensive and not accurate enough.

To reduce the computational power requirements, the computational domain could be limited to one span and inlet boundary conditions could be defined as a fully developed velocity profile obtained by a separate calculation with a periodic boundary condition, named in the following periodic computation. It could be expected that the flow passing over more than 10 spans is to be fully developed in each span. Instead of modeling a full-length rod bundle, the one span approach cited previously has a significant gain in time, with an order of magnitude faster than the former.

The object of periodic computations is to obtain a turbulent flow in a well-developed region, if the distance between two spans is long enough, the influence of the grid can be negligible far downstream the grid. In this case, the grid can be neglected and an inlet box [18] (rod bundle without grid with a height of few hydraulic diameters based on sub-channel) is used to run periodic computations. Since it is difficult to judge at which distance can the influence of grid eliminate, here, two computational domains are considered: one is the inlet box cited previously, the other is the total span with grid [101], named in the following span box.

This section presents the influence of inlet turbulent flow generated by periodic computations (inlet box or span box) on the pressure drop and axial velocity distribution predictions by RANS turbulence models used in NEPTUNE_CFD to model single-phase, isothermal conditions in PWR fuel assemblies. Description of the benchmark experiment and pertinent experimental data are provided in previous section. Results of test sections with realistic flow conditions generated by periodic computations applied on two different domains are compared with measurements and their difference are analyzed.

5.3.2 Mesh generation

The way to create the mesh is a key factor affecting the accuracy of CFD results. The mesh must match the requirement of turbulence model used and near-wall treatments. Furthermore, mesh quality will affect computational stability and convergence time. The geometry of rod bundle with and without grid and meshes associated has been generated through the platform SALOME [113]. Meshes are all based on the grid using a one-block fully hexahedral mesh, as depicted in Figure 5-11. The total cells number for meshes used for inlet box and span box are respectively around 2 million and 9 million.

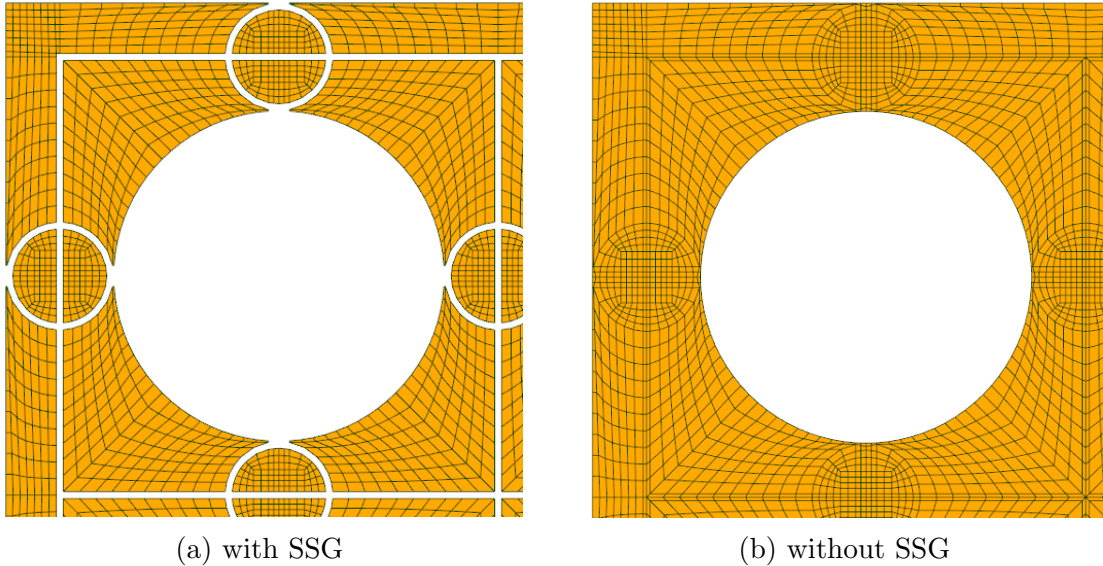


Figure 5-11: Transverse section of mesh used in simulation

Considering the limited computational resources, only the geometry of one span is generated. Since the flow in the disturbed tube bundles (the part downstream of spacer grid) [18] is more interesting in our present work, the length of undisturbed tube bundles (the part upstream of spacer grid) has been reduced to 20 mm, which corresponds to the distance between inlet and SSG, resulting in a length of 251 mm for the disturbed tube bundles region (we recall that the height of SSG is

8 mm). The mesh is generated by extruding in the streamwise direction a two-dimensional radial mesh. The inlet box is a periodic tube bundle without spacer grid, and its axial length is six D_h . The radial mesh refinement for both boxes and test section is the same and their mesh refinement in streamwise direction is equal to 1 mm.

5.3.3 RANS turbulence models

NEPTUNE_CFD [91] is a general multi-fluid Navier-Stokes code with the Eulerian approach. It is based on a finite volume discretization and allows the use of various mesh types which may be hybrid. The mass balance equation is written :

$$\frac{\partial}{\partial t}(\alpha_k \rho_k) + \frac{\partial}{\partial x_i}(\alpha_k \rho_k U_{k,i}) = 0 \quad (5.5)$$

with α_k , ρ_k , U_k , the volume fraction, the density and the mean velocity of phase k . The momentum balance equation in semi-conservative form is written :

$$\begin{aligned} \frac{\partial}{\partial t}(\alpha_k \rho_k U_{k,i}) + \frac{\partial}{\partial x_j}(\alpha_k \rho_k U_{k,i} U_{k,j}) = \\ \frac{\partial}{\partial x_j}(\alpha_k \tau_{k,ij} + \Sigma_{k,ij}^{Re}) - \alpha_k \frac{\partial P}{\partial x_i} + \alpha_k \rho_k g_i + \alpha_k S_k \end{aligned} \quad (5.6)$$

with :

- P the mean pressure;
- g_i the gravity;
- $\tau_{k,ij} = \mu_k \left(\frac{\partial U_i}{\partial x_j} + \frac{\partial U_j}{\partial x_i} - \frac{2}{3} \nabla(U) \delta_{ij} \right)$ the viscous stress tensor;
- μ_k the dynamic viscosity;
- $\Sigma_{k,ij}^{Re} = -\alpha_k \rho_k \langle U'_{k,i} U'_{k,j} \rangle_k$, the turbulent stress tensor;
- $S_k = S_k(\alpha_l, U_l, P)$, with $l = 1, \dots, n_{phases}$, external source terms such as head losses.

The energy balance equation is also considered by the code, but since the present work concerns hydraulic simulations in isothermal conditions, no more details are presented here.

To solve conservation equations on mass, momentum and energy, the "alpha-pressure-energy cycle" is used, which ensures conservation of mass and energy. The algorithm is compressible, which allows variation of density (in the function of pressure and enthalpy) during a time step. The variables are located at the center of the cells. The "alpha-pressure-energy cycle" algorithm is an algorithm with a pressure-based solver at first order in time. This means that the algorithm does not solve directly Euler equations in their conservative form, but tries to reach this conservation

in an iterative manner. This iterative procedure allows to couple velocity, pressure and enthalpy to reach consistency and to assure an implicit resolution.

5.3.4 Boundary conditions

In order to respect the real experimental setup, the boundary conditions used in the numerical simulations are consistent with experiments. The simulation of total rod bundles is difficult due to actual limited computational resources. Considering that the flow pattern has a periodically repeating nature due to the periodicity of the geometry such as the successive spans along the rod bundle, thus periodic computations can be used to generate a fully developed flow for one span [114]. The periodic condition adds source terms in the momentum equation to conserve the total momentum desired within the computation domain [115].

The imposed momentum source term S is similar to the expression of source term used in LES simulations coupled with average RANS component through a time coupling constant [116]. S is the local velocity drop rate which is assumed to be mean velocity drop divided by time step. Since this flow is incompressible, so the water density is constant when considering momentum terms, density terms can be neglected. Besides, compared to sectional velocities, axial velocities play a dominant role in momentum terms. Consequently, we have the final form of S :

$$S = \frac{V_0 \times vol_t - \sum_{i=1}^{ncel} vol_i \times V_{l,i}}{vol_t \times \Delta t} \quad (5.7)$$

where V_0 is the cross-sectional-averaged velocity; vol_t is the total volume of the span; $ncel$ is the total number of cells; vol_i and $V_{l,i}$ are local volume and axial velocity for each cell; Δt is the time step.

The application of periodic conditions has been proved to conserve well the mass balance during the simulation while it eliminates pressure difference between two borders of computational domain. In order to simulate the pressure drop and turbulent flow at the same time, classical simulation of test section (one span) is realized with inlet boundary condition defining as a fully developed flow generated by periodic computations. The periodic computations are based on the same momentum source terms which assure a constant mean axial mass flow rate with periodic conditions in axial direction and realistic flow defined at the beginning of computations.

There are two ways to run periodic computations: one with inlet box, a so-called inlet box containing only a raw tube bundle (as presented in Figure 5-12), the other with span box, a so-called span box, adding the modeling of a grid to the bundle (as presented in Figure 5-13). The height of inlet box is 60 mm, and the mesh of span box is the same as that of test section. Both boxes and test sections have the same mesh quality (both radial and axial). Both velocity distribution and fluctua-

tions are established in the inlet box after about 50 flow turn over cycles and in the test section after about 10 flow through domain (the same for span box). In order to distinguish simulation results of test section with different inlet turbulent flows, the classical test section simulation with inlet turbulent flow generated by periodic computations using span box is named as span test and that with inlet turbulent flow generated by periodic computations using inlet box is named as inlet test.

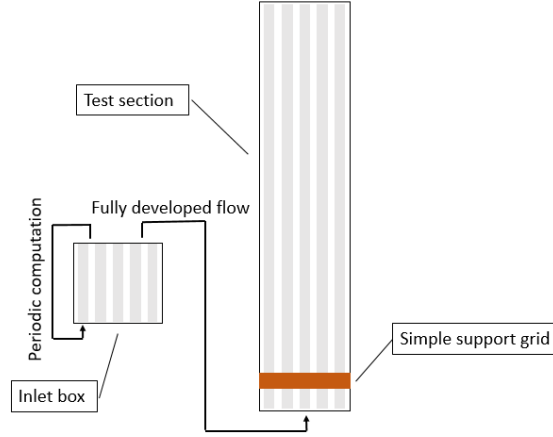


Figure 5-12: Generation of inlet turbulent flow using inlet box

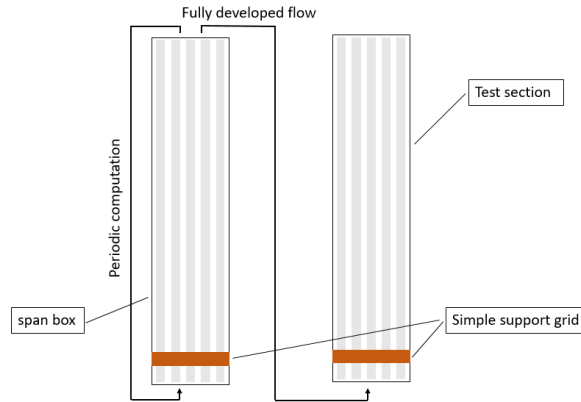


Figure 5-13: Generation of inlet turbulent flow using span box

For parameters set in NEPTUNE_CFD [117], standard $k - \varepsilon$ and $R_{ij} - \varepsilon$ SSG turbulence models have been tested separately. Material chose for simulation is water; Eulerian multiphase is used for flow model; walls with inlet/outlet are taken as boundary conditions in the simulation; local time step is set to be $\Delta t = 5 \times 10^{-5} s$.

Here, the classical logarithmic wall function is chose to describe the velocity profile of the turbulent flow close to the wall:

$$u^+ = \frac{1}{\kappa} \ln(y^+) + B \quad (5.8)$$

Normalized values of velocity u^+ and wall distance y^+ are defined as $u^+ = u_t/u_w$ and $y^+ = \rho_l u_w \Delta y / \mu_l$, where $u_w = \sqrt{\tau_w / \rho_l}$ is the friction velocity and τ_w is the wall shear stress. The variable u_t denotes the known velocity tangential to the wall and Δy denotes the absolute distance from the wall.

The resulting typical wall Y^+ during the simulation is around 50, which is in a reasonable interval and means that the wall treatment has been well performed. Test conditions of the experiment are used to define boundary conditions.

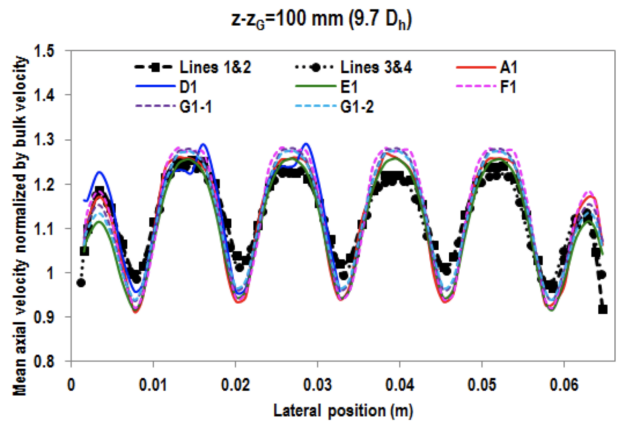
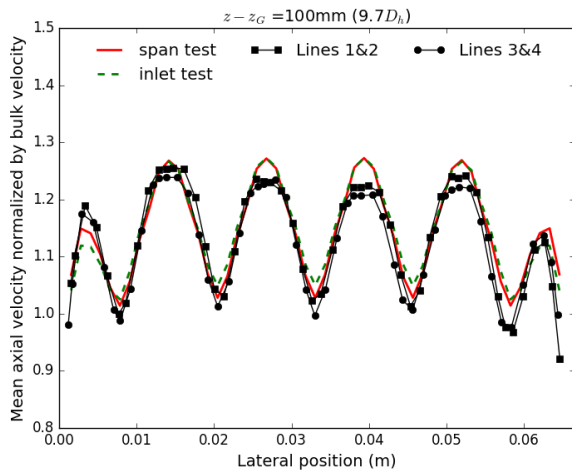
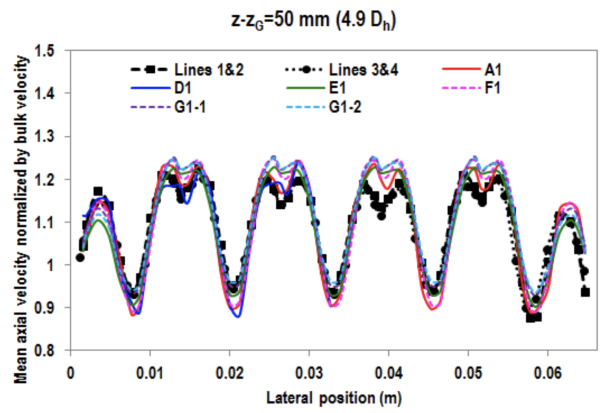
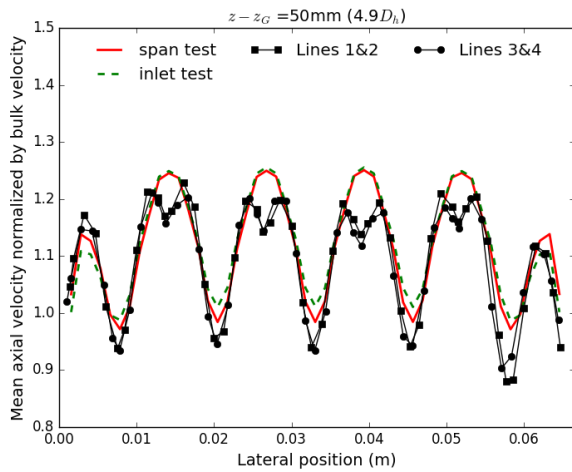
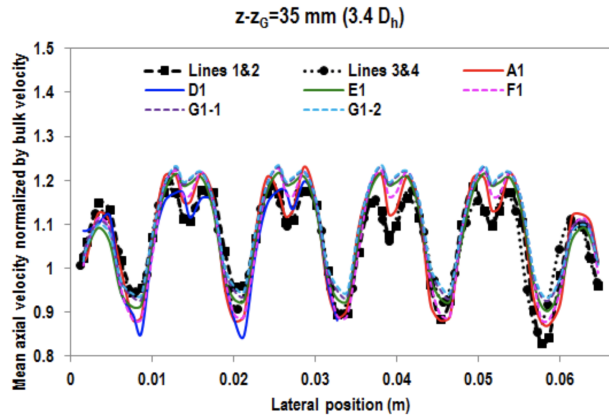
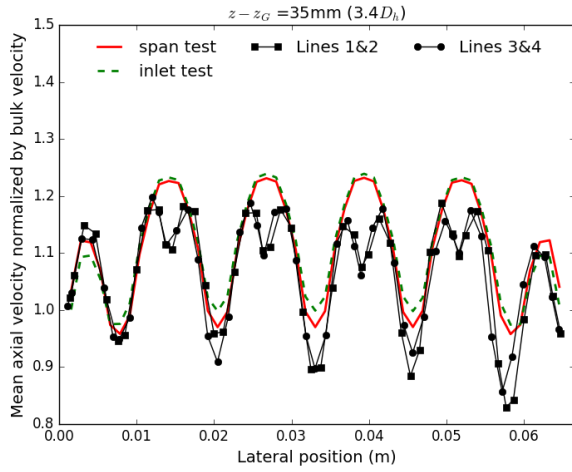
5.3.5 RANS model sensitivity study

Axial velocity

In benchmark experiment, velocities at several axial positions are measured over two spans (span 2a and span 2b), but it is difficult to obtain insight from direct comparison between CFD results of test section with all measured data. More frequently, we also compare directly mean axial velocity profiles along the laser probe scanning Line 1 parallel to the x axis which is more representative (see Figure 5-6 (a)). Due to measuring errors, some discrepancies in the symmetry are present in experimental data. In order to minimize these errors, measured data are averaged in symmetrical locations for (i) Line 1 and 2 and (ii) Line 3 and 4. At each axial location, we average values at the same position far from the spacer grid of span 2a and 2b (except for $z - z_G = 25$ mm and 35 mm). But since CFD results show highly lateral symmetry, only mean axial velocity profiles along x axis are presented hereafter, and discrepancies in simulation results between upper spans are neglected.

Figure 5-14 shows the comparison of the mean axial velocity profiles normalized by bulk velocity between simulation results and experimental data at several axial positions. For results of present work (left column), both velocity distributions of span test and inlet test show good agreement with measured ones far downstream the support grid. The discrepancies become more and more significant as distance from the grid decreases, there is not hollow observed in center region of each sub-channel probably due to the fact that the mesh density in this region is not sufficient to capture the turbulent flow. Besides, results of span test are more coherent with measured ones than that of inlet test.

Right column of Figure 5-14 presents simulation results obtained by participants of EPRI project with isotropic turbulence model. Three commercial CFD codes (ANSYS CFX, ANSYS Fluent, and STAR-CCM+), and one open-source code (Code_Saturne) were used as CFD solvers by participants. Various computational domains and corresponding boundary conditions were adopted in the simulation. For example, the full axial domain, computational domain of several spans and one-span domain are chose along with uniform velocity profile or periodic conditions, and so on.



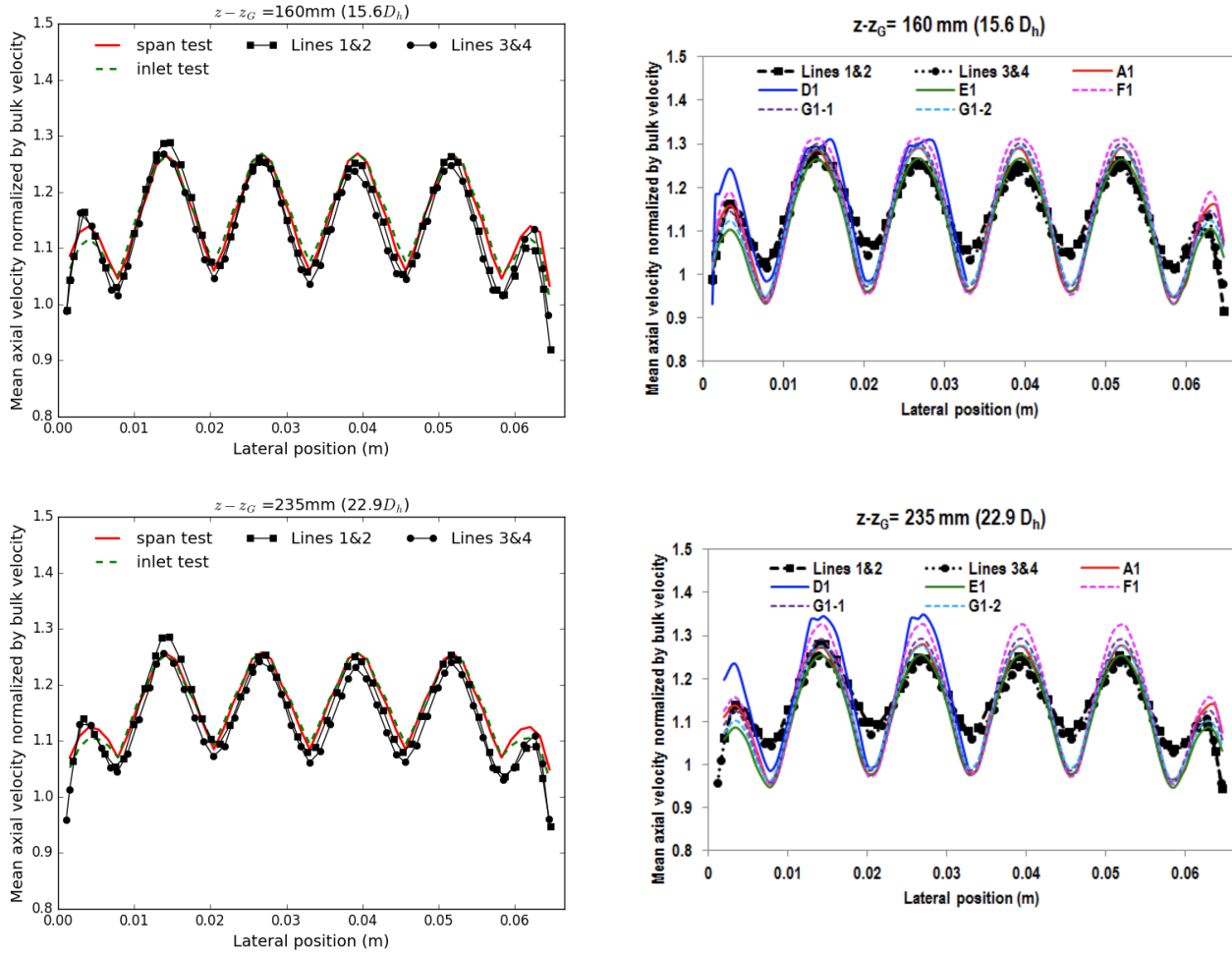


Figure 5-14: Comparison of the mean axial velocity normalized by bulk velocity for results of present work (left column) and that obtained by participants of EPRI project (right column): experimental data are indicated as "line 1&2" and "line 3&4" [101]

Different isotropic RANS turbulence models ($k - \varepsilon$ and $k - \omega$) are applied and two-velocity-scale wall function is mostly selected for the wall treatment. As for the mesh generation, most calculations adopted trimmed hexa mesh and cells number varies from 5,7 million to 32 million. For more details about methodologies used by different participants, see [101].

As a result, hollows were observed near downstream the spacer grid. While for results far downstream the simple grid, discrepancies in velocity amplitude increase as the distance from simple grid increases. In conclusion, calculations of project participants are more appropriate for flow in the disturbed tube while our case performed better in prediction of flow in the undisturbed tube, probably due to different models and mesh generations adopted in the simulation.

The next, for the span test, another turbulence model, the $k - \varepsilon$ SSG, is tested with the same mesh refinement, as depicted in Figure 5-15. Hollows are captured in regions close to the spacer

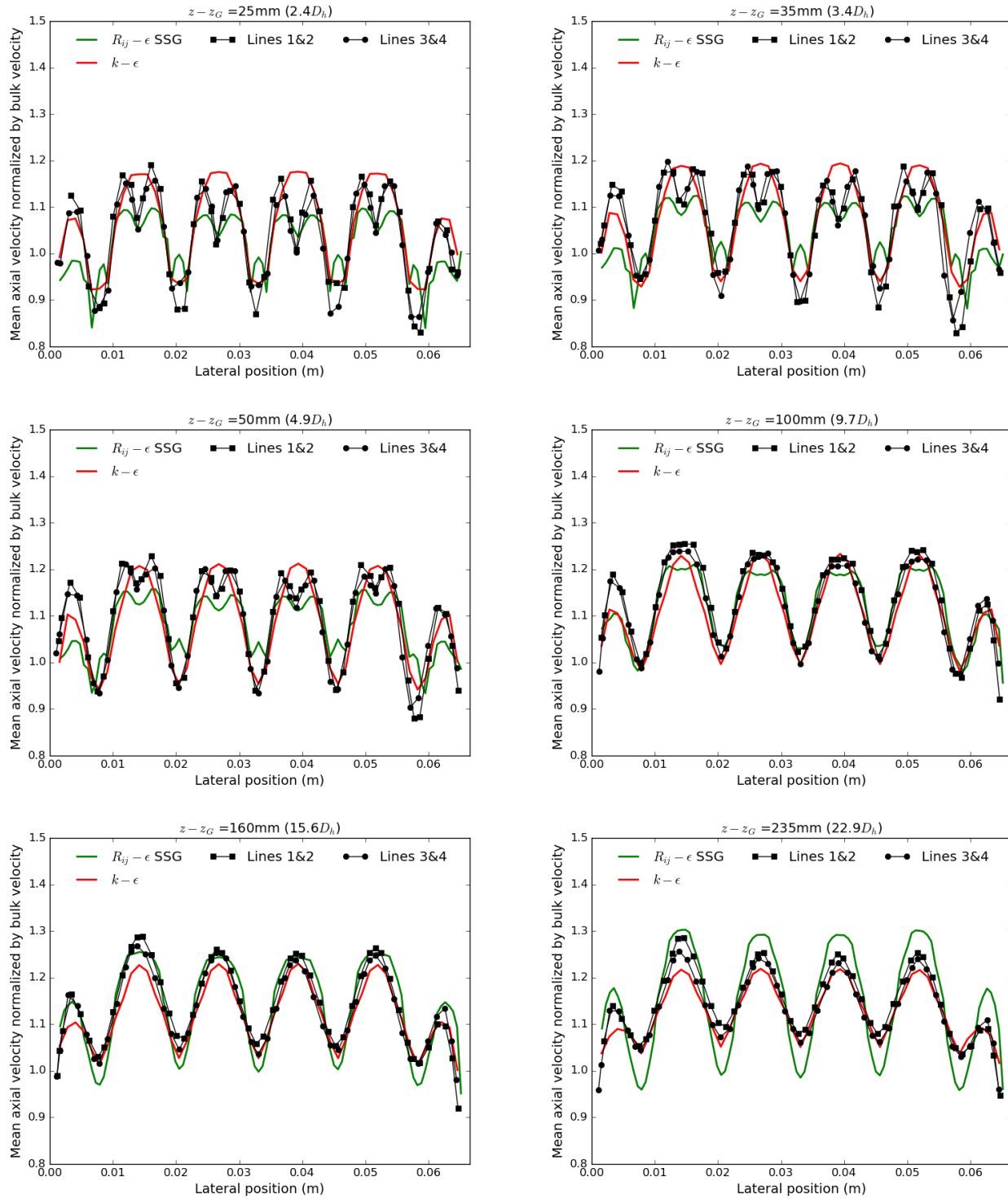


Figure 5-15: RANS model sensitivity study for span test: experimental data are indicated as "Lines 1&2" and "Lines 3&4"

grid while with lower amplitude compared to the case with $k - \varepsilon$ model. Meanwhile, the case with $k - \varepsilon$ SSG has higher amplitudes in regions far downstream the grid. It can be concluded that the current mesh is suitable for the $k - \varepsilon$ model, while finer mesh is required for the $k - \varepsilon$ SSG model to give better predictions. Despite the wrong amplitudes, $k - \varepsilon$ SSG model allows us to observe hollows in the central region of each sub-channel.

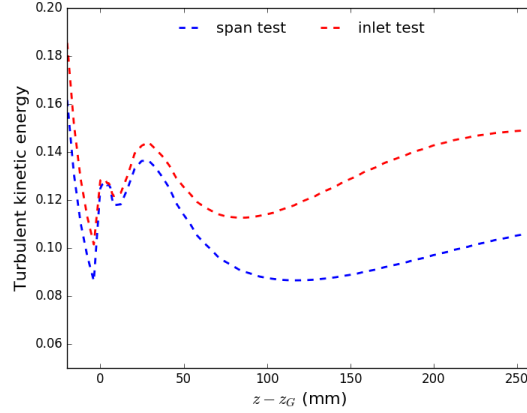


Figure 5-16: Turbulent kinetic energy variation along a grid span

Profiles of turbulent kinetic energy, k along the span between span test and inlet test are presented in Figure 5-16. Obviously, k values of inlet test are larger than that of span test all along the span. Normally, k decreases as elevation increases, but there is a dramatic increase of k at the entrance of the grid and a peak can be observed at around 40 mm away downstream the grid. Furthermore, the value of k has slightly increased far downstream the grid. It could be deduced that k values need to be high enough in a region to capture hollows.

Pressure drop

Figure 5-17 presents comparisons of pressure loss per span between CFD results and experimental ones. Calculation of span test shows good agreement while that of inlet test has an over-prediction of 8.5% compared to experimental data. More specific difference between two calculation results can be identified by comparing the pressure axial profile over a span as shown in Figure 5-18 where z_G is the elevation of spacer grid.

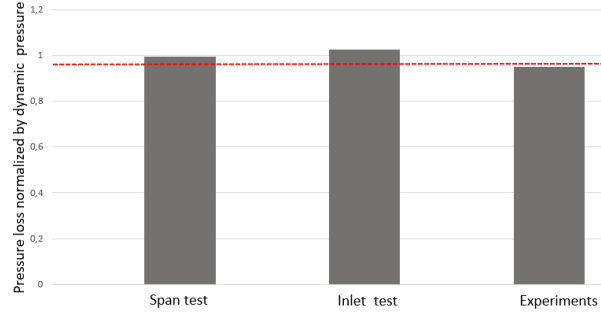


Figure 5-17: Comparison of pressure loss per span

For pressure axial variation over a span, pressure decreases linearly with the same slope upstream and downstream of the spacer grid. There are strong variations in two borders of SSG, but over the length of support grid, pressure decreases linearly with a different slope. Pressure drop obtained by inlet test is higher than that obtained by span test and slopes of pressure variation between two cases are different. We can conclude that different inlet turbulent flows have an influence on pressure axial variation profiles over the span.

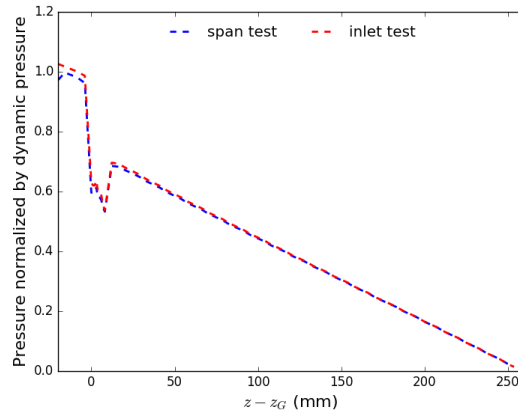


Figure 5-18: Pressure variation along a grid span

To analyse the one-span pressure loss coefficient, we assume that the reference grid span friction pressure loss (ΔP_{BR}) can be calculated using the McAdams correlation [101]

$$f_{MCA} = 0.184 Re_{D_h}^{-0.2} \quad (5.9)$$

where Re_{D_h} is the Reynolds number based on the mean cross-sectional velocity V_0 and the hydraulic diameter D_h accounting for the total test section wetted perimeter ($D_h = 10.28 \text{ mm}$ here). In our case, f_{MCA} is equal to 0.019047. Thus, the one-span friction related pressure loss coefficient (K_{BR}) can be expressed as [118]

$$K_{BR} \equiv \frac{\Delta P_{BR}}{P_{dyn}} = \frac{f_{MCA} H}{D_h} \quad (5.10)$$

where H is the one-span length (0.279 m) and the dynamic pressure $P_{dyn} = \frac{1}{2}\rho V_0^2$ with ρ the fluid density. On the other hand, the one-span grid-related pressure loss coefficient (K_{SSG}) can be expressed as

$$K_{SSG} \equiv \frac{\Delta P_{SSG}}{P_{dyn}} \quad (5.11)$$

Table 5-8: Comparison of pressure loss coefficients

	Exp.	Span test	Err.	Inlet test	Err.
K_{BR}	0.517	0.517	-	0.517	-
K_{SSG}	0.434	0.448	3.2 %	0.510	17.5 %

Table 5-8 shows that the grid-related pressure drop coefficients for both cases are overestimated, the span test has almost perfectly predicted the bare bundle pressure drop (around 3 % error), while the inlet test has much higher over-prediction with 17 % error.

5.3.6 Mesh sensitivity study with the $R_{ij} - \varepsilon$ SSG model

In order to capture hollows at the center region of each sub-channel, computational domains have been refined, especially for regions close to spacer grids, as shown in Figure 5-19. The resulting mesh sizes for inlet box and span box are respectively around 4 million and 14 million. Besides, another turbulence model $R_{ij} - \varepsilon$ SSG is applied according to literature on the related simulations and with respect to the results obtained in our simulations performed with a coarser mesh. No more detail but only key points are analyzed here.

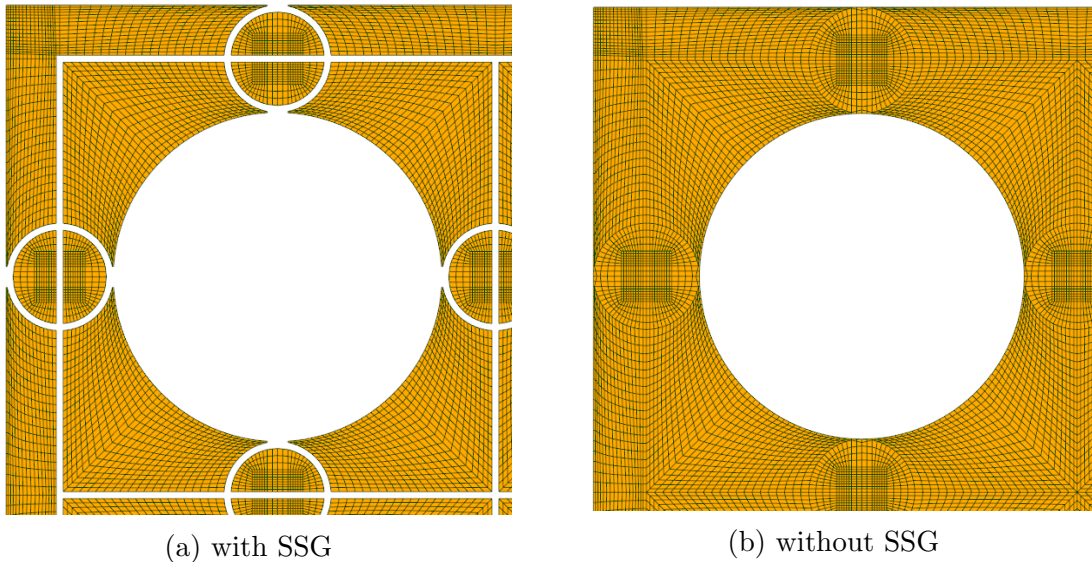
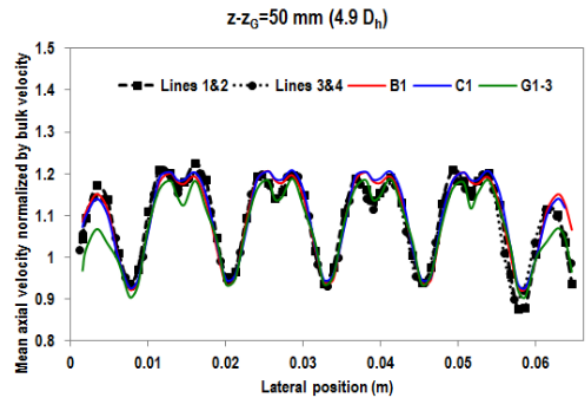
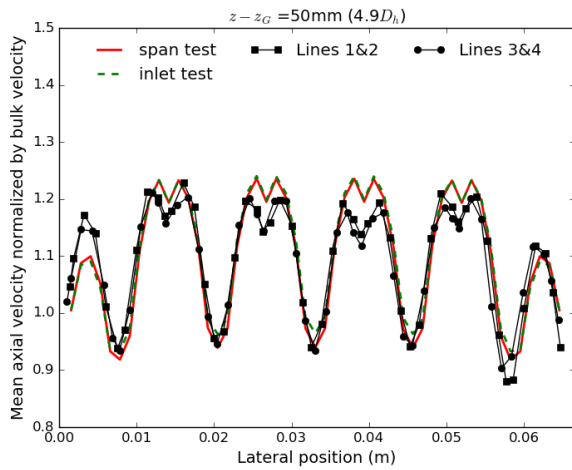
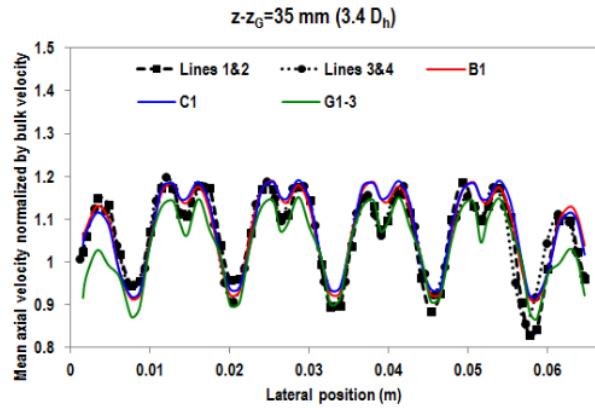
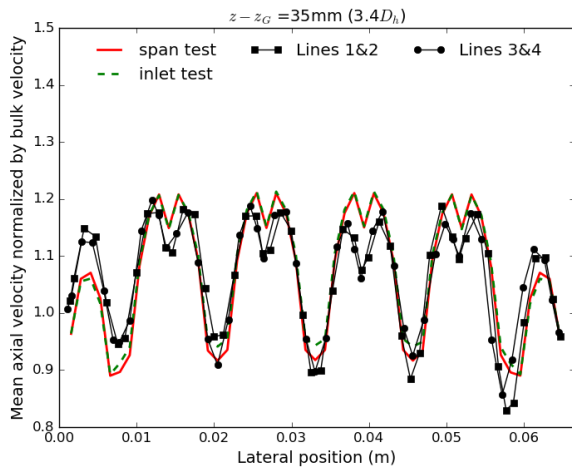


Figure 5-19: Transverse section of refined mesh used in simulation

Axial velocity

Lateral velocity profiles at different elevations, as depicted in Figure 5-20, show better agreement with experimental data in the region close to spacer grids than results with $k - \varepsilon$ model. In the region far downstream the spacer grid, discrepancies become more significant compared to previous case. Hollows are observed, difference between inlet test and span test is not important.

Right column of Figure 5-20 presents simulation results obtained by participants of EPRI project with an-isotropic turbulence model. One commercial code (STAR-CCM+) and one open-source code (Code_Saturne) were used as CFD solvers by participants. One can refer to previous section for more details about computational domains and wall treatments, etc. Current results have relatively higher amplitudes compared to that of other participants, while the discrepancy is neglected. It can be concluded that the an-isotropic turbulence model is more adapted to capture hollows in center regions of sub-channels.



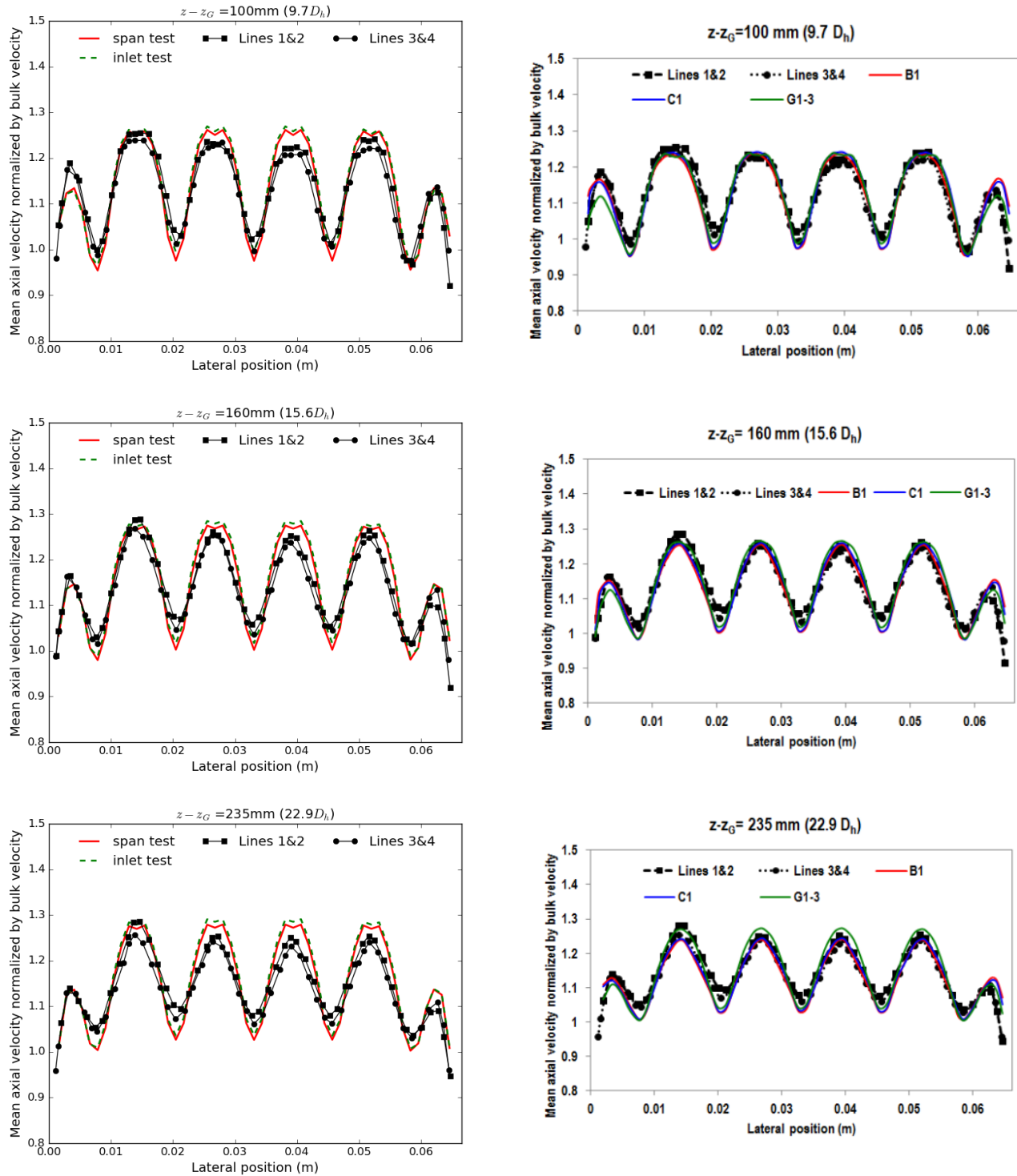


Figure 5-20: Comparison of the mean axial velocity normalized by bulk velocity for $R_{ij} - \epsilon$ SSG model (left column) and that obtained by participants of EPRi project (right column)

Pressure drop

For pressure drop per span, inlet test and span test give similar results, as depicted in Figure 5-21, both are under-estimated by around 15%. The current results are coherent with that of other

EPRI project participants. Compared to a general under-estimation of 25%, our results give better prediction.

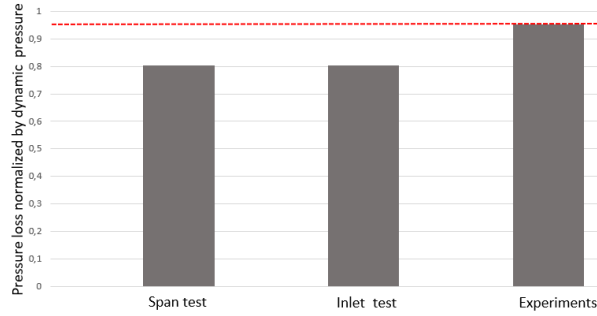


Figure 5-21: Comparison of pressure loss per span with $R_{ij} - \varepsilon$ SSG model

Figure 5-22 shows the pressure variations along the spacer grid which are quite different from previous case: the decrease is not monotonically over the length; there is a dramatical reduce of pressure when leaving the spacer grid. Nevertheless, the overall decrease rates between two test cases are pretty similar.

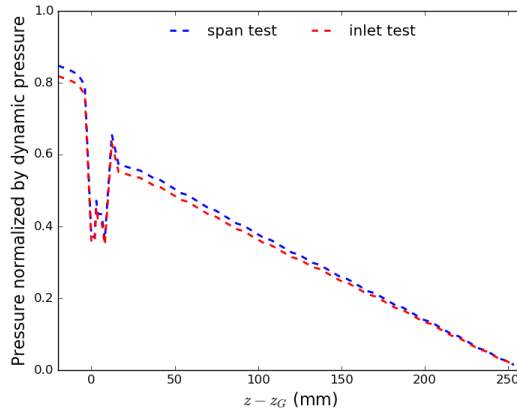


Figure 5-22: Pressure variation along a grid span for $R_{ij} - \varepsilon$ SSG model

Following the same way as previous case, we can calculate one-span pressure loss coefficients (K_{BR}, K_{SSG}) for each case. From Table 5-9, one can notice that both grid-related pressure drop coefficients are underestimated, while inlet test gives better prediction with current turbulence model.

Table 5-9: Comparison of pressure loss coefficients for $R_{ij} - \varepsilon$ SSG model

	Exp.	Span test	Err.	Inlet test	Err.
K_{BR}	0.517	0.517	-	0.517	-
K_{SSG}	0.434	0.414	4.7 %	0.417	3.76 %

5.3.7 Conclusions

Two types of computational domains, one with disturbed tube bundles (with SSG), the other with undisturbed tube bundles (without SSG), are numerically simulated in periodic computations. Momentum source terms are added to ensure a constant mean axial mass flow rate through the simulation. Each type can generate a fully developed turbulent flow at the steady-state regime which will be defined as inlet condition at the classical simulation of test section with a Reynolds number around 100,000. Mean axial velocity distribution on lateral section and pressure drops along z axis are compared with measured data of benchmark experiment.

For axial velocity results: span test shows better agreement with experimental data than inlet test, while difference is not significant. The $k - \varepsilon$ turbulence model can give better results in the region far downstream the SSG, nevertheless, the $R_{ij} - \varepsilon$ SSG model can capture hollows in the region close to SSG. For pressure drop results: the pressure loss is over-predicted with $k - \varepsilon$ model, while it is under-estimated with another turbulence model. The grid-related pressure drop coefficient obtained by span test is more consistent with experimental data. To conclude, present work shows that the influence of SSG is not negligible even far downstream the spacer grid, while discrepancies between two cases is not very significant and can be ignored at certain situations.

5.4 SC/CFD coupling

Finally, the coupling between CFD and SC codes is implemented to simulate the benchmark experiment, with results of pressure drop and axial velocity distributions compared with experimental data to validate coupling methods.

Figure 5-23 shows the flow configurations of the coupled cases without overlap and with partial overlap, respectively. The velocity profile imposed at inlet of each configuration is uniform. The first 10 spans are simulated by SC code while the last span is computed by CFD code with exchange of thermal-hydraulic variables at the coupling interface. The chosen model for turbulence is the " $R_{ij} - \varepsilon$ SSG" one and the cells number of the mesh used by the CFD solver is around 2,3 millions. No field reconstruction is needed at the outlet of the SC domain in these configurations, i.e. flat profiles are imposed at the inlet of the CFD domain. In the following, results of the last span computed by SC solver are compared with that of CFD code as the flow is relatively developed there.

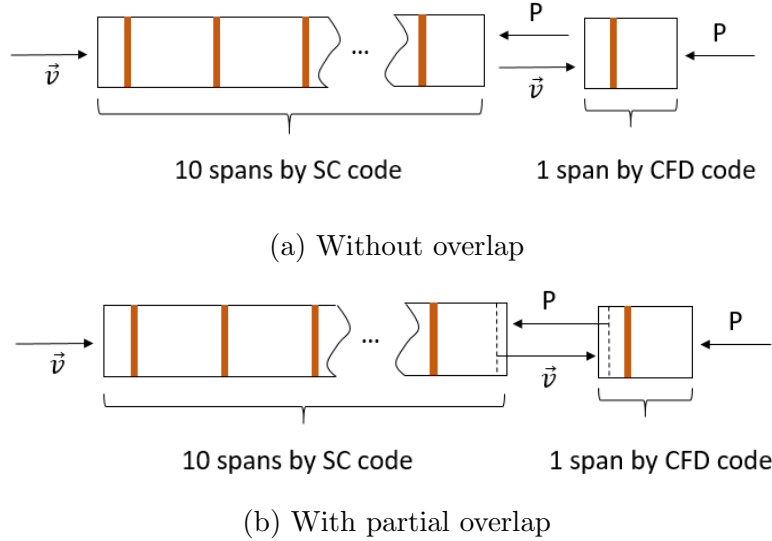


Figure 5-23: SC/CFD coupling configurations

5.4.1 Axial velocity results

In order to ensure the stability according to the Courant number, an adaptive time step width ranges from 1ms to 0.1 μ s is used all along the simulation. The average time step is approximately 50 μ s. A mesh sensitivity was performed using two mesh sizes, one coarse (about 9 million cells) and one fine (about 14 million cells). The simulation carried out with the finer mesh gives similar results to that with coarser mesh, as presented in Figure 5-24.

Concerning the distribution of axial velocity along the x and y axis, both computational configurations give similar results. Only results along the x axis are presented, as depicted in Figure 5-25, where "Overlap (Non-overlap) CFD/SC" corresponds to the CFD/SC part of coupling results with (without) overlap, respectively. Expected hollows are observed at regions close to the spacer grid, with smaller amplitudes however compared to experimental data.

The profiles at the distance of 100 mm and 160 mm from the SSG show good agreement with experimental results, while for the region far away from the spacer grid (ex: $z - z_G = 235mm$), the velocity evolution has a slightly higher amplitude with respect to the reference. Radial refinement with well-developed inlet flow can give better predictions. After the mesh sensitivity study, the amplitude discrepancies between coupling results and experimental data are mainly due to the inlet flow transferred from SC code which is not well-developed.

Results obtained by CFD code show that the velocity distribution is pretty heterogeneous in each sub-channel: it has higher values in the central region while values in the periphery region are lower. Especially for elevations far away from spacer grid, velocities are more concentrated in

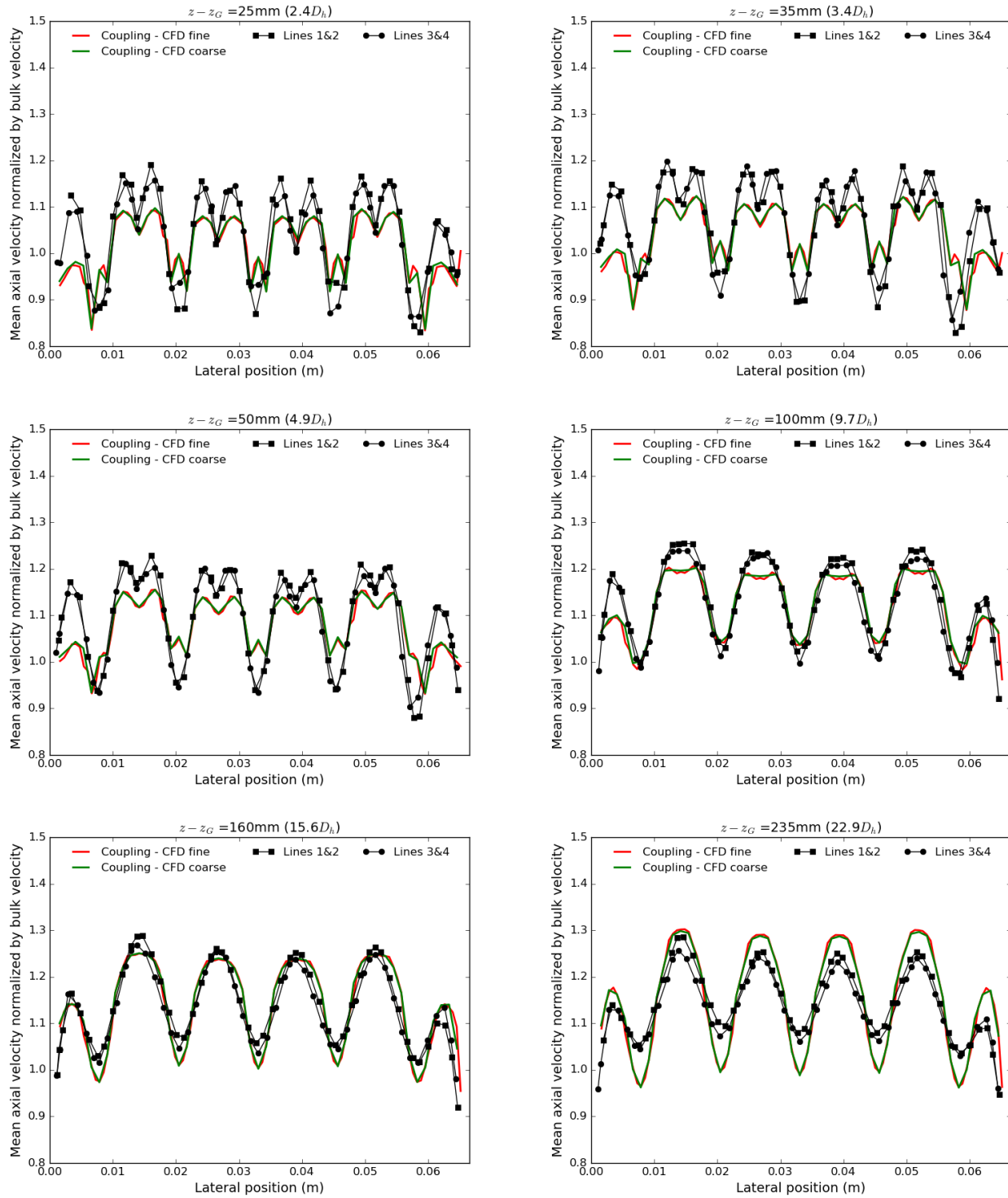


Figure 5-24: Mesh sensitivity study for CFD part: experimental data are indicated as "Lines 1&2" and "Lines 3&4"

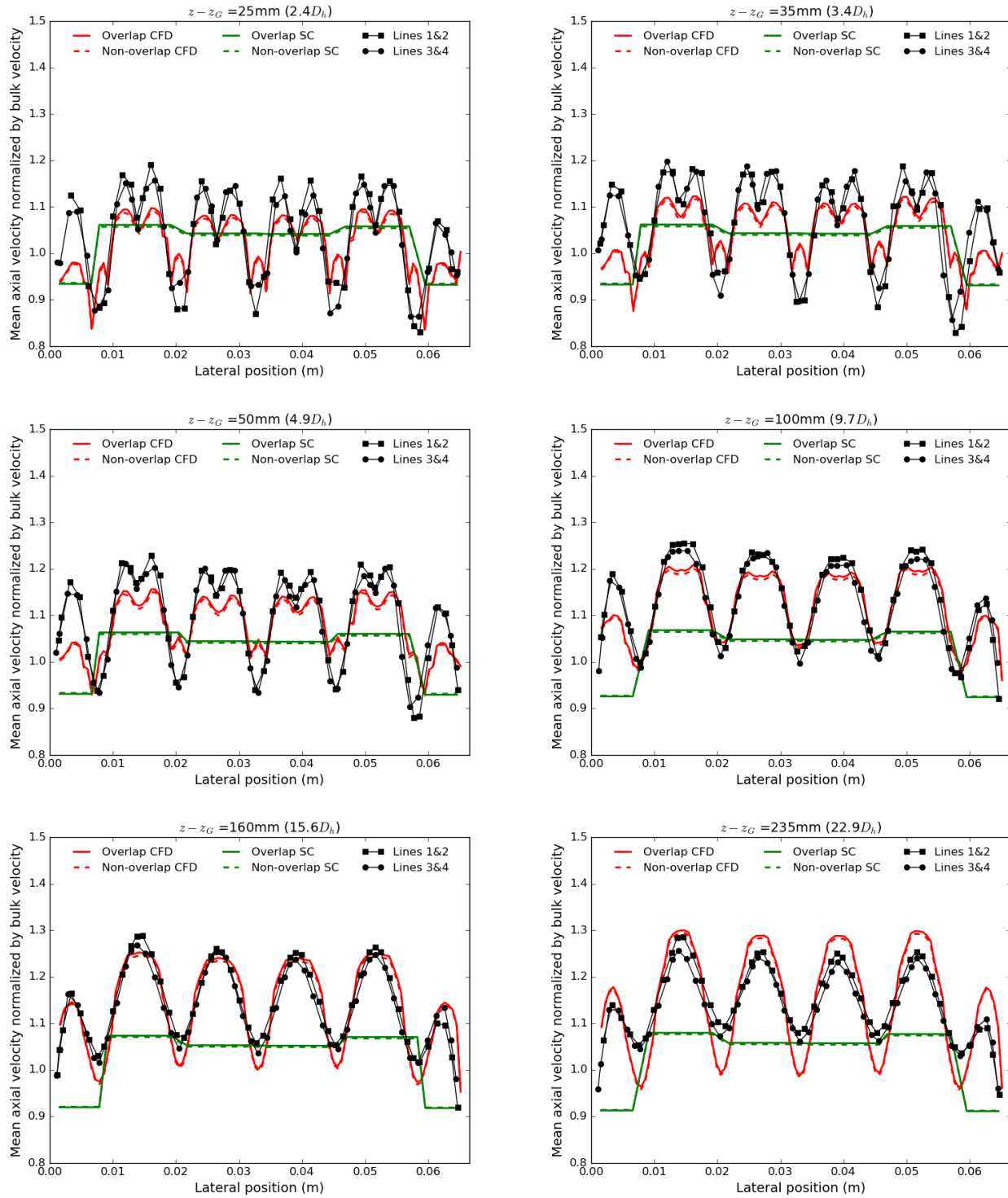


Figure 5-25: Axial velocity distribution for coupling results: experimental data are indicated as "Lines 1&2" and "Lines 3&4"

central regions. Since results of SC solver represent the sub-channel average values, it is normal that the mean value is different with that of CFD part along lines 1&2. Mass flow conservation has been verified quantitatively through output data of two solvers.

Figure 5-25 shows that the couplings with and without overlap give almost the same velocity distribution since the flow can be considered perpendicular to the interface. One can thus refer to the conclusion of one-dimensional flow in this particular situation.

To present the advantages of new coupling method, comparison of computation times between full CFD [103] and SC/CFD coupling is given in Table 5-10. The current couplings save significant time and there is not important difference between overlap and non-overlap cases since the time spent by CFD code is dominant and meshes between two cases are similar.

Table 5-10: Comparison of computation times (hour/proc)

Full CFD	Coupling with overlap	Coupling without overlap
30.5	11.66	11.48

The full CFD computations require a specific work to produce accurate inlet conditions (pre-calculation with a periodic box applicable only to flows perpendicular to the periodic boundary conditions [103], increasing the total cost of the simulation and the complexity of the complete engineering process. The current work is even more significant when considering multiple assemblies with cross flows, where right boundary conditions for a reduced size CFD domain cannot be obtained without SC/CFD coupling.

5.4.2 Pressure drop results

Compared to the experimental pressure loss of 200 mbar/span, the computed value with SC/CFD coupling is 181 mbar/span which gives a better prediction than any other participant of EPRI project [101]. In comparison, the standalone SC code underestimates the pressure loss per span, with a value of 161 mbar. Figure 5-26 presents the pressure axial variation over a span, the reference one is designed according to the pressure loss and its grid-related coefficient obtained in the experiment, the pressure decreases linearly with the same slope upstream and downstream of the spacer grid. There are substantial variations at the two borders of SSG for the CFD part while the pressure decreases monotonously for the SC part of the SC/CFD coupling results.

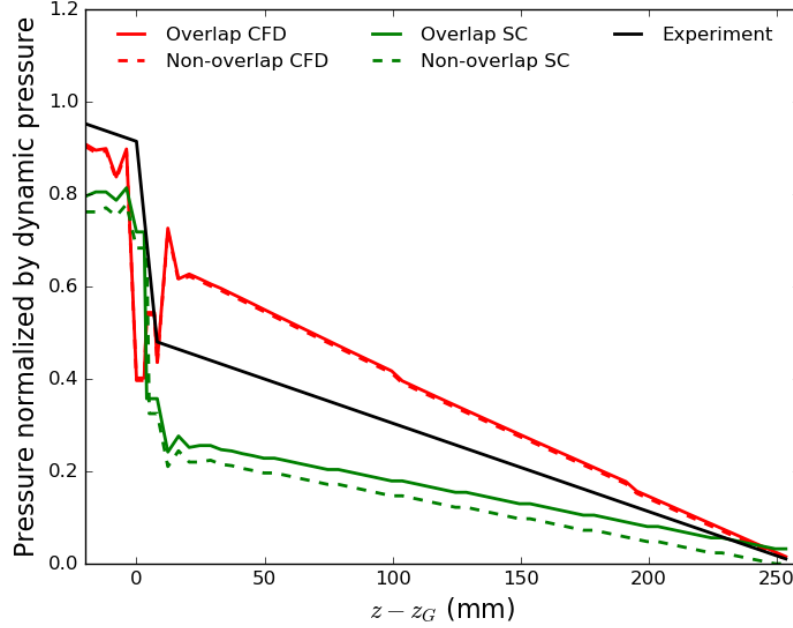


Figure 5-26: Pressure variation along a span

The large under-prediction of the grid span pressure loss may be attributed to several factors, such as turbulence models, near-wall treatment and measurement errors. To quantitatively evaluate the effect of each pressure loss component, a related analysis has been done in previous work [103] and we briefly recall the definition of the one-span grid-related pressure loss coefficient:

$$K_{SSG} \equiv \frac{\Delta P_{SSG}}{P_{dyn}} \quad (5.12)$$

where ΔP_{SSG} indicates the pressure loss due to the addition of the simple support grid, and P_{dyn} is the dynamic pressure $P_{dyn} = \frac{1}{2}\rho V_0^2$.

From Table 5-11, it can be noticed that all computational configurations underestimate the pressure loss related to the spacer grid, while the SC part of SC/CFD coupling results shows better agreement with experimental data.

Table 5-11: Comparison between different cases

	Exp.	SC	Overlap CFD	Non-overlap CFD
$\Delta P_{sp}(mbar)$	200	161	181	181
K_{SSG}	0.434	0.36	0.343	0.343

5.5 Prospective CFD/SC coupling with modified inlet flow

Another coupled configuration of interest can be considered, with the CFD computational domain of one span at the inlet of the global domain and other 10 spans computed by SC code on the downstream side, as presented in Figure 5-27. Used parameters and meshes are the same as the previous case.

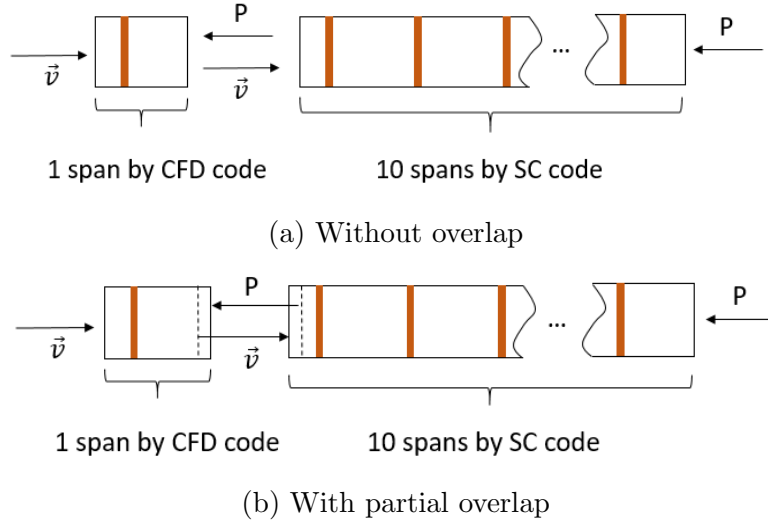


Figure 5-27: CFD/SC coupling configurations

In the purpose to study the evolution of the transverse flow within an assembly, the inlet conditions are modified compared to the experimental reference: half of the inlet surface is overcharged and the remain half inlet surface is undercharged, with the conditions below:

$$U_z(x, y) = \begin{cases} 7 \text{ m/s}, & x \leq L/2, \\ 6 \text{ m/s}, & x > L/2. \end{cases} \quad (5.13)$$

where L is the side length of the rod bundle. The averaged axial velocities for the overcharged and undercharged parts at different elevations are calculated and the variation of their ratio along with the elevation is presented in Figure 5-28.

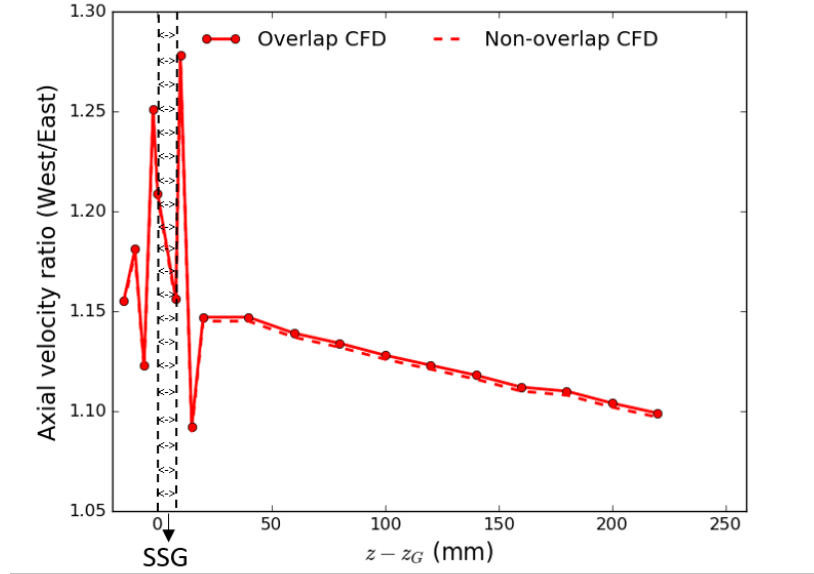


Figure 5-28: Inlet flow mixing - computed axial velocity ratio versus axial elevation

According to the variation of the mean axial velocity ratio, we can observe that the flow is strongly unbalanced upstream and downstream of the spacer grid, and tends to get re-balanced after a certain distance downstream of the grid, converging linearly towards an equilibrium state with respect to the distance. Related to the work of Toumi et al. [119], which compare the SC computational results with experiment for non-uniform inlet flow distribution performed in the HERMES facility, the same unbalanced phenomena after the foot plate and spacer/mixing grid are observed experimentally, while the SC code compute only the re-balanced ones over the whole domain. In the case of non-homogeneous inlet flow conditions, the CFD/SC coupling simulations thus show advantages in the accurate prediction of the evolution of the transverse flow.

5.6 Conclusions

The current work focus on the multi-scale simulation of flow across a fuel rod bundle with a coupling method between CFD and SC codes. The domain decomposition approach is chosen as the spatial coupling method. Data exchange is achieved by transferring mass flow in one direction and pressure in the other. An implicit numerical algorithm is implemented in the current coupling work to enhance both the stability and the convergence.

The coupling of SC/CFD is finally used to simulate a benchmark experiment for validation analysis and results are compared to experimental data. The coupled works with and without overlap give almost the same velocity distribution since the flow can be considered to be perpendicular to the interface. In the CFD domain, mean axial velocity profiles are in good agreement with

experimental results and are close to reference CFD simulations. The proposed coupling satisfactorily predicts the pressure drop coefficient through the support grid located in this domain. Some prospective results of the CFD/SC coupling simulation using non-homogeneous inlet flow conditions show that it is well designed to predict with accuracy the physical re-balancing process within one span of the fuel assembly contrary to the SC code.

The results obtained with the developed coupling method show that it allows to predict correctly the physics compared to reference simulations and that it makes the local simulation of complex flows in a large volume possible with a reasonable and affordable numerical cost.

Chapter 6

Conclusions and perspectives

The present doctoral research project has focused on the investigation, development, preliminary validation and application of a new computational methodology to perform multi-scale flow simulation in fuel assemblies. More in detail, the research has focused on the implementation of a partitioned coupling methodology which makes use of sub-channel and CFD codes in order to improve the simulation of the multi-dimensional thermal-hydraulic phenomena taking place inside the core of a PWR. Moreover, the new coupled codes were tested, verified and validated using appropriate both academic problems and experimental data.

Among the two main strategies that can be adopted for partitioned coupling implementations, namely the domain decomposition and domain overlapping techniques, the research work focus on the former, which envisages the division of the original computational domain into two or more sub-domains, coupled via the dynamic exchange of boundary conditions at coupling interfaces. To implement this technique, the supervisor code ICoCo, written in Python language, has been developed to drive the exchange of data and compute numerical algorithms.

6.1 Conclusions

Hereafter, the main achievements will be summarized. It contains the theoretical part, the results of test cases, the CFD reference calculation of benchmark experiment and coupling work between SC and CFD codes to simulate the MANIVEL experiment.

6.1.1 Coupling methods development

An important part of the research project has been centered on the investigation of linear interpolation method, data exchange with domain decomposition (with or without overlap) and numerical schemes. The main conclusions of this theoretical part can be summarized as follows:

- Concerning domain decomposition approaches, the Dirichlet-Neumann iteration is applied for the case without overlap between subdomains; while the alternating Schwarz method is used for the case with overlapping subdomains since it has higher convergence rate and computational time of CFD solver is dominant in coupling work;
- For numerical schemes, explicit and implicit algorithms based on fixed-point iteration are developed. Explicit schemes, which imply that field variables are exchanged only once in a coupling time step, are often prone to numerical instabilities. Implicit schemes with sub-iterations within each time step can improve numerical stability and allows us to use larger time step which can save significantly computational time.
- Considering different mesh refinements, multigrid data exchange methods are developed which consist of restriction and prolongation procedures. In the coupling work, mass flow rate is passed in one direction while pressure in the opposite one. When passing data from CFD to SC solvers, surface or volume average is required; meanwhile in prolongation procedure, linear interpolation method which ensure the mass conservation at interface is developed to construct continuous velocity profile based on results obtained by SC code.

6.1.2 Verification with test cases

A first verification study of the coupling methodology against test cases was based on the single-phase open pipe flow, coupling results are compared to reference CFD simulations. The CFD code is coupled with CFD and SC codes successively through supervisor code ICoCo to test the reliability of coupling methods.

- The coupling of CFD/CFD is performed firstly: the pressure variation along the pipe shows good agreement with the reference. The non-overlapping approach is enough to simulate the flow perpendicular to the coupling interface and linear interpolation method can impose more appropriate velocity profile in the fine domain. When the flow is non-orthogonal to the interface, the overlapping approach gives better results because the flow direction is conserved. In the case of reverse flow, it is better to consider Dirichlet boundary condition type for the coupling interface with the overlapping approach.
- In the case of SC and CFD codes coupling approach, coupling results are compared with reference CFD and SC ones both in TF (CFD code in the upstream) and FT (SC code in the upstream) modes. The mode with CFD code in upstream seems to be more flexible for transient scenarios since there is no information loss for both codes. The dynamic is well reproduced in both cases according to pressure profiles obtained.

6.1.3 Influence of inlet turbulent flow

The validation study of the coupling methodology was realized against the MANIVEL benchmark experiment. To construct firstly the CFD reference calculation, the influence of inlet turbulent flow which are generated by periodic computations was investigated by comparing results between inlet test and span test.

- For axial velocity distribution, span test shows better agreement with experimental data than inlet test, while discrepancy is not significant. The $k - \varepsilon$ turbulence model gives better results in the region far downstream of the SSG, nevertheless, the $R_{ij} - \varepsilon$ SSG model can capture hollow in the region close to SSG.
- In terms to pressure drop results, the pressure loss is over-predicted with $k - \varepsilon$ model, while it is under-estimated with another turbulence model. The grid-related pressure drop coefficient obtained by span test is more consistent with experimental data.

6.1.4 Experimental validation

Finally, the coupling between SC and CFD codes is implemented to simulate the benchmark experiment, with results of pressure drop and axial velocity distributions compared with experimental data.

- The coupled works with and without overlapping domains give almost the same velocity distribution since the flow can be treated as perpendicular to the interface. In the CFD domain, mean axial velocity profiles are in good agreement with experimental data and the proposed coupling satisfactorily predicts the grid-related pressure drop coefficient.
- The CFD/SC coupling simulation with non-uniform inlet flow conditions can qualitatively predict the physical re-balancing process within one span of the fuel assembly which could be the prospective work to simulate the transverse flow.

6.2 Perspectives

In the future, it could be interesting to construct full "coupling boundary conditions" for non-overlapping and overlapping approaches involving Dirichlet-Neumann and Dirichlet-Dirichlet conditions applied on all variables for each solver. This is expected to improve the results in the reverse flow configuration. Then, large scale computations of significant transverse flow between two or more assemblies will be implemented. It is worth considering the extension of current coupling methodology to simulate two-phase flow.

List of Figures

1-1	Schematic view of a fuel assembly [16]	2
2-1	Illustration of domain overlapping methods	5
2-2	Decomposition into two domains : without (left) and with (right) overlap.	7
2-3	A complex domain made from two overlapping subdomains	7
2-4	Convergence of MS method	10
2-5	Comparison of convergence rates between alternate (left) and parallel (right) Schwarz algorithms	10
2-6	Schematic configuration of new restriction matrices	12
2-7	Comparison between AS (left) and RAS (right) algorithms	13
2-8	Domain divided into two non-overlapping subdomains	15
2-9	Prolongation for fictive cell-centred variables of fine domain	30
2-10	Definition of fictive fine cell value at the junction of two dual cells	32
2-11	Prolongation for fictive surface-centred variables of fine domain	32
2-12	Interpolation for general case	33
2-13	Calculation of junction value for general case	33
2-14	Interpolation with space partially overlapping for collocated grid	35
2-15	Outline of literature review	36
2-16	Data exchange at coupling interfaces for a single-phase open pipe flow	37
2-17	Conceptual scheme of a partitioned coupling method	38
2-18	Sequential communication pattern implemented in the explicit coupling scheme	39
2-19	Flowchart of the generic sequential explicit coupling numerical algorithm	39
2-20	Flowchart of the implicit coupling numerical algorithm	40
2-21	General sequential communication pattern implemented in the implicit coupling scheme	41
2-22	Flowchart of general implicit coupling numerical algorithm	41
4-1	Schematic diagram of computational domains	56
4-2	Different validation cases	57
4-3	Pressure variation along the pipe	57
4-4	Radial velocity distributions at different cases	58

4-5	Schematic diagram of one-dimensional flow configuration	59
4-6	Velocity profiles without domain overlapping for different cases (left) and corresponding relative errors (right)	60
4-7	Schematic diagram of one-dimensional flow configuration with domain partially overlapping	61
4-8	Velocity profiles with domain partially overlapping for different cases (left) and corresponding relative errors (right)	62
4-9	Pressure distribution at the coupling region for the case R1	63
4-10	Schematic diagram of two-dimensional flow configuration	64
4-11	Velocity vector distribution: (left) classic coupling, (right) the reference.	64
4-12	Schematic diagram of two-dimensional flow configuration with SPO method	65
4-13	Velocity vector distribution: (left) FF coupling, (right) the reference.	65
4-14	Velocity profile at the coupling interface: (left) U, (right) V.	66
4-15	Velocity vector distribution: (left) FC coupling, (right) CF coupling.	66
4-16	U profile at the interface: (left) FC coupling, (right) CF coupling.	67
4-17	V profile at the interface: (left) FC coupling, (right) CF coupling.	67
4-18	Diagram of reverse flow configuration: (left) the reference, (right) classic coupling.	68
4-19	Velocity vector distribution: (left) the reference and (right) classic coupling.	68
4-20	Reverse flow configuration with partial overlap: (left) pressure-velocity coupling , (right) velocity-velocity coupling.	69
4-21	Velocity vector distribution: (left) pressure-velocity coupling (right) velocity-velocity coupling.	70
4-22	Velocity profiles at the interface I2 for pressure-velocity coupling: (left) U and (right) V.	70
4-23	Velocity profiles at the interface I2 for velocity-velocity coupling: (left) U and (right) V.	71
4-24	Schematic diagram of FT configuration	72
4-25	Pressure variation along the computational domain in FT configuration	72
4-26	Transient results in FT mode with same time step	73
4-27	Transient results in FT mode with different time steps	74
4-28	Schematic diagram of TF configuration	74
4-29	Pressure variation along the computational domain in TF configuration	75
4-30	Transient results in TF mode compared to standalone reference values	75
5-1	Schematics of the simple support grid	80
5-2	Schematics of the MANIVEL bundles	81
5-3	Rods configuration	82
5-4	DPMi measurement-to-mean value ratios [101]	83
5-5	LDV target measurement mesh, with a zoom over a typical sub-channel [101]	85

5-6	Averaging measured values in (a) lateral positions and (b) axial positions	87
5-7	Averaged experimental mean axial velocity data along probe lines at different elevations	88
5-8	General flowchart of FLICA4 calculation	88
5-9	Mesh configuration used in FLICA4: cross section(left) and axial view (right)	89
5-10	Axial mean velocities distribution	91
5-11	Transverse section of mesh used in simulation	93
5-12	Generation of inlet turbulent flow using inlet box	96
5-13	Generation of inlet turbulent flow using span box	96
5-14	Comparison of the mean axial velocity normalized by bulk velocity for results of present work (left column) and that obtained by participants of EPRI project (right column): experimental data are indicated as "line 1&2" and "line 3&4" [101]	99
5-15	RANS model sensitivity study for span test: experimental data are indicated as "Lines 1&2" and "Lines 3&4"	100
5-16	Turbulent kinetic energy variation along a grid span	101
5-17	Comparison of pressure loss per span	102
5-18	Pressure variation along a grid span	102
5-19	Transverse section of refined mesh used in simulation	103
5-20	Comparison of the mean axial velocity normalized by bulk velocity for $R_{ij} - \varepsilon$ SSG model (left column) and that obtained by participants of EPRI project (right column)	105
5-21	Comparison of pressure loss per span with $R_{ij} - \varepsilon$ SSG model	106
5-22	Pressure variation along a grid span for $R_{ij} - \varepsilon$ SSG model	106
5-23	SC/CFD coupling configurations	108
5-24	Mesh sensitivity study for CFD part: experimental data are indicated as "Lines 1&2" and "Lines 3&4"	109
5-25	Axial velocity distribution for coupling results: experimental data are indicated as "Lines 1&2" and "Lines 3&4"	110
5-26	Pressure variation along a span	112
5-27	CFD/SC coupling configurations	113
5-28	Inlet flow mixing - computed axial velocity ratio versus axial elevation	114

List of Tables

4-1	Boundary conditions	55
4-2	Relative errors for cases with and without overlap	61
4-3	Mass flow balance for different test cases	63
5-1	Pressure drop test run conditions (mean value and variation amplitude) [101]	83
5-2	MANIVEL LDV test run conditions [101]	84
5-3	Axial elevation of LDV-scanned cross-sections in Spans 2a and 2b [101]	84
5-4	One-span pressure loss coefficients based on the MANIVEL pressure drop tests	86
5-5	Reference pressure loss coefficients for isothermal experiment	86
5-6	Boundary conditions in FLICA4	90
5-7	Comparison of calculation/experiment	90
5-8	Comparison of pressure loss coefficients	103
5-9	Comparison of pressure loss coefficients for $R_{ij} - \varepsilon$ <i>SSG</i> model	106
5-10	Comparison of computation times (hour/proc)	111
5-11	Comparison between different cases	112

Bibliography

- [1] D Olander. Nuclear fuels—present and future. Journal of Nuclear Materials, 389(1):1–22, 2009.
- [2] Y Wu, Z Chen, L Hu, M Jin, Y Li, J Jiang, J Yu, C Alejaldre, E Stevens, K Kim, et al. Identification of safety gaps for fusion demonstration reactors. Nature Energy, 1(12):1–11, 2016.
- [3] D.Barbier. L’hydraulique des réacteurs à eau pressurisée. Technical report, Société française d’énergie nucléaire, 1999.
- [4] Long Sun Tong and Yu S Tang. Boiling heat transfer and two-phase flow. Routledge, 2018.
- [5] D Barbier, M Moreau, and J Noailly. Hermes t: French experimental facility for measurement of transverse flows and assessment of the corresponding risk of vibrations in heterogeneous cores. Technical report, American Society of Mechanical Engineers, New York, NY (United States), 1996.
- [6] J Mahaffy, B Chung, C Song, F Dubois, E Graffard, F Ducros, M Heitsch, M Scheuerer, M Henriksson, E Komen, et al. Best practice guidelines for the use of cfd in nuclear reactor safety applications. Technical report, Organisation for Economic Co-Operation and Development, 2007.
- [7] Santiago Corzo, Damian Ramajo, and Norberto Nigro. 1/3d modeling of the core coolant circuit of a phwr nuclear power plant. Annals of Nuclear Energy, 83:386–397, 2015.
- [8] Nuclear Regulatory Commission et al. Relap5/mod3 code manual: Code structure, system models, and solution methods. volume 1. Technical report, Nuclear Regulatory Commission, 1995.
- [9] DR Liles and JH Mahaffy. Trac-pf1/mod1: An advanced best-estimate computer program for pressurized water reactor thermal-hydraulic analysis. Technical report, Los Alamos National Lab., NM (USA). Safety Code Development Group, 1986.
- [10] Dominique Bestion. The physical closure laws in the cathare code. Nuclear Engineering and design, 124(3):229–245, 1990.

- [11] DS Rowe. Cross-flow mixing between parallel flow channels during boiling. part i. cobra: Computer program for coolant boiling in rod arrays. Technical report, Battelle-Northwest, Richland, Wash. Pacific Northwest Lab., 1967.
- [12] CW Stewart, JM Cuta, AS Koontz, JM Kelly, KL Basehore, TL George, and DS Rowe. Vipre-01. a thermal-hydraulic analysis code for reactor cores. volume 1. mathematical modeling.[pwr; bwr]. Technical report, Battelle Pacific Northwest Labs., Richland, WA (USA), 1983.
- [13] Sylvie Aniel, André Bergeron, Philippe Fillion, Danielle Gallo, Fabrice Gaudier, Olivier Grégoire, Matthieu Martin, Edwige Richebois, Eric Royer, Patricia Salvatore, et al. Flica4: Status of numerical and physical models and overview of applications. In Proc. 11th Int. Top. Meeting on Nuclear Thermo-Hydraulics (NURETH-11), pages 2–6, 2005.
- [14] A Moorthi, Anil Kumar Sharma, and K Velusamy. A review of sub-channel thermal hydraulic codes for nuclear reactor core and future directions. Nuclear Engineering and Design, 332:329–344, 2018.
- [15] B Liu, S He, C Moulinec, and J Uribe. Sub-channel cfd for nuclear fuel bundles. Nuclear Engineering and Design, 355:110318, 2019.
- [16] EDF. Pressurized water reactor, 2021. <https://watt-logic.com/2021/07/31/epr-update/>.
- [17] W. Wiesenack. 9 - nuclear fuel assembly design and fabrication. In Ian Crossland, editor, Nuclear Fuel Cycle Science and Engineering, Woodhead Publishing Series in Energy, pages 203–233. Woodhead Publishing, 2012.
- [18] Ulrich Bieder. Analysis of the flow down-and upwind of split type mixing vanes. Proc. of the CFD4NRS-4, Daejeon, Korea, Sept, 10:12, 2012.
- [19] Fujiang Yu, Andreas G. Class, Jianjun Xiao, and Thomas Jordan. Coarse grid cfd methodology: flux corrections for individual mesh cells and application to rod bundles. In 17th International Topical Meeting on Nuclear Reactor Thermal Hydraulics, NURETH 2017; Qujiang Int’l Conference Center Xi’an, Shanxi; China; 3 September 2017 through 8 September 2017, page Paper No. 21717. Association for Computing Machinery (ACM), 2017. 32.02.11; LK 01.
- [20] CL Farmer. Upscaling: a review. International journal for numerical methods in fluids, 40(1-2):63–78, 2002.
- [21] Xilin Zhang, Kanglong Zhang, VH Sanchez-Espinoza, and Hongli Chen. Multi-scale coupling of cfd code and sub-channel code based on a generic coupling architecture. Annals of Nuclear Energy, 141:107353, 2020.

- [22] Timothy P Grunloh and A Manera. A novel multi-scale domain overlapping cfd/sth coupling methodology for multi-dimensional flows relevant to nuclear applications. Nuclear Engineering and Design, 318:85–108, 2017.
- [23] TH Fanning and JW Thomas. Advances in coupled safety modeling using systems analysis and high-fidelity methods. Technical report, Argonne National Lab.(ANL), Argonne, IL (United States), 2010.
- [24] Marti Jeltsov, Kaspar Kööp, Pavel Kudinov, and Walter Villanueva. Development of a domain overlapping coupling methodology for sth/cfd analysis of heavy liquid metal thermal-hydraulics. In NURETH-15, 2013.
- [25] Yinxing Zhang, Puzhen Gao, Chunping Tian, Xiaoqiang He, Chong Chen, and Zhongyi Wang. Coupling one-dimensional user code and star-ccm+ for simulation of rolling conditions in a rod bundle channel. Annals of Nuclear Energy, 151:107888, 2021.
- [26] Victorita Dolean, Pierre Jolivet, and Frédéric Nataf. An Introduction to Domain Decomposition Methods: algorithms, theory and parallel implementation. Lecture, January 2015.
- [27] Andrea Toselli and Olof Widlund. Domain decomposition methods-algorithms and theory, volume 34. Springer Science & Business Media, 2004.
- [28] Tony F Chan and Tarek P Mathew. Domain decomposition algorithms. Acta numerica, 3:61–143, 1994.
- [29] Martin J Gander, Felix Kwok, and Bankim C Mandal. Dirichlet-neumann and neumann-neumann waveform relaxation algorithms for parabolic problems. arXiv preprint arXiv:1311.2709, 2013.
- [30] Antonio Toti, Jan Vierendeels, and F Belloni. Improved numerical algorithm and experimental validation of a system thermal-hydraulic/cfd coupling method for multi-scale transient simulations of pool-type reactors. Annals of Nuclear Energy, 103:36–48, 2017.
- [31] Małgorzata Peszynska, Qin Lu, and Mary F Wheeler. Coupling different numerical algorithms for two phase fluid flow. 1999.
- [32] Kanglong Zhang, Alejandro Campos Munoz, and Victor Hugo Sanchez-Espinoza. Development and verification of the coupled thermal-hydraulic code-trace/scf based on the icoco interface and the salome platform. Annals of Nuclear Energy, 155:108169, 2021.
- [33] Timothy P Grunloh and Annalisa Manera. A novel domain overlapping strategy for the multiscale coupling of cfd with 1d system codes with applications to transient flows. Annals of Nuclear Energy, 90:422–432, 2016.

- [34] R Bavière, N Tauveron, F Perdu, E Garré, and S Li. A first system/cfd coupled simulation of a complete nuclear reactor transient using cathare2 and trio_u. preliminary validation on the phénix reactor natural circulation test. Nuclear Engineering and Design, 277:124–137, 2014.
- [35] A Huxford et al. Development of innovative overlapping-domain coupling between sam and nekrs. Proc. Proceedings of NURETH, 2022.
- [36] B Liu, S He, C Moulinec, and J Uribe. A coupling approach between resolved and coarse-grid sub-channel cfd. Nuclear Engineering and Design, 377:111124, 2021.
- [37] TP Grunloh and A Manera. Comparison of overlapping and separate domain coupling methods. In NURETH-16: 16th International Topical Meeting on Nuclear Reactor Thermal Hydraulics, ISBN: 978-0-89448-722, volume 4, 2015.
- [38] G. Meurant. Studies in mathematics and its applications. In G. Meurant, editor, Computer Solution of Large Linear Systems, volume 28 of Studies in Mathematics and Its Applications. Elsevier, 1999.
- [39] A. Quarteroni and A. Valli. Domain decomposition methods for partial differential equations. Number BOOK. Oxford University Press, 1999.
- [40] Barry Smith, Peter Bjørstad, and William Gropp. Domain Decomposition: Parallel Multilevel Methods for Elliptic Partial Differential Equations. Number BOOK. Cambridge University Press, 2004.
- [41] Frédéric Magoules. Mesh partitioning techniques and domain decomposition methods. Saxe-Coburg Publications, 2008.
- [42] H.A. Schwarz. Ueber einige abbildungsaufgaben. 1869(70):105–120, 1869.
- [43] Véronique Martin. Introduction aux méthodes de schwarz.
- [44] Martin J. Gander. Schwarz methods over the course of time. ETNA. Electronic Transactions on Numerical Analysis [electronic only], 31:228–255, 2008.
- [45] Pierre-Louis Lions. On the schwarz alternating method.i. In First international symposium on domain decomposition methods for partial differential equations, volume 1, pages 1–42. SIAM Philadelphia, 1988.
- [46] Pierre-Louis Lions. On the schwarz alternating method. ii: Stochastic interpretation and orders properties. In Second international symposium on domain decomposition methods for partial differential equations, volume 1, pages 47–70. SIAM Philadelphia, 1989.

- [47] Pierre-Louis Lions. On the schwarz alternating method. iii: a variant for nonoverlapping subdomains. In Third international symposium on domain decomposition methods for partial differential equations, volume 6, pages 202–223. SIAM Philadelphia, 1990.
- [48] Marc Garbey, Yu A Kuznetsov, and Yu V Vassilevski. A parallel schwarz method for a convection-diffusion problem. SIAM Journal on Scientific Computing, 22(3):891–916, 2000.
- [49] M. Dryja. A capacitance matrix method for dirichlet problem on polygon region. Numerische Mathematik, 39:51–64, 1982.
- [50] Olof Widlund and M Dryja. An additive variant of the Schwarz alternating method for the case of many subregions. Technical Report 339, Ultracomputer Note 131. Department of Computer Science, Courant Institute, dec 1987.
- [51] Maksymilian Dryja and Olof B Widlund. Towards a unified theory of domain decomposition algorithms for elliptic problems. In Third international symposium on domain decomposition methods for partial differential equations, pages 3–21, 1990.
- [52] Q. V. Dinh, Bertrand Mantel, Jacques Périaux, and Roland Glowinski. Approximate solution of the navier-stokes equations for incompressible viscous fluids, related domain decomposition methods. 1983.
- [53] Olof Widlund and Maksymilian Dryja. On the optimality of an additive iterative refinement method. Technical Report 442, Ultracomputer Note 156. Department of Computer Science, Courant Institute, apr 1989.
- [54] Xiao-Chuan Cai and Marcus Sarkis. A restricted additive schwarz preconditioner for general sparse linear systems. Siam journal on scientific computing, 21(2):792–797, 1999.
- [55] Evridiki Efstathiou and Martin J. Gander. Why restricted additive schwarz converges faster than additive schwarz. BIT, 43(5):945–959, dec 2003.
- [56] Martin J Gander. Optimized schwarz methods. SIAM Journal on Numerical Analysis, 44(2):699–731, 2006.
- [57] Patrick Le Tallec, Yann-Hervé De Roeck, and Marina Vidrascu. Domain decomposition methods for large linearly elliptic three-dimensional problems. Journal of Computational and Applied Mathematics, 34(1):93–117, 1991.
- [58] Charbel Farhat and Francois-Xavier Roux. A method of finite element tearing and interconnecting and its parallel solution algorithm. International journal for numerical methods in engineering, 32(6):1205–1227, 1991.

- [59] Jean-François Bourgat, Roland Glowinski, Patrick Le Tallec, and Marina Vidrascu. Variational formulation and algorithm for trace operation in domain decomposition calculations. PhD thesis, INRIA, 1988.
- [60] Axel Klawonn and Olof Widlund. Feti and neumann-neumann iterative substructuring methods: connections and new results. Communications on Pure and Applied Mathematics: A Journal Issued by the Courant Institute of Mathematical Sciences, 54(1):57–90, 2001.
- [61] Olof B Widlund. Iterative substructuring methods: Algorithms and theory for elliptic problems in the plane. In First International Symposium on Domain Decomposition Methods for Partial Differential Equations, Philadelphia, PA, 1988.
- [62] Ivo Dravins. The dirichlet-neumann iteration–three-field case: Methods and analyses. Master’s Theses in Mathematical Sciences, 2018.
- [63] Jörg Liesen and Zdenek Strakos. Krylov subspace methods: principles and analysis. Oxford University Press, 2013.
- [64] Lewis Fry Richardson. IX. the approximate arithmetical solution by finite differences of physical problems involving differential equations, with an application to the stresses in a masonry dam. Philosophical Transactions of the Royal Society of London. Series A, Containing Papers of a Mathematical or Physical Character, 210(459-470):307–357, 1911.
- [65] Eduard Stiefel. Methods of conjugate gradients for solving linear systems. J. Res. Nat. Bur. Standards, 49:409–435, 1952.
- [66] Michel Belliard and Marc Grandotto. Local zoom computation of two-phase flows in steam generators using a local defect correction method. Numerical Heat Transfer: Part A: Applications, 43(2):111–135, 2003.
- [67] R Minero, MJH Anthonissen, and RMM Mattheij. A local defect correction technique for time-dependent problems. Numerical Methods for Partial Differential Equations: An International Journal, 22(1):128–144, 2006.
- [68] Wolfgang Hackbusch. Local defect correction method and domain decomposition techniques. In Defect correction methods, pages 89–113. Springer, 1984.
- [69] Petter E Bjørstad and Olof B Widlund. Solving elliptic problems on regions partitioned into substructures. In Elliptic Problem Solvers, pages 245–255. Elsevier, 1984.
- [70] Achi Brandt. Guide to multigrid development. In Multigrid methods, pages 220–312. Springer, 1982.
- [71] Göran Starius. Composite mesh difference methods for elliptic boundary value problems. Numerische Mathematik, 28(2):243–258, 1977.

- [72] Roland Glowinski, Jacques Périaux, and Quang Vinh Dinh. Domain decomposition methods for non linear problems in fluid dynamics. PhD thesis, INRIA, 1982.
- [73] Wolfgang Hackbusch. The fast numerical solution of very large elliptic difference schemes. IMA Journal of Applied Mathematics, 26(2):119–132, 1980.
- [74] Michel Belliard. Multigrid preconditioning of steam generator two-phase mixture balance equations in the genepi software. Progress in computational fluid dynamics, 6(8):459–474, 2006.
- [75] Wolfgang Hackbusch. Multi-grid methods and applications, volume 4. Springer Science & Business Media, 2013.
- [76] Achi Brandt, JE Dendy Jr, and Hans Ruppel. The multigrid method for semi-implicit hydrodynamics codes. Journal of Computational Physics, 34(3):348–370, 1980.
- [77] Isabelle Ramiere, Philippe Angot, and Michel Belliard. A fictitious domain approach with spread interface for elliptic problems with general boundary conditions. Computer Methods in Applied Mechanics and Engineering, 196(4-6):766–781, 2007.
- [78] S Pratap Vanka. Block-implicit multigrid solution of navier-stokes equations in primitive variables. Journal of Computational Physics, 65(1):138–158, 1986.
- [79] Christophe Romé. Une méthode de raccordement de maillages non-conformes pour la résolution des équations de Navier-Stokes. PhD thesis, Université Sciences et Technologies-Bordeaux I, 2006.
- [80] Søren Taverniers, Alexander Y Pigarov, and Daniel M Tartakovsky. Conservative tightly-coupled simulations of stochastic multiscale systems. Journal of Computational Physics, 313:400–414, 2016.
- [81] B.Raverdy. Méthode multi-domaines non conforme dans mc3d. Technical report, Institute for radiological protection and nuclear safety, 2015.
- [82] Wei Li, Xiaoli Wu, Dalin Zhang, Guanghui Su, Wenxi Tian, and Suizheng Qiu. Preliminary study of coupling cfd code fluent and system code relap5. Annals of Nuclear Energy, 73:96–107, 2014.
- [83] Vincent Bergeaud and Vincent Lefebvre. Salome. a software integration platform for multi-physics, pre-processing and visualisation. 2010.
- [84] Fabien Perdu and Simone Vandroux. System/cfd coupling for reactor transient analysis. an application to the gas fast reactor with cathare and trio-u. In Proceedings of the 2008 International Congress on Advances in Nuclear Power Plants-ICAPP’08, 2008.

- [85] IK Park, JR Lee, SW Lee, HY Yoon, and JJ Jeong. An implicit code coupling of 1-d system code and 3-d in-house cfd code for multi-scaled simulations of nuclear reactor transients. Annals of Nuclear Energy, 59:80–91, 2013.
- [86] Antonio Toti, J Vierendeels, and F Belloni. Coupled system thermal-hydraulic/cfd analysis of a protected loss of flow transient in the myrrha reactor. Annals of Nuclear Energy, 118:199–211, 2018.
- [87] Joe D Hoffman and Steven Frankel. Fixed-point iteration. In Numerical Methods for Engineers and Scientists, pages 141–145, 2001.
- [88] T.Hibiki M.Ishii. Thermal-fluid dynamics of two phase flow. 2006.
- [89] Thomas Galié. Couplage interfacial de modèles en dynamique des fluides. Application aux écoulements diphasiques. PhD thesis, Université Pierre et Marie Curie-Paris VI, 2009.
- [90] Anouar Mekkas, Anne Charneau, and Sami Kouraichi. A new numerical algorithm for two-phase flows drift-flux model with staggered grid in porous media. ESAIM: Proceedings and Surveys, 58:58–77, 2017.
- [91] CEA-EDF-FRAMATOME-IRSN. NEPTUNE CFD, 2020. <https://www.code-saturne.org/cms/neptune-cfd>.
- [92] Jean-Marc Hérard and Olivier Hurisse. The numerical coupling of a two-fluid model with an homogeneous relaxation model. In Finite volumes for complex applications V, pages 503–510. ISTE-Wiley, 2008.
- [93] Edwige Godlewski, Kim-Claire Le Thanh, and Pierre-Arnaud Raviart. The numerical interface coupling of nonlinear hyperbolic systems of conservation laws: Ii. the case of systems. ESAIM: Mathematical Modelling and Numerical Analysis, 39(4):649–692, 2005.
- [94] Edwige Godlewski. Coupling fluid models. Exploring some features of interfacial coupling, in” Finite Volumes for Complex Applications V”(eds. R. Eymard and J.-M. Hérard), ISTE-Wiley, pages 87–102, 2008.
- [95] Mamoru Ishii. Collection de la direction des etudes et recherches d’électricite de france. editeur Eyrolles, 22:275p, 1975.
- [96] Melvin R Baer and Jace W Nunziato. A two-phase mixture theory for the deflagration-to-detonation transition (ddt) in reactive granular materials. International journal of multiphase flow, 12(6):861–889, 1986.
- [97] Thierry Gallouët, Jean-Marc Hérard, and Nicolas Seguin. Numerical modeling of two-phase flows using the two-fluid two-pressure approach. Mathematical Models and Methods in Applied Sciences, 14(05):663–700, 2004.

- [98] Chufa Qiu, Bruno Raverdy, and Vincent Faucher. Development of a sub-channel/cfd coupling method for multi-scaled simulations. In International Topic Meeting on Nuclear Reactor Thermal Hydraulics. American Nuclear Society, 2022.
- [99] Chufa Qiu, Bruno Raverdy, and Vincent Faucher. Development of a partitioned coupling method for complex hydraulics based on multi-scale data exchanges between porous and cfd solvers with application to fuel assemblies in a nuclear core. Annals of Nuclear Energy (In press), 2022.
- [100] B Liu, S He, C Moulinec, and J Uribe. Coupled porous media approaches in sub-channel cfd. Nuclear Engineering and Design, 377:111159, 2021.
- [101] S Yagnik and D Wells. Computational fluid dynamics benchmark of high fidelity rod bundle experiments: Industry round robin phase 1–rod bundle with simple support grids. Final Report), March, 2014.
- [102] WH McAdams. Heat transfer. McGraw-Hill, New York, 1(51):3, 1954.
- [103] Chufa Qiu, Bruno Raverdy, Vincent Faucher, and André Bergeron. Influence of inlet turbulent flow generated by periodic computations on the pressure drop and axial velocity distribution predictions. In International Conference on Nuclear Engineering, volume 85260, page V003T08A004. American Society of Mechanical Engineers, 2021.
- [104] Y. Hassan. 12 - an overview of computational fluid dynamics and nuclear applications. In Francesco D’Auria, editor, Thermal-Hydraulics of Water Cooled Nuclear Reactors, pages 729 – 829. Woodhead Publishing, 2017.
- [105] Y Katto. Critical heat flux. International Journal of Multiphase Flow, 20:53–90, 1994.
- [106] J. Mahaffy, B. Chung, C. Song, F. Dubois, E. Graffard, F. Ducros, M. Heitsch, M. Scheuerer, M. Henriksson, E. Komen, F. Moretti, T. Morii, P. Muehlbauer, U. Rohde, B. L. Smith, T. Watanabe, and G. Zigh. Best practice guidelines for the use of cfd in nuclear reactor safety applications (nea-csni-r–2007-05). nuclear energy agency of the oecd (nea). 2007.
- [107] JR Secker, MY Young, and JL Bradfute. Evaluation and mitigation of crud induced power shift. 2004.
- [108] Andrew Dykhuis and Michael Short. Three dimensional multiphysics modeling and validation of crud-induced localized corrosion (cilc) in pwr [npc 2014: Nuclear plant chemistry conference 2014]. 2014.
- [109] Rosa Yang, Bo Cheng, Jeff Deshon, Kurt Edsinger, and Odelli Ozer. Fuel r & d to improve fuel reliability. Journal of nuclear science and technology, 43(9):951–959, 2006.

- [110] Shin K Kang and Yassin A Hassan. Computational fluid dynamics (cfd) round robin benchmark for a pressurized water reactor (pwr) rod bundle. Nuclear Engineering and Design, 301:204–231, 2016.
- [111] Michael E Conner, Emilio Baglietto, and Abdelaziz M Elmahdi. Cfd methodology and validation for single-phase flow in pwr fuel assemblies. Nuclear Engineering and Design, 240(9):2088–2095, 2010.
- [112] A Bergeron, T Chataing, J Garnier, E Decossin, P Péturaud, and SK Yagnik. Design, feasibility, and testing of instrumented rod bundles to improve heat transfer knowledge in pwr fuel assemblies. In Proceedings of the 2007 LWR Fuel Performance Meeting/TopFuel 2007'Zero by 2010', 2007.
- [113] CEA-EDF. SALOME, 2021. <http://www.salome-platform.org>.
- [114] M Martin, T Keheley, K Vogel, K Goodheart, A Hatman, and A Chatelain. Validation of areva's best practices in the epri round robin benchmark. In Proceeding of the 16th International Topical Meeting on Nuclear Reactor Thermal Hydraulics, NURETH, volume 16, 2015.
- [115] Luigi Capone, Sofiane Benhamadouche, and Yassin A Hassan. Source terms modeling for spacer grids with mixing vanes for cfd simulations in nuclear reactors. Computers & Fluids, 126:141–152, 2016.
- [116] Sofiane Benhamadouche, Luigi Capone, and Yassin Hassan. Source terms modeling of nuclear reactors spacer grids with mixing vanes for CFD simulations. Computers and Fluids, 126:141–152, 2016.
- [117] Guodong Gai, Abdellah Hadjadj, Sergey Kudriakov, Stéphane Mimouni, and Olivier Thomine. Numerical study of spray-induced turbulence using industrial fire-mitigation nozzles. Energies, 14(4):1135, 2021.
- [118] S Benhamadouche. Pressure drop predictions using code_saturne in nestor cfd benchmark. In Proceedings of the 16th International Topical Meeting on Nuclear Reactor Thermal Hydraulics (NURETH-16), 2015.
- [119] I Toumi, A Bergeron, D Gallo, E Royer, and D Caruge. Flica-4: a three-dimensional two-phase flow computer code with advanced numerical methods for nuclear applications. Nuclear Engineering and Design, 200(1-2):139–155, 2000.